

HABOOBS IN OUTER SPACE: THE WHEN AND WHERE OF DUST STORMS IN
DISTANT GALAXIES

by
Kyle Penner

A Dissertation Submitted to the Faculty of the
DEPARTMENT OF ASTRONOMY
In Partial Fulfillment of the Requirements
For the Degree of
DOCTOR OF PHILOSOPHY
In the Graduate College
THE UNIVERSITY OF ARIZONA

2014

THE UNIVERSITY OF ARIZONA
GRADUATE COLLEGE

As members of the Dissertation Committee, we certify that we have read the dissertation prepared by Kyle Penner entitled “Haboobs in outer space: The when and where of dust storms in distant galaxies” and recommend that it be accepted as fulfilling the dissertation requirement for the Degree of Doctor of Philosophy.

_____ Date: 2014 May 7
Mark Dickinson

_____ Date: 2014 May 7
Buell T. Jannuzi

_____ Date: 2014 May 7
Alexandra Pope

_____ Date: 2014 May 7
Dennis Zaritsky

_____ Date: 2014 May 7
Xiaohui Fan

Final approval and acceptance of this dissertation is contingent upon the candidate’s submission of the final copies of the dissertation to the Graduate College.

I hereby certify that I have read this dissertation prepared under my direction and recommend that it be accepted as fulfilling the dissertation requirement.

_____ Date: 2014 May 7
Dissertation Director: Mark Dickinson

_____ Date: 2014 May 7
Dissertation Director: Buell T. Jannuzi

STATEMENT BY AUTHOR

This dissertation has been submitted in partial fulfillment of requirements for an advanced degree at The University of Arizona and is deposited in the University Library to be made available to borrowers under rules of the Library.

Brief quotations from this dissertation are allowable without special permission, provided that accurate acknowledgment of source is made. Requests for permission for extended quotation from or reproduction of this manuscript in whole or in part may be granted by the head of the major department or the Dean of the Graduate College when in his or her judgment the proposed use of the material is in the interests of scholarship. In all other instances, however, permission must be obtained from the author.

SIGNED: Kyle Penner

ACKNOWLEDGMENTS

I thank my advisors, Alex Pope and Mark Dickinson, for enduring my obstinacy.

DEDICATION

For the teachers I've taken from: Lauri Crestani, Greg Sitz, and Paul Schimelman.

TABLE OF CONTENTS

LIST OF FIGURES	8
LIST OF TABLES	9
ABSTRACT	11
1 INTRODUCTION	13
2 REDSHIFT ORIGINS OF THE COSMIC MILLIMETER BACKGROUND	16
2.1 Motivation	16
2.2 Data	18
2.2.1 Creating the combined 1.16 mm map	18
2.2.2 Verifying the 1.16 mm map	22
2.2.3 Sample	27
2.3 Stacking analysis	28
2.3.1 The effects of angular clustering on stacking analyses	30
2.3.2 Quantifying the effects of angular clustering	32
2.4 Results and discussion	37
2.5 Summary	47
3 QUIDDITY OF DOGs	49
3.1 Motivation	50
3.2 Data	52
3.2.1 Measured quantities	52
3.2.2 Samples	54
3.2.3 Derived quantities	58
3.3 Results	60
3.4 Discussion	65
3.5 Summary	73
4 Is β WELL-DEFINED?	76
4.1 Motivation	76
4.2 Simulated β values	77
4.3 Results and discussion	79
4.3.1 The Calzetti attenuation formula	79
4.3.2 The attenuation formula for $z \sim 2$ dusty galaxies	83
4.3.3 The attenuation formula based on Murphy	86
5 NONUNIFORM DUST DISTRIBUTIONS IN DUSTY GALAXIES	89
5.1 Motivation	90
5.2 Data	92
5.2.1 Measured quantities	92

5.2.2	Derived quantities	95
5.3	Results	97
5.4	Discussion	103
5.5	Summary	106
6	FUTURE DIRECTIONS	108

LIST OF FIGURES

2.1	Detector transmission curves	20
2.2	Distribution of normalized weights	21
2.3	Empirical deboosting comparison for 1.1 mm sources	26
2.4	Empirical deboosting comparison for 1.2 mm sources	27
2.5	Test of angular clustering at 1.1 mm	35
2.6	Test of angular clustering at 850 μm	38
2.7	Stacked flux densities	39
2.8	Contribution to background vs. S_{24}	40
2.9	Redshift distributions of the resolved 850 μm and 1.16 mm background	42
2.10	Predicted redshift origins of total 1.16 mm background	45
2.11	Comparing our results to those of Viero	47
3.1	DOG selection	55
3.2	Redshift distributions	56
3.3	Distributions of IR luminosities	61
3.4	Stellar masses vs. redshift	62
3.5	S_{100}/S_{24} vs. redshift	63
3.6	S_{250}/S_{24} vs. redshift	64
3.7	$S_{2.2}/S_{0.65}$ vs. redshift	65
3.8	Specific star formation rates vs. redshift	69
3.9	IRX vs. β	71
4.1	β and the Calzetti attenuation formula	81
4.2	β and the Calzetti attenuation formula vs. redshift	82
4.3	β and the attenuation formula for $z \sim 2$ dusty galaxies	84
4.4	β and the attenuation formula for $z \sim 2$ dusty galaxies vs. redshift	85
4.5	β and the attenuation formula based on Murphy	87
4.6	β and the attenuation formula based on Murphy vs. redshift	88
5.1	$\text{H}\alpha$ vs. UV escape fraction for low- z dust-poor galaxies	99
5.2	$\text{H}\alpha$ vs. UV escape fraction for low- z dusty galaxies	101
5.3	$\text{H}\alpha$ vs. UV escape fraction for high- z dusty galaxies	102
5.4	$\text{H}\beta$ vs. $\text{H}\alpha$ escape fraction for low- z dusty galaxies	105

LIST OF TABLES

2.1	Secure detections in the 1.16 mm map	23
2.1	Secure detections in the 1.16 mm map	24
2.2	The effects of angular clustering on the resolved background	34
2.3	The total background at 4 wavelengths	41
2.4	Redshift distributions of the resolved 850 μm and 1.16 mm background . .	44
3.1	Basic properties of DOG and control samples	57

“Meronym spoke, marv’lin’ as much as me, they wasn’t temples, nay, but *observ’trees* what Old Uns used to study the planets’n’moon’n’stars, an’ the space b’tween, to und’stand where ev’rythin’ begins an’ where ev’rythin’ ends.”

—David Mitchell, *Cloud Atlas*

ABSTRACT

Dust grains are a minor component by mass of the interstellar medium of a galaxy. Yet they can be the dominant source of luminosity. At $z \sim 1$, the luminosity density of the Universe in the IR is ~ 10 times higher than it is at $z \sim 0$; common high-redshift galaxies have IR luminosities and dust masses that surpass those of even rare low-redshift galaxies. Dusty galaxies must transition to dust-poor galaxies. In this thesis, we attempt to understand the When? and Where? of this transition. We examine the redshift distribution of the cosmic millimeter background and the spatial distributions of dust in high-redshift galaxies.

The cosmic millimeter background is the flux surface density, across the entire sky, from dust emission from all galaxies in the Universe. We stack the 1.16 mm flux densities of a sample of dusty galaxies to determine the evolution of their contribution to the background. We resolve $\sim 35\%$ of the background at 1.16 mm and $\sim 50\%$ of the background at $850\mu\text{m}$. We make two unique predictions for the redshift origins of the total 1.16 mm background.

Dust is responsible for more than the IR emission from a galaxy. The existence of dust is a necessary but not sufficient condition for the attenuation of a galaxy's intrinsic UV emission; the IR- and emergent UV-emitting regions must be spatially coincident. We establish a relation between the ratio of infrared to UV luminosity and β for dusty galaxies at $z \sim 2$, which implies that their regions are coincident. We also argue that the dust is spread on galactic scales.

In dust-poor galaxies at low redshift, the amount of dust attenuating the emission from ionizing stars is greater than the amount attenuating the emission from massive but nonionizing stars. For dusty galaxies at $z \sim 1.3$, the amounts may be unequal—though this result is subject to the assumption that high-redshift dusty galaxies have the same

spatial and grain size distributions as low-redshift dust-poor galaxies. The dust properties of high-redshift galaxies may be more diverse than they are in low-redshift galaxies.

CHAPTER 1

INTRODUCTION

For 13.7 billion years, the energies of photons have been redistributed. Between recombination and the completion of reionization, Hydrogen atoms kept the Universe dark; after reionization, Hydrogen atoms—the Ly α forest—kept galaxies dark (at specific wavelengths). And the expansion of space itself decreases the energies of photons.

Dust grains redistribute the energies of photons in ways less amenable to calculations from first-principles. Grains absorb and scatter ultraviolet and optical photons, heat up, and then radiate this heat at infrared (IR) wavelengths. They do not generate their own energy yet they are the great equalizer of emission from galaxies. While 0.01% of the baryons at $z \sim 0$ are in dust, the emission from dust in galaxies at all redshifts is roughly equal to the emission from stars in galaxies at all redshifts (Dole et al. 2006; Ménard et al. 2010). (About 6% of the baryons at $z \sim 0$ are in stars; Moustakas et al. 2013.) Without dust, the cosmic IR background would not exist and the cosmic optical background would be twice as bright.

In high-redshift galaxies, microscopic grains can have mass-to-luminosity ratios between 10^{-4} and 10^{-5} (Bussmann et al. 2009b). A dust mass that is a small fraction of a stellar mass nevertheless has an outsized effect on the spectral energy distribution of a galaxy—dust can compose less than 1% of a galaxy’s mass while being responsible for more than 90% of its luminosity. A high-redshift galaxy’s luminosity may be dominated by dust emission, but what creates and destroys the dust as this galaxy evolves?

Like stars, dust has a lifecycle. It is created by stars and in the interstellar medium (ISM), and destroyed by supernovae and in the ISM. Whether the lifecycle is dominated by the galaxy’s star formation history—dust created and destroyed by stars—or to more secular processes—dust created and destroyed in the ISM—is an open question, and one

which this thesis does not answer. (Dust that exists in the present-day Milky Way is a result of secular processes; Draine 2009.) We explore the questions of When? and Where? of dust in high-redshift galaxies with infrared emission that far surpasses UV and optical emission. Answering these questions is the first step in answering the hard question of How?

The transition of common galaxies from dusty to dust-poor manifests itself in the redshift distribution of galaxies' contributions to the cosmic IR background (CIB). Evolution of the background with redshift does not immediately imply that the emission from dust in high-redshift galaxies is more luminous than the emission from dust in low-redshift galaxies. (The effect might be due to observing lower rest-frame wavelengths at higher redshifts.) That common high-redshift galaxies have higher IR luminosities than common low-redshift galaxies is well-established from other evidence, mainly luminosity functions (Magnelli et al. 2013). The redshift distribution of the background does constrain when dust grains were created and destroyed. Long wavelength portions of the CIB come from emission from large, cold dust grains. When do galaxies contribute most to the CIB at millimeter wavelengths? Though we do not resolve the total millimeter background, in chapter 2 we find that 60–88% of it comes from galaxies at $z > 1.3$.

Where is the dust in these galaxies? It might surround only the central region of a galaxy hosting an accreting supermassive black hole—in which case the lifecycle of dust is tied to the evolution of the black hole and its surroundings. We argue that this is not the case in chapter 3. Dust is not concentrated in a small number of regions in a galaxy; its lifecycle is tied to the evolution of the galaxy's stars and ISM. And while dust may be pervasive, its morphology is unconstrained, as we argue in chapter 5. Perhaps it is uniformly distributed; perhaps galactic regions with ionizing stars have more dust than regions with nonionizing stars.

In chapter 6 we discuss the answers to When? and Where? in the context of galaxy

evolution, and the future research that will further our understanding of the lifecycle of dust.

The results in chapter 2 are independent of cosmological parameters. In chapters 3 and 5, we assume a cosmology with $H_0 = 70 \text{ km s}^{-1} \text{ Mpc}^{-1}$, $\Omega_m = 0.3$, and $\Omega_\Lambda = 0.7$.

CHAPTER 2

REDSHIFT ORIGINS OF THE COSMIC MILLIMETER BACKGROUND

We present a study of the cosmic infrared background, which is a measure of the dust obscured activity in all galaxies in the Universe. We venture to isolate the galaxies responsible for the background at 1 mm; with spectroscopic and photometric redshifts we constrain the redshift distribution of the contribution to the background from these galaxies. We create a deep 1.16 mm map ($\sigma \sim 0.5$ mJy) by combining the AzTEC 1.1 mm and MAMBO 1.2 mm datasets in GOODS-N. This combined map contains 41 secure detections, 13 of which are new. By averaging the 1.16 mm flux densities of individually undetected galaxies with $24\mu\text{m}$ flux densities $> 25\mu\text{Jy}$, we resolve 31–45 percent of the 1.16 mm background. Repeating our analysis on the SCUBA $850\mu\text{m}$ map, we resolve a higher percentage (40–64 percent) of the $850\mu\text{m}$ background. A majority of the background resolved (attributed to individual galaxies) at both wavelengths comes from galaxies at $z > 1.3$. If the ratio of the resolved submillimeter to millimeter background is applied to a reasonable scenario for the origins of the unresolved submillimeter background, 60–88 percent of the total 1.16 mm background comes from galaxies at $z > 1.3$.

This chapter is adapted from Penner et al. (2011).

2.1 Motivation

The cosmic infrared background (CIB) is the total dust emission from all galaxies in the Universe. The contribution of galaxies to the background varies with redshift; this variation constrains the evolution over cosmic time of the output of dust obscured AGN activity and star formation. Decomposing the background into individual galaxies provides constraints as a function of redshift on the processes important to galaxy evolution, as well as the creation and destruction of large dust grains.

Models predict that a large fraction of the CIB at longer (sub)millimeter wavelengths comes from galaxies at high redshift (Gispert et al. 2000). The main evidence is that the SED of the (sub)mm background is less steep than the SED of a representative (sub)mm galaxy; the shallow slope of the background can be due to high-redshift galaxies, because the peak of their infrared SED shifts to observed (sub)mm wavelengths (Lagache et al. 2005). In this chapter we address the question, What galaxies are responsible for the CIB at $\lambda \sim 1$ mm and what is the redshift distribution of their contribution to the background?

Detecting a majority of the galaxies that contribute to the millimeter background is difficult, as maps are limited by confusion noise due to the large point spread functions of current single-dish mm telescopes. To resolve the ~ 1 mm background, we rely on a stacking analysis of galaxies detected at other wavelengths. Stacking is the process of averaging the millimeter flux density of a large sample of galaxies undetected in a millimeter map; the desired result is a high significance detection of the external sample as a whole (or in bins of flux density, redshift, etc.).

Stacking the (sub)mm flux density of galaxies is not a new methodology. Several studies seek to decompose the background at $850\mu\text{m}$ by stacking on SCUBA maps (Wang et al. 2006; Dye et al. 2006; Serjeant et al. 2008). These studies agree that the $850\mu\text{m}$ background is not completely resolved by current samples of galaxies; however, they reach contradictory conclusions on the redshift distributions of contributions from galaxies to the resolved background. Viero et al. (2013) stack on an AzTEC map and reach similar conclusions to those here regarding the decomposition of the background at 1.1 mm. (Their analysis was published after ours.) Stacking has been carried out on BLAST maps at 250, 350, and $500\mu\text{m}$ (Marsden et al. 2009; Devlin et al. 2009; Pascale et al. 2009; Chary & Pope 2010). As with stacking on any map with a large PSF, stacking on BLAST maps is subject to complications when the galaxies are angularly clustered. We take this issue into consideration in our analysis.

We combine the AzTEC 1.1 mm and MAMBO 1.2 mm maps in the GOODS-N field to create a deeper map at an effective wavelength of 1.16 mm (Perera et al. 2008; Greve et al. 2008). A significant advantage of the combined 1.16 mm map over the individual 1.1 mm and 1.2 mm maps is reduced noise. We investigate the contribution of galaxies with $24\mu\text{m}$ emission to the 1.16 mm background as a function of redshift. By stacking the same sample of galaxies on the SCUBA $850\mu\text{m}$ map in GOODS-N, we calculate the relative contribution of galaxies to the background at $850\mu\text{m}$ and 1.16 mm as a function of redshift. We infer the redshift distribution of the galaxies contributing to the remaining, unresolved 1.16 mm background.

2.2 Data

2.2.1 Creating the combined 1.16 mm map

There are two deep millimeter surveys of the Great Observatories Origins Deep Survey North region (GOODS-N; Dickinson et al. 2003). The AzTEC survey at 1.1 mm carried out on the JCMT (PSF FWHM = 19.5 arcsec) reaches a depth of $\sigma = 0.96\text{ mJy}$ over 0.068 deg^2 (Perera et al. 2008). The MAMBO survey at 1.2 mm carried out on the IRAM 30-m telescope (PSF FWHM = 11.1 arcsec) reaches a depth of $\sigma = 0.7\text{ mJy}$ over 0.080 deg^2 (Greve et al. 2008). The noise values refer to the uncertainty in determining the flux density of a point source. For more details on the individual maps, we refer the reader to those papers.

We create a combined mm map from a weighted average of the AzTEC 1.1 mm and MAMBO 1.2 mm maps. We use the PSF-convolved maps that are on the same RA and Dec grid with the same pixel size ($2\text{ arcsec} \times 2\text{ arcsec}$).

The weighted average flux density in a pixel in the combined mm map is:

$$S_{\text{measured}} = \frac{\frac{w_A S_A}{\sigma_A^2} + \frac{w_M S_M}{\sigma_M^2}}{\frac{w_A}{\sigma_A^2} + \frac{w_M}{\sigma_M^2}}, \quad (2.1)$$

where S_A and σ_A are the measured flux density and noise in the AzTEC 1.1 mm map, S_M and σ_M are the measured flux density and noise in the MAMBO 1.2 mm map, and the w 's are constants.

The noise in each pixel from Eq. 2.1 is:

$$\sigma = \frac{\sqrt{\frac{w_A^2}{\sigma_A^2} + \frac{w_M^2}{\sigma_M^2}}}{\frac{w_A}{\sigma_A^2} + \frac{w_M}{\sigma_M^2}}. \quad (2.2)$$

Use of the inverse variance weights in combining the two maps results in the map with minimum noise. We are instead interested in the resulting map with the *maximum* signal-to-noise ratio (SNR) of the sources, whether these sources are above or below some detection threshold. We introduce additional weights, w_A and w_M , which are constant multiplicative factors for the two individual maps. To rephrase the justification for these w 's in astrophysical terms: at (sub)millimeter wavelengths the spectral energy distributions (SEDs) of galaxies fall off $\propto \nu^{2+\beta}$ (a Rayleigh-Jeans fall off with emissivity index β); the flux density at 1.1 mm is higher than that at 1.2 mm. A simple inverse variance weighted average ($w_A = w_M$) does not account for this.

The optimal w 's come from iteratively maximizing the SNR of the detections in the resulting combined map. (In practice, we maximize the number of detections above 3.8σ .) The two values are $[w_A, w_M] = [0.56, 0.44]$. Given these w 's, the inverse variance weights, and that the transmission curves for the individual maps shown in Fig. 2.1 overlap, the central wavelength of the combined map is 1.16 mm. In the absence of *any* weighting the combined map has an effective wavelength of 1.15 mm. Weighting the individual maps results in a small shift of the central wavelength of the combined map to 1.16 mm.

The combined 1.16 mm map has 2 significant advantages over the individual 1.1 mm and 1.2 mm maps: (1) reduced noise (by roughly $\sqrt{2}$); and (2) increased reliability of secure detections. The AzTEC and MAMBO catalogs include some spurious detections (Perera et al. 2008; Greve et al. 2008); by combining the two (independent) maps, the

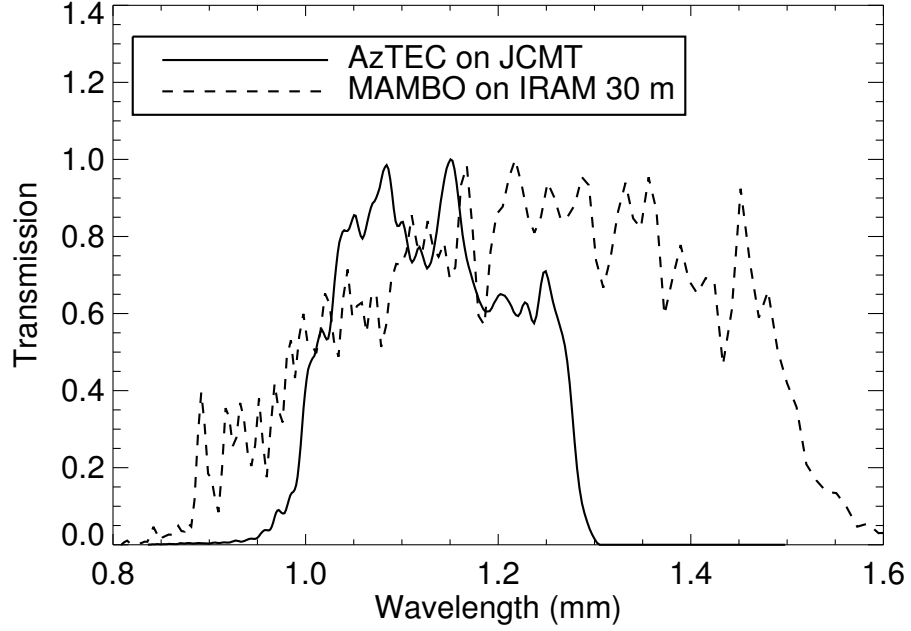


Figure 2.1 Transmission curves for the AzTEC and MAMBO detectors on their respective telescopes.

secure detections in the resulting map may be more reliable (this is the expectation).

The penalties to pay for these advantages are that the FWHM of the PSF and the effective wavelength vary slightly across the 1.16 mm map. We could smooth the two individual raw maps to the same PSF resolution at the expense of decreased SNR in each pixel. As the weights, w_A/σ_A^2 and w_M/σ_M^2 , change from pixel to pixel, we average different proportions of AzTEC 1.1 mm and MAMBO 1.2 mm flux densities. Fig. 2.2 shows the distributions of *normalized* weights (defined in the legend) from Eq. 2.1 for pixels with $\sigma < 1$ mJy in the combined 1.16 mm map. The majority of pixels in the combined map are in a small range of normalized weights (~ 0.4 for the AzTEC map, ~ 0.6 for the MAMBO map); the variation in FWHM and effective wavelength is small. We calculate the central wavelength of the combined map using the normalized weights

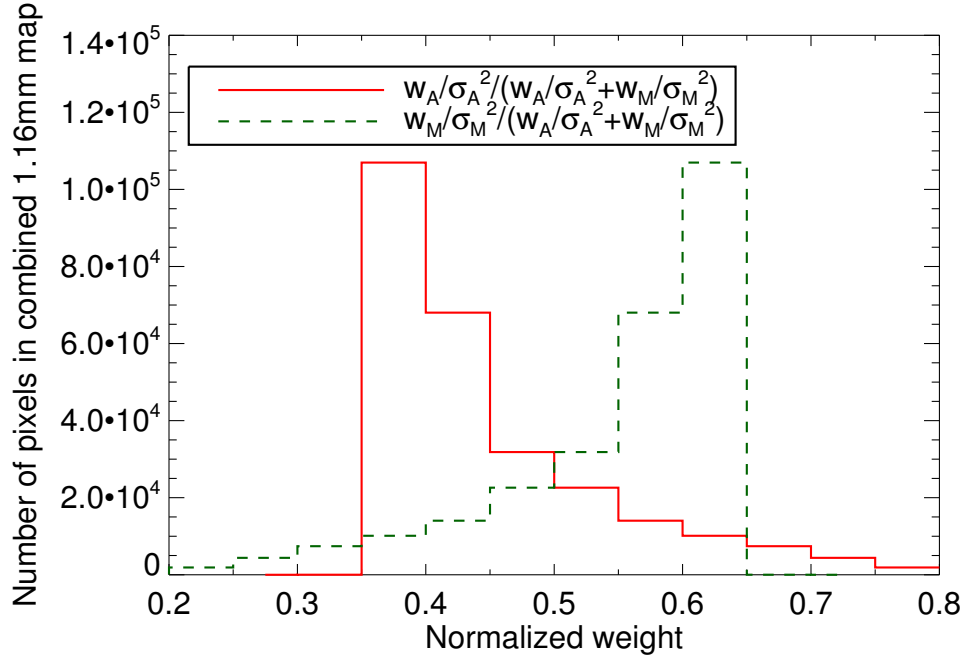


Figure 2.2 Distribution of normalized weights (Eq. 2.1) for pixels with $\sigma < 1$ mJy in the combined 1.16 mm map. The normalized weights applied to the AzTEC and MAMBO maps for each pixel sum to 1, so the histograms are symmetric about 0.5.

and the quoted wavelengths of the two individual maps. The distribution of stacked flux densities for randomly chosen pixels in the combined map has zero mean, as expected based on the individual maps (§2.3).

The area in our combined 1.16 mm map with $\sigma < 1$ mJy is 0.082 deg^2 . We use the overlap between this region and the area covered by the $24 \mu\text{m}$ sources (0.068 deg^2) for the stacking analysis. While we focus on stacking using the combined 1.16 mm map due to its uniform depth (reaching $\sigma \sim 0.5$ mJy), we also compare the stacking results using the SCUBA $850 \mu\text{m}$ survey of the GOODS-N region. The cleaned (of secure detections) $850 \mu\text{m}$ map has a nonuniform, non-contiguous 0.031 deg^2 area with $0.5 < \sigma < 5$ mJy (Pope et al. 2005). We ensure that both the clean and full SCUBA maps have a mean flux

density of 0 mJy in the area with $24\mu\text{m}$ sources.

Our terminology is as follows: *map* refers to a map convolved with its PSF, except when prefaced with ‘raw’; *secure detections* are directly detected sources in the mm map—non-spurious sources in the AzTEC 1.1 mm and MAMBO 1.2 mm maps, and sources with $\text{SNR} \geq 3.8$ in the combined 1.16 mm map (see §2.2.2 for a justification of this threshold); hereafter, when we use the word *sources* we mean sources in an external catalog that are not detected in the mm maps. A *cleaned* map has all secure detections subtracted before convolution with the PSF (§2.3.2), whereas a *full* map contains the secure detections. The combined 1.16 mm map is publicly available at http://www.astro.umass.edu/~pope/goodsn_mm/.

2.2.2 Verifying the 1.16 mm map

We find detections in the combined 1.16 mm map by searching for peaks in the SNR map. As the SNR threshold is decreased, there is an increased probability that some detections are spurious. Perera et al. (2008) and Greve et al. (2008) determine which detections in their AzTEC 1.1 mm and MAMBO 1.2 mm maps are most likely spurious; most spurious detections have SNR (before deboosting) < 3.8 . Only 5 secure detections have SNR (before deboosting) < 3.8 . We use this SNR threshold to make our secure detection list for the combined map. Positions and measured flux densities of secure 1.16 mm detections are given in Table 2.1.

Table 2.1. Secure detections in the 1.16 mm map

Number	RA	Dec	S_{measured} mJy	σ mJy	SNR	$S_{\text{deboosted}}$ mJy	AzTEC ID	MAMBO ID
1	189.299114	62.369436	10.26	0.68	15.0	...	AzGN01	GN1200.1
2	189.137896	62.235510	5.24	0.57	9.1	5.2	AzGN03	GN1200.2
3	189.378717	62.216051	4.51	0.55	8.2	4.4	AzGN05	GN1200.4
4	189.297686	62.224436	4.09	0.54	7.6	3.9	AzGN07	GN1200.3
5	189.132927	62.286617	4.22	0.56	7.5	4.1	AzGN02	GN1200.13
6	189.112273	62.101043	4.81	0.67	7.2	4.5	AzGN06	GN1200.5
7	188.959560	62.178029	5.00	0.71	7.0	4.6	AzGN04	GN1200.12
8	189.308576	62.307210	3.46	0.57	6.1	3.1	AzGN26	GN1200.6
9	189.149018	62.119408	3.35	0.61	5.5	2.9	AzGN11	GN1200.14
10	189.190353	62.244432	3.02	0.56	5.4	2.6	AzGN08	...
11	188.973386	62.228058	3.10	0.60	5.1	2.6	AzGN13	GN1200.15
12	189.184207	62.327207	3.03	0.59	5.1	2.5	AzGN28	GN1200.9
13	189.138377	62.105511	3.31	0.66	5.0	2.7	AzGN12	...
14	189.213067	62.204995	2.88	0.57	5.0	2.4	AzGN14	GN1200.25
15	189.501924	62.269772	3.26	0.66	4.9	2.7	AzGN21	...
16	189.202112	62.351658	3.05	0.63	4.8	2.5
17	189.214098	62.339995	2.88	0.60	4.8	2.3
18	189.068612	62.254326	2.61	0.55	4.7	2.1	AzGN16	...
19	189.300036	62.203880	2.59	0.55	4.7	2.1	...	GN1200.29
20	189.114187	62.203822	2.61	0.57	4.6	2.1	AzGN10	...
21	189.407721	62.292688	2.62	0.58	4.5	2.1	AzGN09	...
22	189.400013	62.184363	2.63	0.58	4.5	2.1	...	GN1200.17
23	189.440268	62.148758	3.84	0.85	4.5	2.8
24	189.035270	62.244279	2.46	0.56	4.4	1.9	AzGN24	...
25	189.575648	62.241841	3.56	0.82	4.3	2.6
26	188.951634	62.257458	2.84	0.66	4.3	2.1	AzGN15	...
27	189.421566	62.206005	2.41	0.57	4.3	1.9	AzGN18	...
28	188.942743	62.192993	3.09	0.73	4.3	2.3
29	189.216774	62.083885	3.74	0.88	4.2	2.6	AzGN25	...
30	188.920762	62.242944	3.01	0.71	4.2	2.2	AzGN17	...
31	189.323691	62.133314	2.74	0.67	4.1	2.0	...	GN1200.23

Table 2.1 (continued)

Number	RA	Dec	S_{measured} mJy	σ mJy	SNR	$S_{\text{deboosted}}$ mJy	AzTEC ID	MAMBO ID
32	189.033574	62.148164	2.42	0.60	4.0	1.8	...	GN1200.7
33	189.090016	62.268797	2.23	0.56	4.0	1.7
34	189.143551	62.322737	2.44	0.61	4.0	1.8
35	189.258342	62.214444	2.19	0.55	4.0	1.6
36	189.039961	62.255953	2.21	0.56	4.0	1.6
37	188.916328	62.212377	2.97	0.75	4.0	2.1
38	189.327507	62.231090	2.12	0.54	3.9	1.6
39	189.020746	62.114810	2.71	0.70	3.9	1.9	AzGN19	...
40	189.238057	62.279444	2.14	0.56	3.8	1.5
41	189.550659	62.248008	2.78	0.73	3.8	1.9

Note. — Columns: RA and Dec are in decimal degrees, and are reported from the center of the pixel with maximum SNR ($S_{\text{measured}}/\sigma$). S_{measured} and σ are the measured flux density and noise in the 1.16 mm map, and $S_{\text{deboosted}}$ is the deboosted flux density calculated with Eq. 2.3. The AzTEC ID is from Perera et al. (2008), the MAMBO ID is from Greve et al. (2008).

Flux boosting is an important issue for detections at low SNR thresholds, particularly when the differential counts distribution (dN/dS) is steep, so that it is more likely for a faint detection’s flux density to scatter up than for a bright detection’s flux density to scatter down. Flux deboosting is a statistical correction to the measured flux density of a secure detection (Hogg & Turner 1998). The deboosting correction relies on a simulated map using a model of the differential counts distribution (see Coppin et al. 2005). A simulation of the 1.16 mm map is subject to large uncertainties because we do not have exact knowledge of the PSF, so we choose to deboost the flux densities of secure detections empirically.

To verify our method of combining the two maps, we want to compare the deboosted flux densities of secure detections in the 1.16 mm map with their deboosted flux densities

in the 1.1 mm and 1.2 mm maps. Our approach to obtain empirically deboosted flux densities is to fit a function that relates the *deboosted* flux densities of secure detections in the 1.1 mm and 1.2 mm maps to the *measured* flux densities and noise values in those maps. We then use the derived formula to estimate empirically deboosted flux densities for the secure 1.16 mm detections from the measured 1.16 mm flux densities and noises. We find

$$S_{\text{deboosted}} = 1.55 S_{\text{measured}}^{0.89} - 2.7 \sigma, \quad (2.3)$$

where S_{measured} and σ are in mJy. For the secure AzTEC 1.1 mm and MAMBO 1.2 mm detections, the residuals between the deboosted flux densities from this relation and the deboosted flux densities in Perera et al. (2008) and Greve et al. (2008) have a standard deviation of 0.1 mJy, an error well below the flux density noise values in all mm maps. This formula is only valid in the range of SNR covered by the AzTEC and MAMBO detections, so we do not deboost the flux density of source 1 (a 15σ source). Table 2.1 lists the deboosted flux densities for the secure 1.16 mm detections using this relation. For the main purposes of this paper, flux deboosting is not necessary since we stack the 1.16 mm flux densities of sources we know to exist from other observations.

Fig. 2.3 shows the comparison between deboosted flux densities for secure 1.16 mm and 1.1 mm detections. The combined 1.16 mm map recovers the majority of secure detections identified in the AzTEC 1.1 mm map—the arrows pointing down show that there are 4 secure detections in the AzTEC map that are not secure detections in the combined map.

Fig. 2.4 shows the comparison between deboosted flux densities for secure 1.16 mm and 1.2 mm detections. There are 14 secure detections in the MAMBO 1.2 mm map that are not coincident with secure detections in the combined 1.16 mm map (the down arrows in the right panel). However, the upper limits to the flux densities in the combined map are within the scatter about the solid line.

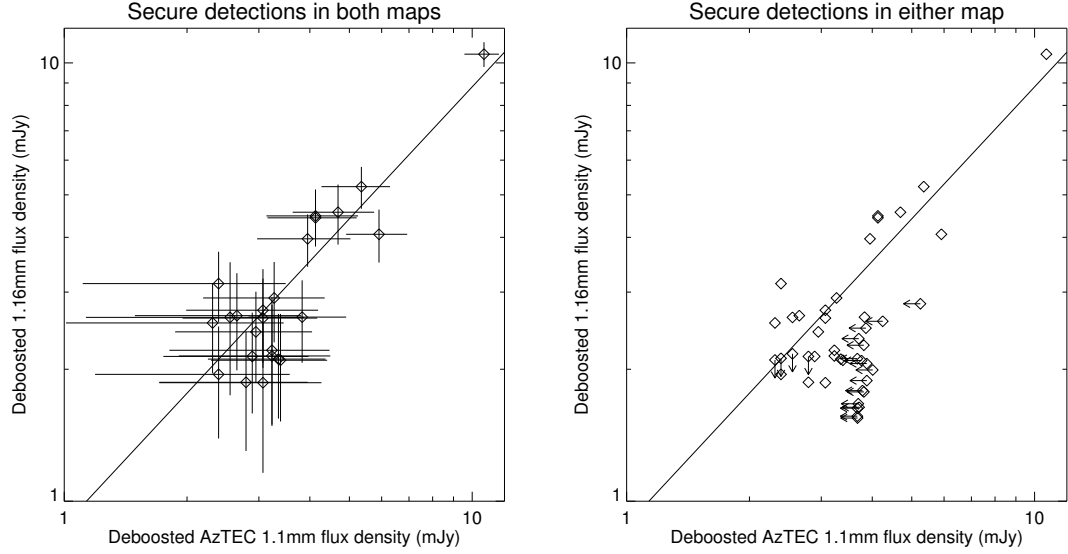


Figure 2.3 *Left panel:* Empirically deboosted combined 1.16 mm flux density ($S_{\text{deboosted}}$) as a function of deboosted AzTEC 1.1 mm flux density ($S_{\text{A,deboosted}}$) for detections that are secure in both maps. The solid line is the best-fitting line to the deboosted flux densities of secure detections ($S_{\text{deboosted}} = 0.88S_{\text{A,deboosted}}$). *Right panel:* A comparison of deboosted flux densities for secure detections in either map. If a secure 1.16 mm detection does not coincide with a secure AzTEC 1.1 mm detection, a 3.8σ upper limit on the AzTEC 1.1 mm flux density is plotted. Similarly, if a secure AzTEC 1.1 mm detection does not coincide with a secure 1.16 mm detection, a 3.8σ upper limit on the 1.16 mm flux density is plotted.

The comparisons in Figs. 2.3 and 2.4 lead us to conclude that our method of combining the AzTEC 1.1 mm and MAMBO 1.2 mm maps is effective. The combined 1.16 mm map has 13 new secure detections (Table 2.1). We do not expect the new detections to be in the individual maps.

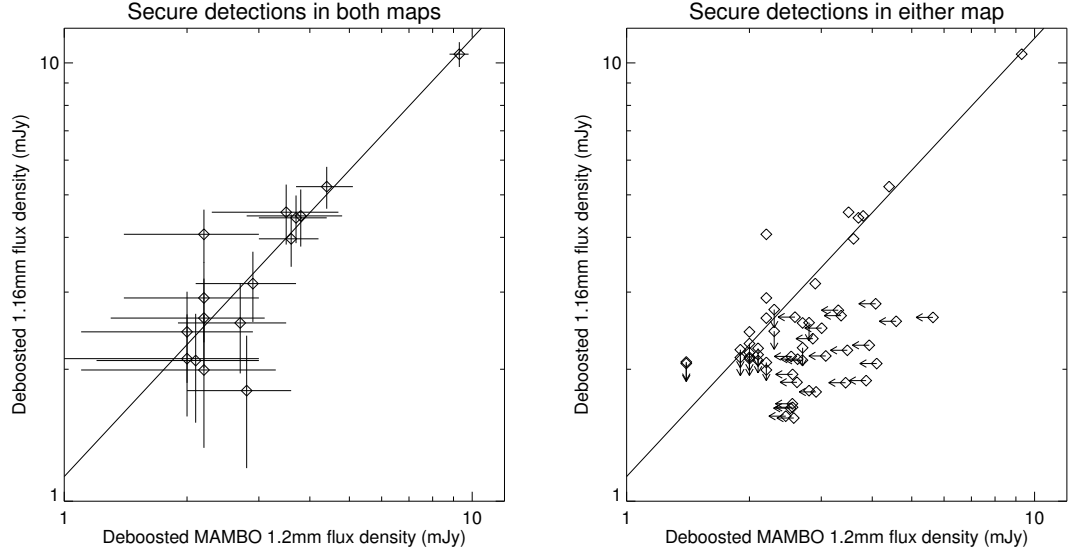


Figure 2.4 *Left panel*: Empirically deboosted combined 1.16 mm flux density ($S_{\text{deboosted}}$) as a function of deboosted MAMBO 1.2 mm flux density ($S_{\text{M,deboosted}}$) for detections which are secure in both maps. The solid line is the best-fitting line to the deboosted flux densities of secure detections ($S_{\text{deboosted}} = 1.14S_{\text{M,deboosted}}$). *Right panel*: A comparison of deboosted flux densities for secure detections in either map. If a secure 1.16 mm detection does not coincide with a secure MAMBO 1.2 mm detection, a 3.8σ upper limit on the MAMBO 1.2 mm flux density is plotted. Similarly, if a secure MAMBO 1.2 mm detection does not coincide with a secure 1.16 mm detection, a 3.8σ upper limit on the 1.16 mm flux density is plotted. Based on this figure and Fig. 2.3, we conclude that our method of combining the AzTEC 1.1 mm and MAMBO 1.2 mm maps is valid.

2.2.3 Sample

Galaxies with detected $24\mu\text{m}$ emission compose the most homogeneous set of dusty galaxies whose mm flux density can be stacked with significant results. We use the $24\mu\text{m}$ catalog from the *Spitzer*/MIPS survey of GOODS-N. The catalog has a uniform depth of $\sigma \sim 5\mu\text{Jy}$ in the regions of interest; the $24\mu\text{m}$ fluxes are measured at the positions of

IRAC sources, so this catalog pushes to faint $24\mu\text{m}$ fluxes. We only stack $\geq 3\sigma$ $24\mu\text{m}$ sources with $S_{24} > 25\mu\text{Jy}$. At flux densities above $50\mu\text{Jy}$, the catalog is 99 percent complete; for $25 < S_{24} < 50\mu\text{Jy}$, the catalog is 83 percent complete (Magnelli et al. 2009). Completeness corrections to our results are negligible, so we do not apply them. We exclude sources that lie in the region of the 1.16 mm map with $\sigma > 1\text{ mJy}$; in this region, the noise is nonuniform. The final $24\mu\text{m}$ catalog for stacking has 2484 sources in 0.068 deg^2 .

To decompose the contribution to the mm background from $24\mu\text{m}$ sources as a function of redshift, we require either a photometric or spectroscopic redshift for each $24\mu\text{m}$ source. We start by matching a source with a spectroscopic redshift from the catalogs of Barger et al. (2008) and D. Stern (private communication) to each $24\mu\text{m}$ source. The match radius, 0.7 arcsec, is chosen by maximizing the number of unique matches while minimizing the number of multiple matches. We find spectroscopic redshifts for 1026 (41 percent of the) $24\mu\text{m}$ sources.

If no (or multiple) coincident sources with spectroscopic redshifts are found, we resort to the photometric redshift source catalog of M. Brodwin (private communication) to find a source match. Photometric redshifts are constrained with deep $UBVRIzJK$ imaging, and provide redshift estimates for 872, or 35 percent, of the $24\mu\text{m}$ sources. Photometric redshift uncertainties are small compared to the width of our redshift bins (we are interested in the contribution to the background from galaxies in large redshift bins). If no (or multiple) coincident sources with photometric redshifts are found, we assign the $24\mu\text{m}$ source to a ‘redshift unknown’ bin in the stacking analysis. Of the 2484 $24\mu\text{m}$ sources, 588 (24 percent) have no spectroscopic or photometric redshift estimate available.

2.3 Stacking analysis

Our stacking procedure depends on 2 fundamental properties of the (sub)mm maps.

1. *Every detection, and source, is a point source.* The PSFs are large; in all 3 maps the

full-width-half-maxima (FWHM) are > 10 arcsec. This property has a number of implications. To make low SNR detection-finding easy the raw maps are convolved with their PSFs. The result is a map where each pixel value is the flux density of a point source at the position of the pixel. To stack the millimeter flux densities of sources we require only the values of single pixels in the map.

2. *The means of the maps are 0 mJy.* These millimeter observations are taken, filtered, and reduced in such a way that the sum of all pixel values in the map is zero. In other words, the most likely value of a randomly chosen pixel is 0 mJy, a useful statistical property we explore in §2.3.1. However, the large PSF forces us to carefully consider the effects of having multiple sources clustered in the area covered by one PSF (also in §2.3.1).

Stacking is the process of averaging the flux density, at some wavelength (1.16 mm), of sources detected at another wavelength. To resolve the (sub)mm background, we want to stack a catalog of sources whose emission correlates strongly with 1.16 mm emission, and we want this catalog to have a large number of sources. A catalog that meets these requirements has galaxies selected on dust emission at both low and high redshift. We do not expect a sample of stellar mass selected sources—for example, $3.6\mu\text{m}$ sources—to be efficient at isolating the galaxies responsible for the mm background, because $3.6\mu\text{m}$ sources are a mix of dusty and dust-poor galaxies. The MIPS catalog of $24\mu\text{m}$ sources is selected on dust emission to high redshift and there are known correlations between the flux densities at mid-infrared and far-infrared wavelengths (Chary & Elbaz 2001).

The stacking equation we use is similar to Eq. 2.1:

$$S_{\text{bin}} = \frac{\sum_{i=1}^{N_{\text{bin}}} \frac{S_{i,1.16}}{\sigma_{i,1.16}^2}}{\sum_{i=1}^{N_{\text{bin}}} \frac{1}{\sigma_{i,1.16}^2}}, \quad (2.4)$$

where S_{bin} is the stacked flux density of N_{bin} sources in a bin of $24\mu\text{m}$ flux density or redshift and $S_{i,1.16}$ and $\sigma_{i,1.16}$ are the measured 1.16 mm flux density and noise at the

position of the i -th $24\mu\text{m}$ source. This equation does not include any constant terms (w 's) because the goal of stacking is to get an average flux density for all sources from a map at one wavelength. The noise decreases with the inclusion of more sources:

$$\sigma_{\text{bin}} = \frac{1}{\sqrt{\sum_{i=1}^{N_{\text{bin}}} \frac{1}{\sigma_{i,1.16}^2}}}. \quad (2.5)$$

In a mathematical sense, this equation is only valid when all of the $\sigma_{i,1.16}$ are independent; because there are many $24\mu\text{m}$ sources in the area of one PSF, this requirement is strictly not met. We fit a Gaussian to the distribution of stacked flux densities for 2484 random pixels, and the σ is the same as the σ_{bin} we calculate for the $24\mu\text{m}$ sources using Eq. 2.5. We choose $N_{\text{bin}} \sim 220$ sources when binning by $24\mu\text{m}$ flux density and $N_{\text{bin}} \sim 660$ sources when binning by redshift. These numbers allow adequate SNR for the stacked flux density in each bin. The redshift bins are larger than the flux density bins because we want a differential contribution from the sources in each redshift bin, whereas we want a cumulative contribution from the sources in each flux density bin. The contribution to the 1.16 mm background from each bin is $N_{\text{bin}} S_{\text{bin}}/A$, where A is the area. The overlap between the 1.16 mm map area with $\sigma < 1$ mJy and the $24\mu\text{m}$ exposure map defines A (0.068 deg^2).

2.3.1 The effects of angular clustering on stacking analyses

The undetected mm emission from a $24\mu\text{m}$ source covers the area of the mm PSF, so a natural question to ask is, What happens to the stacked mm flux density when there are multiple $24\mu\text{m}$ sources in the area encompassed by one mm PSF? We revisit the fundamental properties of the mm maps to answer this question.

Consider a randomly distributed population of sources. We are interested in the best estimate of the mm flux density of source A, a source with many neighbors. We remember that 0 mJy is the most likely flux density of a randomly chosen pixel. An equivalent statement is that the total flux density at the position of A from all of A's randomly distributed

neighbors is 0 mJy. There are a few neighbors with angular separations small enough to contribute positive flux density at the position of A, but there are many more neighbors with angular separations that are large enough to contribute negative flux density at the position of A. *If we have randomly distributed sources in the area covered by the mm PSF, the true flux densities of the sources are the measured flux densities in the mm map.* Marsden et al. (2009) prove that in the case of randomly distributed sources, stacking is a measure of the covariance between the stacked catalog and the (sub)mm map.

Let us consider a population of sources that is *not* randomly distributed—a population that is angularly clustered (as we expect the $24\mu\text{m}$ sources to be). If the clustering is significant at angular separations where the PSF is positive, and if it is negligible at larger angular separations, the positive contribution at the position of A from the many sources that have small angular separations is not canceled out by the negative contribution from the sources that have large angular separations. In this case, the measured flux density of A is higher than the true flux density. We cannot blindly stack multiple sources in the same PSF area. The stacked flux density of angularly clustered sources near secure detections is overestimated for the same reason. The ratio of the measured flux densities to the true flux densities for an ensemble of sources is a function of the angular clustering strength of the sources, the flux densities at the wavelength we stack at, and the size of the PSF (Béthermin et al. 2010). We detail our simulation to compute this ratio for the $24\mu\text{m}$ sources and the (sub)mm PSF in §2.3.2. We further consider the angular clustering of sources with secure (sub)mm detections; the tests we perform suggest that this angular clustering is the dominant source of overestimating the stacked flux density.

The aim of the next section is to investigate the impact of angular clustering on the the stacked (sub)mm flux densities of $24\mu\text{m}$ sources. Using a similar analysis, Chary & Pope (2010) conclude that clustering leads to a significant overestimate of the flux density when stacking on BLAST (sub)mm maps with larger PSFs than those for the SCUBA $850\mu\text{m}$

and 1.16 mm maps.

The angular clustering of $24\mu\text{m}$ sources is uncertain, though spatial clustering measurements exist (Gilli et al. 2007). The assumption we test is that this spatial (three dimensional) clustering projects to an angular (two dimensional) clustering, which may lead to an overestimate of the stacked flux density.

2.3.2 Quantifying the effects of angular clustering

The 2 tests of our assertion of angular clustering are:

1. An estimate of the ratio of measured flux densities to true flux densities for a simulated map composed solely of $24\mu\text{m}$ sources. This test quantifies the effect of angular clustering of $24\mu\text{m}$ sources in the area of one PSF. Here, *true* flux density is an input flux density and *measured* flux density is an output flux density (after the simulation).
2. A comparison of the resolved background from stacking on a cleaned map with the resolved background from stacking on a full map. This test helps address the effect of angular clustering of $24\mu\text{m}$ sources with secure (sub)mm detections.

Both tests require a well-characterized PSF: for the first, to create a realistic simulated map, and for the second, to subtract the secure (sub)mm detections to create a clean map. The 1.16 mm map does not have a well-characterized PSF so we perform the tests for the Perera et al. (2008) AzTEC 1.1 mm map, with an area, 0.070 deg^2 , defined by $\sigma < 1\text{ mJy}$. We also run the tests for the SCUBA $850\mu\text{m}$ map, with an area, 0.031 deg^2 , defined by $\sigma < 5\text{ mJy}$.

2.3.2.1 The first test

Our first test is a simulation of an AzTEC 1.1 mm map composed exclusively of $24\mu\text{m}$ sources. Using the relation between $24\mu\text{m}$ flux density and stacked 1.1 mm flux density—the differential form of Fig. 2.7—we insert best estimates of the 1.1 mm flux densities at

the positions of all the $24\mu\text{m}$ sources. This process preserves the angular clustering of the real $24\mu\text{m}$ sources. We convolve the simulated map with the AzTEC PSF, and remeasure the 1.1 mm flux densities by stacking. The stacked flux density, multiplied by the number of sources, is the *measured* flux density of the entire sample, while the *true* flux density is the sum of the inserted flux densities. The ratio of total measured flux density to total true flux density is ~ 1.08 . Due to angular clustering of multiple sources within the average PSF, the stacked 1.1 mm flux density of $24\mu\text{m}$ sources appears to be overestimated by ~ 8 percent. Different relations between $24\mu\text{m}$ flux density and 1.1 mm flux density that are physically motivated—for example, by Chary & Elbaz 2001—produce comparable ratios. This 8 percent correction to the stacked 1.1 mm flux density is within the uncertainties of the relation between $24\mu\text{m}$ and 1.1 mm flux densities.

An alternative test is an extension of the deblending method in Greve et al. (2010) and Kurczynski & Gawiser (2010). Deblending is the simultaneous solution of a system of Q equations that are mathematical descriptions of the flux densities of blended, angularly clustered sources (Q is the number of sources to be stacked, see §5.2 and fig. 5 in Greve et al. 2010). The result of deblending is a vector of the true source flux densities. Our extension of the methods in Greve et al. (2010) and Kurczynski & Gawiser (2010) generalizes the equations by not assuming a Gaussian PSF—which does not have the negative parts that are important for the data we consider here—but instead uses the AzTEC PSF for deblending the sources in the AzTEC map. Our extension does not account for $24\mu\text{m}$ undetected sources that may affect the stacked 1.1 mm flux of $24\mu\text{m}$ sources. This deblending procedure gives the same answer as our simulations: an 8 percent overestimation of the stacked 1.1 mm flux density.

2.3.2.2 The second test

Our procedure for cleaning the raw AzTEC 1.1 mm map is: (1) for each secure 1.1 mm detection, scale the PSF to the deboosted flux density; (2) subtract the scaled PSFs from

Table 2.2. The effects of angular clustering on the resolved background

Map	850 μm bkg Jy deg^{-2}	1.1 mm bkg Jy deg^{-2}
Full	27.0 ± 1.6	9.7 ± 0.9
Cleaned	12.5 ± 1.6	7.4 ± 0.9
Cleaned w/detections	21.1 ± 1.7	9.2 ± 0.9

the raw map; and (3) convolve the residual map with the PSF. There are two components to the resolved 1.1 mm background: the contribution to the background from stacking $24 \mu\text{m}$ sources, and the contribution to the background from the secure 1.1 mm detections cleaned from the map. The latter is calculated by summing the deboosted flux densities of all the secure detections and dividing by the area.

We compare the 1.1 mm background resolved from stacking on the full and cleaned maps in Fig. 2.5 (values in Table 2.2). A stack of $24 \mu\text{m}$ sources on the full map, when compared to a stack on the cleaned map, does *not* significantly overestimate the resolved 1.1 mm background.

Fig. 2.5 implies the clustering of $24 \mu\text{m}$ sources with the secure detections in the 1.16 mm map will have a small effect on the stacked flux density, although we note that the combined 1.16 mm map does have more secure detections (in a larger area with $\sigma < 1 \text{ mJy}$) than the AzTEC 1.1 mm map.

The cleaned 850 μm map is from Pope et al. (2005). We compare the 850 μm background resolved from stacking on the full and cleaned maps in Fig. 2.6. The blue diamonds (values in Table 2.2) show that a stack of $24 \mu\text{m}$ sources on the full 850 μm map

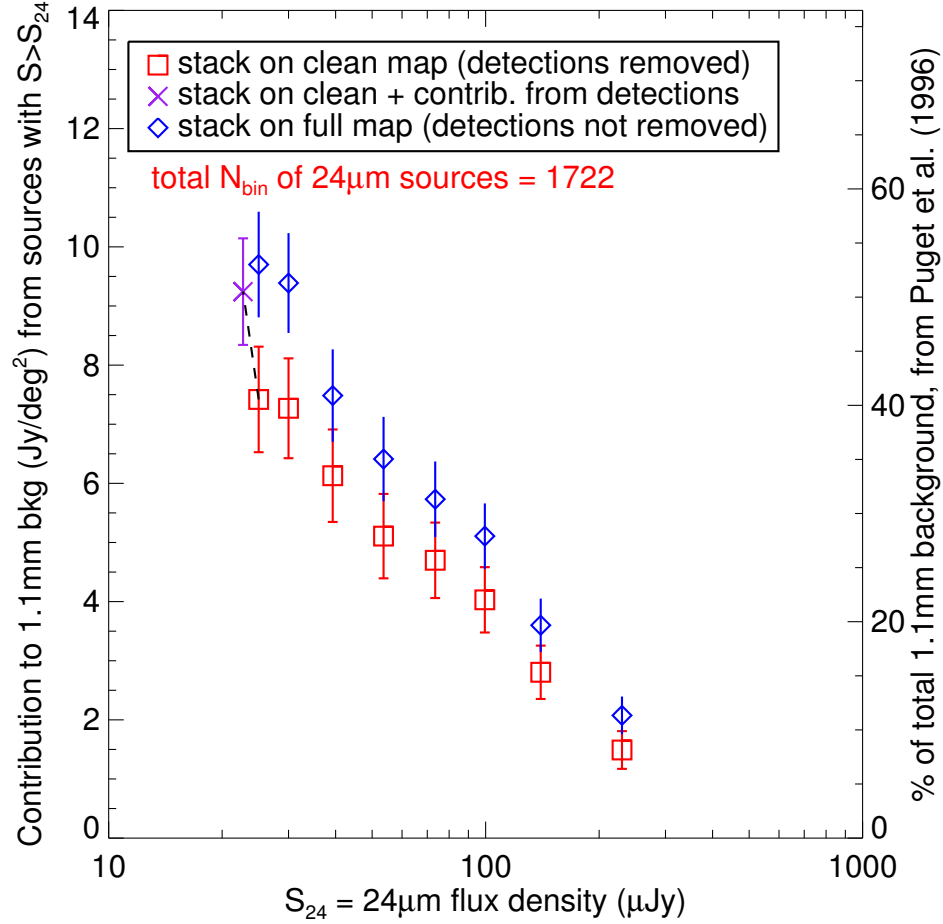


Figure 2.5 The resolved 1.1 mm background from $24\mu\text{m}$ sources with flux densities $> S_{24}$. The red squares are a stack on the cleaned map; the blue triangles are a stack on the full map. The purple ‘X’ includes the contribution to the background from the secure 1.1 mm detections, arbitrarily added to the faintest cumulative flux density bin, after stacking on the cleaned map. Angular clustering of $24\mu\text{m}$ sources with secure 1.1 mm detections does not appear to cause a significant overestimate of the resolved 1.1 mm background.

overestimates the resolved submm background, when compared to a stack on the cleaned map. We hesitate to attribute the entire difference to angular clustering of $24\mu\text{m}$ sources

with the secure $850\mu\text{m}$ detections. The difference is probably due to many effects:

1. Oversubtraction of the secure $850\mu\text{m}$ detections in making the cleaned map. Detections are subtracted using measured, rather than deboosted, flux densities. To estimate the magnitude of this oversubtraction we clean the raw AzTEC 1.1 mm map using both measured and deboosted flux densities for the secure 1.1 mm detections, and find a marginal difference in the resolved 1.1 mm background between the two methods. The average deboosting correction—roughly 30% of the measured flux subtracted off (Perera et al. 2008; Pope et al. 2006)—is similar for both the $850\mu\text{m}$ and 1.1 mm detections. Combined with the marginal difference in resolved 1.1 mm background, the resolved $850\mu\text{m}$ background is probably insensitive to the oversubtraction of the secure $850\mu\text{m}$ detections in the cleaned map.
2. Oversubtraction of the secure $850\mu\text{m}$ detections in regions of the map close to the confusion limit. The measured and deboosted flux densities of the detections in the deepest parts of the $850\mu\text{m}$ map are not corrected for the contribution from blended sources below the detection limit. We compare the background resolved from stacking on the full and cleaned maps again, this time excluding regions around all detections with $\sigma < 1\text{ mJy}$; a large difference in the resolved background remains.
3. Nonuniform noise, which complicates interpretation of the results from the inverse-variance weighted stacking formula.
4. Different chop throws across the SCUBA map, which complicates the angular separations where we expect to see negative emission from detections.
5. Angular clustering of the $24\mu\text{m}$ sources with the secure $850\mu\text{m}$ detections.

A simulation of the $850\mu\text{m}$ map, similar to our first test except using *randomly distributed* sources drawn from a differential counts distribution (dN/dS) and an idealized SCUBA

PSF, implies that part of the difference may be due to effects other than angular clustering (for example, effects 1–4). If this simulation is correct, the stacked $850\mu\text{m}$ flux density is *underestimated* when using the cleaned map, and our estimate of the resolved $850\mu\text{m}$ background is a lower limit. However, the ratio of stacked $850\mu\text{m}$ to 1.16 mm flux density as a function of redshift (using the full $850\mu\text{m}$ map) requires a model SED with a higher dust temperature than 60 K (assuming an emissivity index β of 1.5). We therefore use the $850\mu\text{m}$ flux density from stacking on the cleaned map. With large, uniform maps from SCUBA-2 these issues can be tested and resolved. Until we have such maps, we cannot separate the effects of angular clustering and nonuniform noise.

In conclusion, we find that:

1. In the specific case of the $24\mu\text{m}$ sources and the 1.16 mm map and its PSF, the effects due to angular clustering are additional corrections within the statistical uncertainty of the stacked flux density.
2. We cannot separate the effect of angular clustering from the effect of nonuniform noise in the SCUBA $850\mu\text{m}$ map.

The results we present in §2.4 use the cleaned $850\mu\text{m}$ map, with the contribution from the secure $850\mu\text{m}$ detections added after stacking, and the full 1.16 mm map.

2.4 Results and discussion

The stacked 1.16 mm flux density as a function of cumulative $24\mu\text{m}$ source flux density is shown in Fig. 2.7. The combined 1.16 mm map values (blue diamonds) lie between the stacked flux densities for the individual maps, which provides another validation of our method of combining the AzTEC 1.1 mm and MAMBO 1.2 mm maps. The stack on the combined 1.16 mm map has smaller errors than the stacks on the individual maps, as anticipated from Eq. 2.2.

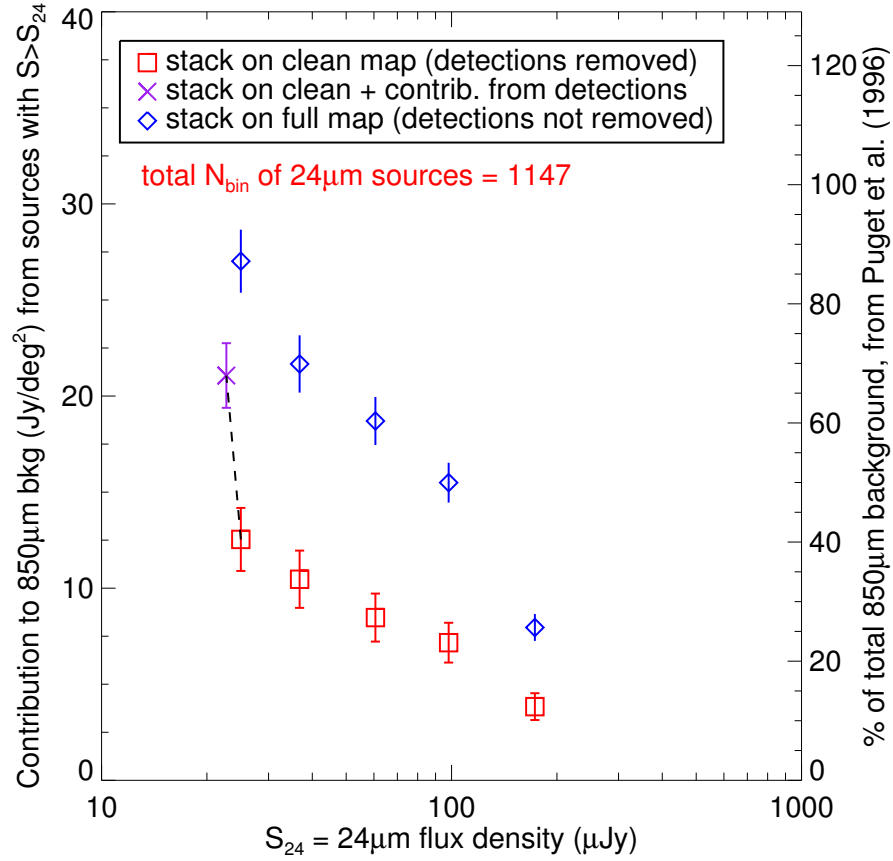


Figure 2.6 The resolved $850\mu\text{m}$ background from $24\mu\text{m}$ sources with flux densities $> S_{24}$. The red squares are a stack on the cleaned map; the blue diamonds are a stack on the full map. The purple ‘X’ includes the contribution to the background from the secure $850\mu\text{m}$ detections, arbitrarily added to the faintest cumulative flux density bin, after stacking on the cleaned map. In reality, the $24\mu\text{m}$ counterparts to the secure $850\mu\text{m}$ detections have flux densities ranging from $S_{24} \sim 20 - 700\mu\text{Jy}$ (Pope et al. 2006). We adopt the background values from stacking on the cleaned map.

We multiply the stacked flux density (Fig. 2.7) by the number of $24\mu\text{m}$ sources in the cumulative bin and divide by the area to get the contribution to the background (Fig. 2.8). The overlap between the 1.16 mm map area with $\sigma < 1\text{ mJy}$ and the $24\mu\text{m}$ exposure

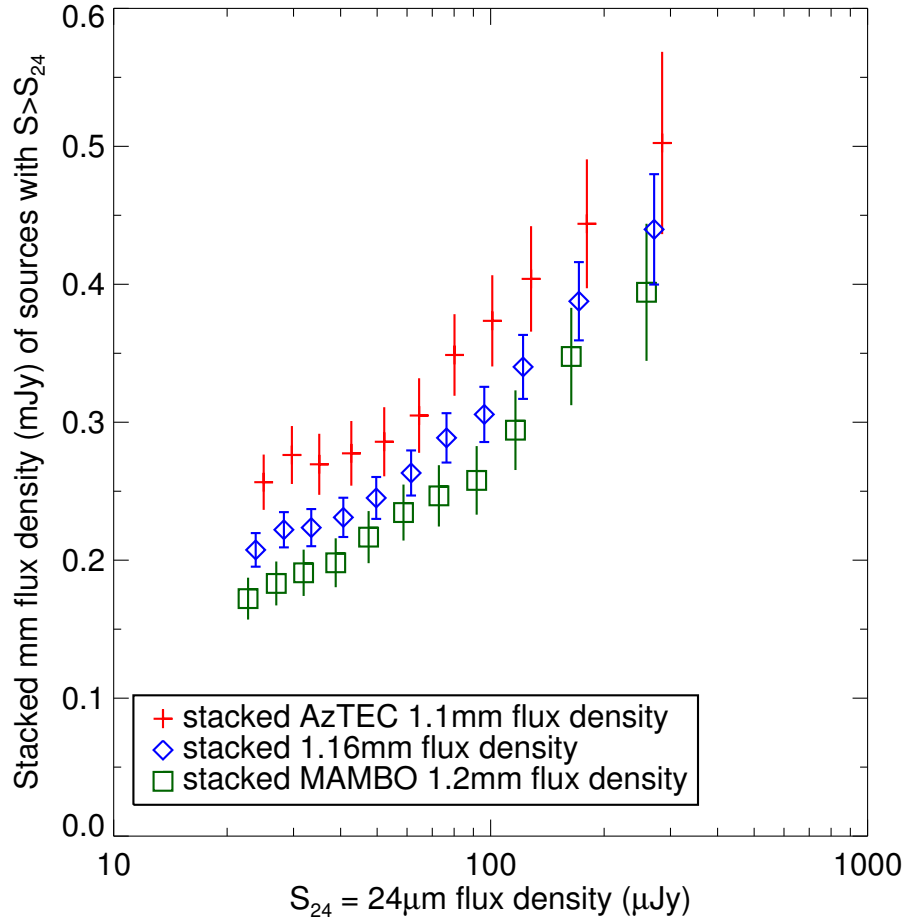


Figure 2.7 Stacked AzTEC 1.1 mm, combined 1.16 mm, and MAMBO 1.2 mm flux densities from $24\mu\text{m}$ sources with flux densities $> S_{24}$. The stacked 1.1 mm flux densities are higher than the stacked 1.2 mm flux densities, as expected for the SED of a typical dusty galaxy. The 1.16 mm flux density lies between and has smaller errors than the 1.1 mm and 1.2 mm flux densities.

map defines A (0.068 deg^2). The blue diamonds show that $24\mu\text{m}$ sources resolve $7.6 \pm 0.4\text{ Jy deg}^{-2}$ of the 1.16 mm background.

The observed background is measured using *COBE* maps. The total CIB at (sub)mm wavelengths is uncertain due to large scale variability of cirrus emission in the Galaxy that

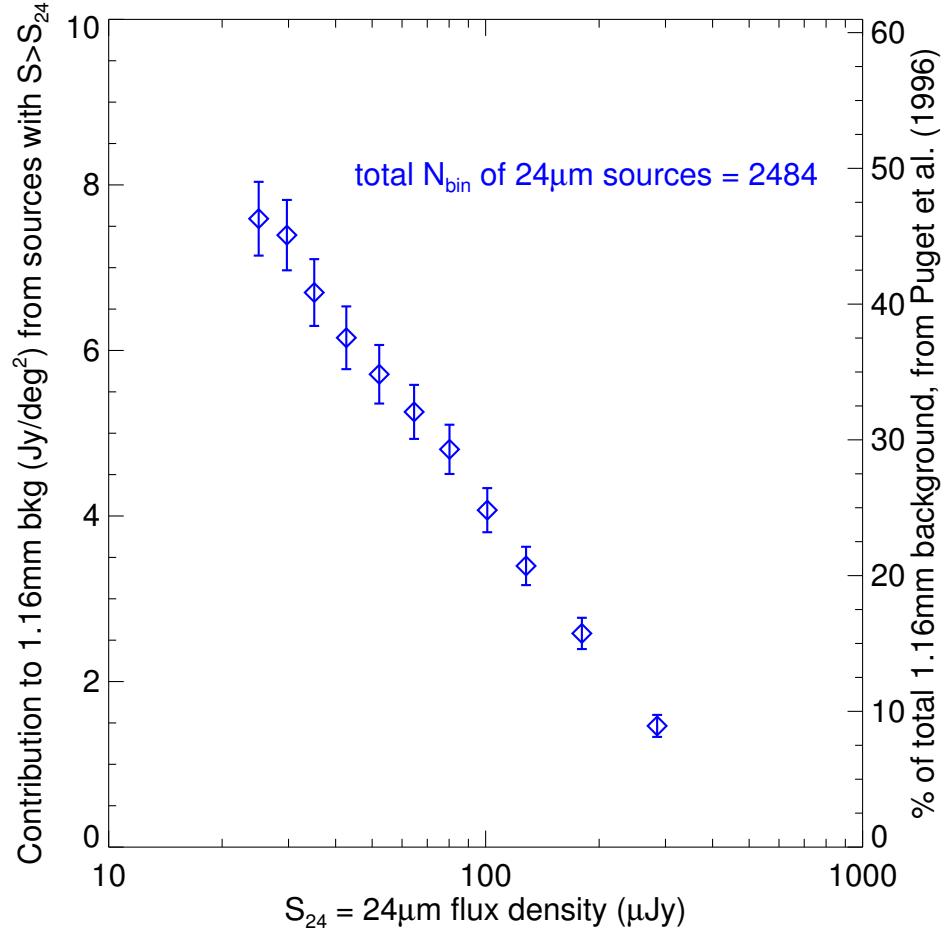


Figure 2.8 Contribution to the 1.16 mm background from $24\mu\text{m}$ sources with flux densities $> S_{24}$.

must be subtracted from the observed background. At 1.16 mm the published estimates for the total CIB are 16.4 Jy deg^{-2} (Puget et al. 1996) and 22.0 Jy deg^{-2} (Fixsen et al. 1998) (Table 2.3).

The left panel in Fig. 2.9 shows the resolved 1.16 mm background decomposed into redshift bins. Photometric redshift errors for individual $24\mu\text{m}$ sources should be negligible in bins of this size. The highest redshift bin is for all sources with $z > 1.33$, but we plot it out to $z = 3$ for clarity. We assume that any $24\mu\text{m}$ sources that fail to match to

Table 2.3. The total background at 4 wavelengths

Wavelength	Puget 96	Fixsen 98	Adopted
mm	Jy deg ⁻²	Jy deg ⁻²	Jy deg ⁻²
0.85	31	44 ⁺⁵ ₋₈	40 ± 9
1.1	18.3	24.8 ^{+1.7} _{-4.0}	...
1.16	16.4	22.0 ^{+1.4} _{-3.4}	19.9 ± 3.5
1.2	15.4	20.4 ^{+1.1} _{-3.0}	...

unique sources with redshift estimates (either spectroscopic or photometric) lie at $z > 1.3$, and we add their contribution to the highest redshift bin.

The 1.16 mm background is not fully resolved by $24\mu\text{m}$ sources with $S_{24} > 25\mu\text{Jy}$. Most of the resolved portion comes from galaxies at high redshift ($z > 1.3$). We repeat our stacking analysis on the cleaned $850\mu\text{m}$ map to investigate the differences in the resolved portions of the background at $850\mu\text{m}$ and 1.16 mm.

We use the same redshift bins as in the 1.16 mm analysis (the right panel in Fig. 2.9). At $850\mu\text{m}$ the values for the total background are 31 Jy deg⁻² (Puget et al. 1996) and 44 Jy deg⁻² (Fixsen et al. 1998) (Table 2.3). The contribution from the secure $850\mu\text{m}$ detections is added to the contribution derived from stacking the $24\mu\text{m}$ sources on the cleaned map. All secure $850\mu\text{m}$ detections have $24\mu\text{m}$ counterparts and we assume for simplicity that the detections lie at $z > 1.3$. This assumption is reasonable since only 4 of the 33 detections appear to lie at $z < 1.3$ (Pope et al. 2006) and these 4 account for < 5 percent of the contribution from the detections.

Our analysis does not definitively provide the redshift origins of the total $850\mu\text{m}$

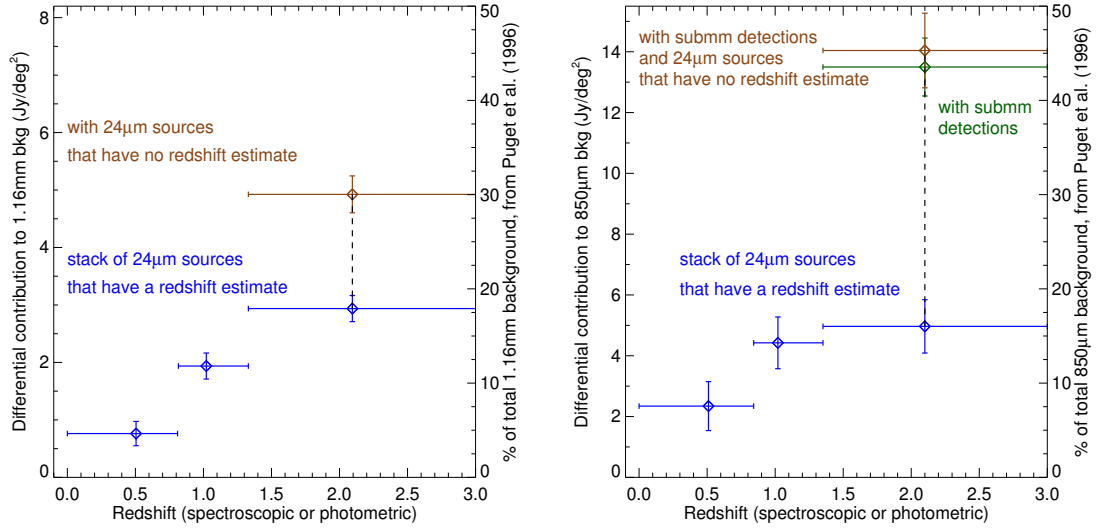


Figure 2.9 *Left panel:* The differential redshift distribution of the resolved 1.16 mm background from 24 μm sources. The diamonds are plotted at the average redshifts of the bins. The brown diamond contains the contributions from the 24 μm sources with $z > 1.3$ and the 24 μm sources without a redshift estimate. *Right panel:* The differential redshift distribution of the resolved 850 μm background from 24 μm sources. We use the same redshift bins as in the left panel. The y-axes in both panels show the levels at which the backgrounds are 50 percent resolved. Most of the resolved background at the two wavelengths comes from galaxies at $z > 1.3$.

background since it is not completely resolved by 24 μm sources. The results suggest that a large fraction of the resolved 850 μm background originates in galaxies at $z > 1.3$. Wang et al. (2006) perform a stacking analysis and conclude that more than half of the background at 850 μm comes from galaxies at low redshifts ($z < 1.5$). Our method differs from that of Wang et al. (2006); they stack a near infrared ($H + 3.6 \mu\text{m}$) sample on the full map with the 850 μm detections.

We show that the background at 850 μm and 1.16 mm is only partially resolved. Can we provide any constraints on the redshifts of the galaxies that contribute to the remainder

of the 1.16 mm background?

There are two often used estimates for the total background at these two wavelengths. We adopt the average of the range allowed by the two estimates: $19.9 \pm 3.5 \text{ Jy deg}^{-2}$ at 1.16 mm, and $40 \pm 9 \text{ Jy deg}^{-2}$ at $850 \mu\text{m}$ (Table 2.3). If we assume that the galaxies responsible for the unresolved $850 \mu\text{m}$ background contribute in a way to maintain the redshift distribution of the contribution from the galaxies responsible for the resolved background, the final decomposition of the $850 \mu\text{m}$ background is $[z \sim 0.4, z \sim 1, z > 1.3] = [4.5 \pm 1.6 \text{ Jy deg}^{-2}, 8.5 \pm 1.6 \text{ Jy deg}^{-2}, 27 \pm 2 \text{ Jy deg}^{-2}]$. The uncertainties maintain the SNR of the redshift bins of the resolved background. We also assume that the ratios of the resolved $850 \mu\text{m}$ to 1.16 mm background as a function of redshift (last column of Table 2.4) hold for the total $850 \mu\text{m}$ background; we thus convert each contribution to the $850 \mu\text{m}$ background into a contribution to the 1.16 mm background. The decomposition of the 1.16 mm background is $4.5/3.1 + 8.5/2.3 + 27/2.9 = 14.4 \pm 0.85 \text{ Jy deg}^{-2}$. The rest of the 1.16 mm background, which is $19.9 - 14.4 = 5.4 \pm 0.85 \text{ Jy deg}^{-2}$, presumably comes from galaxies at $z > 1.3$, where the observed submm to mm flux density ratio is lower than the values we use (see, for example, fig. 13 in Greve et al. 2004). The sum of all contributions from galaxies at $z > 1.3$ is $14.8 \pm 1.1 \text{ Jy deg}^{-2}$, or 74 ± 14 percent of the total 1.16 mm background. This likely scenario for the unresolved background is shown with filled bars in Fig. 2.10.

Table 2.4. Redshift distributions of the resolved $850\mu\text{m}$ and 1.16 mm background

z	$S_{\text{bin},1.16}$ mJy	$N_{\text{bin},1.16}$	percent w/spec- z	1.16 mm bkg Jy deg^{-2}	$S_{\text{bin},850}$ mJy	$N_{\text{bin},850}$	$850\mu\text{m}$ bkg Jy deg^{-2}	850/1.16
0 – 0.82	0.090 ± 0.025	576	75	0.76 ± 0.21	0.237 ± 0.081	304	2.34 ± 0.81	3.1 ± 1.4
0.82 – 1.33	0.199 ± 0.023	660	64	1.94 ± 0.23	0.402 ± 0.077	338	4.42 ± 0.85	2.3 ± 0.5
> 1.33	0.302 ± 0.023	660	26	2.94 ± 0.23	0.492 ± 0.087	310	4.97 ± 0.88	1.7 ± 0.3
with $850\mu\text{m}$ detections added to highest z bin								
> 1.33	...	660	...	2.94 ± 0.23	...	343	13.50 ± 0.95	4.6 ± 0.5
with ‘redshift unknown’ added to highest z bin								
> 1.33	...	1248	...	4.92 ± 0.32	...	538	14.04 ± 1.23	2.9 ± 0.3

Note. — Columns: $S_{\text{bin},1.16}$ is the stacked 1.16 mm flux density of $N_{\text{bin},1.16}$ sources; $S_{\text{bin},850}$ is the stacked $850\mu\text{m}$ flux density of $N_{\text{bin},850}$ sources. Column 4 is the percentage of the $N_{\text{bin},1.16}$ sources that have a redshift determined spectroscopically. Columns 5 and 8 are the resolved background in each bin. Column 9 is the resolved $850\mu\text{m}$ background divided by the resolved 1.16 mm background.

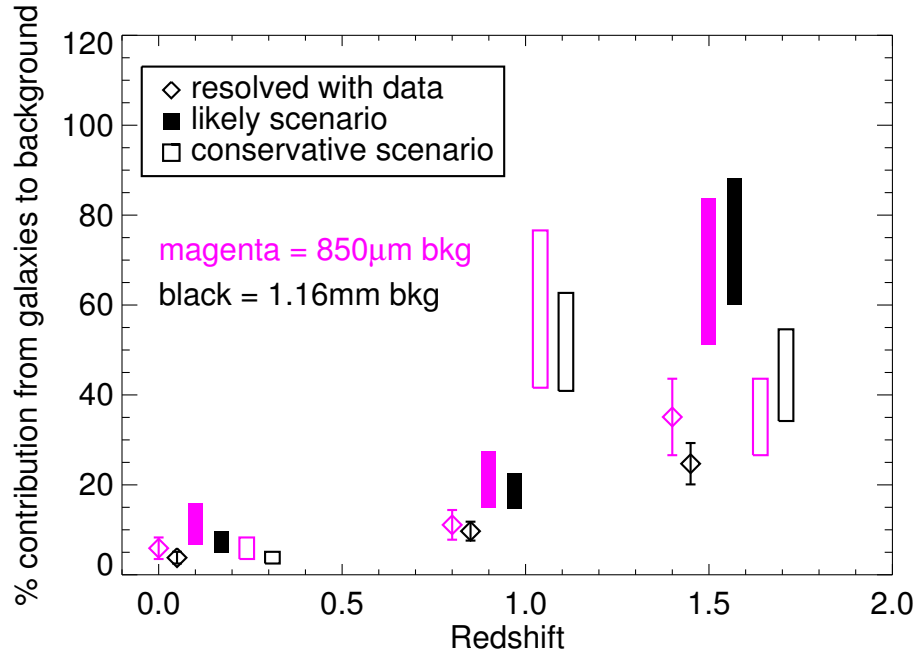


Figure 2.10 The redshift origins of the background at $850\mu\text{m}$ and 1.16 mm under various scenarios. The different plotting styles indicate different scenarios: all magenta points/bars are for the $850\mu\text{m}$ background while all black points/bars are for the 1.16 mm background. Points/bars are offset within the redshift bins for clarity. In what we deem the most likely scenario, 60–88 percent of the 1.16 mm background comes from galaxies at $z > 1.3$.

Although we cannot quantify the probability that the unresolved $850\mu\text{m}$ background is distributed as the resolved background, we are able to derive a lower limit to the amount of the total 1.16 mm background that comes from galaxies at $z > 1.3$. In a conservative scenario, all of the unresolved $850\mu\text{m}$ background comes from galaxies at $z < 1.3$. Assuming the ratio of 2.3 at $z \sim 1$ holds for the total background, an additional contribution of $40 - 2.3 - 4.4 - 14 = 19.3\text{ Jy deg}^{-2}$ at $850\mu\text{m}$ corresponds to an additional contribution of 8.4 Jy deg^{-2} at 1.16 mm . If the unresolved $850\mu\text{m}$ background is produced only by $z < 1.3$ galaxies, the contribution to the 1.16 mm background is $0.8 + 10.3 + 4.9 =$

$16 \pm 1.3 \text{ Jy deg}^{-2}$. The remaining $19.9 - 16 = 3.9 \pm 1.3$ of the 1.16 mm background presumably comes from galaxies at $z > 1.3$. At minimum, 44 ± 10 percent of the total 1.16 mm background comes from galaxies at $z > 1.3$. This conservative scenario is illustrated with unfilled bars in Fig. 2.10.

An alternate explanation to both scenarios is that all the unresolved background comes from a population of low-redshift galaxies with very cold dust and no warm dust (that is, a population of galaxies with a disproportionate number of large dust grains relative to small dust grains). Our decomposition of the (sub)mm background depends on selecting dusty galaxies at $24 \mu\text{m}$. The selection could miss galaxies with little or no warm dust. Galaxies with an excess of cold dust need dust temperatures in the realm of $\sim 10 \text{ K}$ at $z \sim 1$, and lower temperatures at lower redshifts, to account for the ratio of unresolved $850 \mu\text{m}$ to 1.1 mm background. Large numbers of galaxies are unlikely to have these extreme dust temperatures.

In this chapter, we use observational constraints on the fraction of the (sub)mm background that is resolved to hypothesize that 60–88 percent of the 1.16 mm background comes from high-redshift galaxies. In order to resolve the total 1.16 mm background and provide direct constraints on the redshifts of the galaxies, we need improvements in the mm map. Future single-dish (sub)mm telescopes, such as the Large Millimeter Telescope, will provide maps in which the bulk of the galaxies that contribute to the cosmic millimeter background are individually detected. Improvements in stacking catalogs and methods are unlikely to fully resolve the background. Since 2011, when this work was published, another group has employed a stacking analysis at 1.1 mm. Fig. 2.11 compares our results with those of Viero et al. (2013). The two redshift distributions are roughly the same. (Their bins are fixed in redshift while ours are fixed in number of sources.) Models presented in Chary & Pope (2010) predict that 60 percent of the 1.2 mm background comes from galaxies with 1.2 mm flux densities larger than 0.06 mJy —30 times deeper

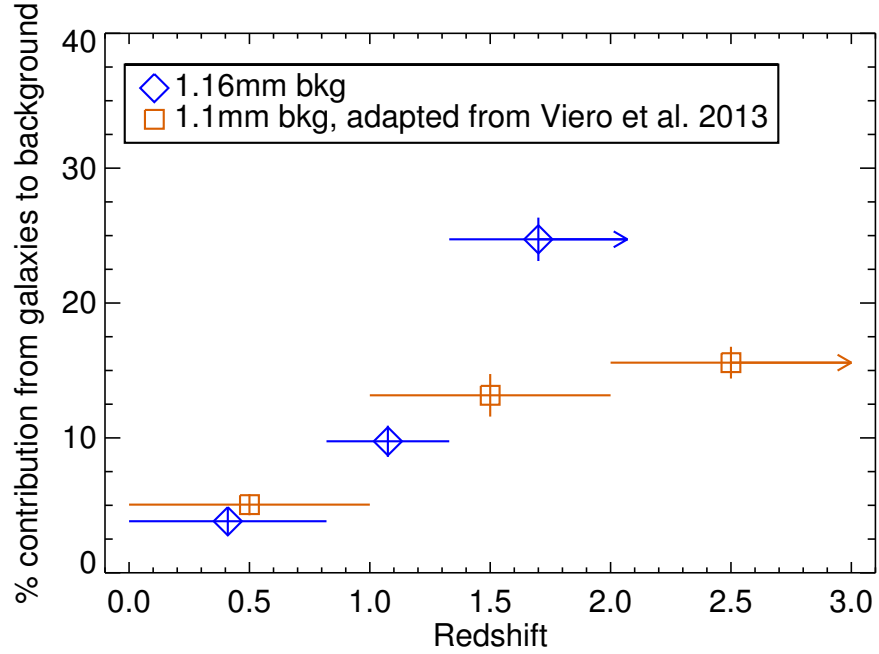


Figure 2.11 Redshift distributions of the resolved CIB at ~ 1.1 mm. Our results are the blue diamonds. The results of Viero et al. (2013) are the orange squares. (Their $2 < z < 3$ and $3 < z < 4$ bins have been combined.) The two distributions are roughly the same.

than the combined map.

2.5 Summary

1. We create a deep ($\sigma \sim 0.5$ mJy) 1.16 mm map by averaging the AzTEC 1.1 mm and MAMBO 1.2 mm maps in the GOODS-N region. We verify the properties of this map by examining both the deboosted flux densities of the 41 secure detections and the stacked flux density of $24\mu\text{m}$ sources. Of the 41 secure detections, 13 are new.
2. We test the effects of angular clustering of $24\mu\text{m}$ sources on the stacked (sub)mm flux density. While clustering does not seem to lead to a significant overestimate of the stacked 1.16 mm flux density, it may be responsible for part of the overestimate

of the stacked $850\mu\text{m}$ flux density.

3. $24\mu\text{m}$ sources resolve 7.6 Jy deg^{-2} (31–45 percent) of the 1.16 mm background. 3 Jy deg^{-2} comes from galaxies at $z > 1.3$. $24\mu\text{m}$ sources resolve 12.3 Jy deg^{-2} (23–39 percent) of the $850\mu\text{m}$ background, and the submillimeter detections contribute an additional 16–26 percent. 14 Jy deg^{-2} of the $850\mu\text{m}$ background comes from galaxies at $z > 1.3$.
4. Using the ratio of the resolved $850\mu\text{m}$ background to the resolved 1.16 mm background, we propose that 60–88 percent of the cosmic millimeter background comes from high-redshift ($z > 1.3$) galaxies. In the most conservative scenario, 34–55 percent of the 1.16 mm background comes from galaxies at $z > 1.3$.

CHAPTER 3

QUIDDITY OF DOGS

Decomposing the CIB provides constraints on dust emission from all galaxies at all redshifts. In chapter 2 we argue that most of the millimeter background comes from galaxies at $z > 1.3$. What process creates dust and what process destroys it? The pat answer is that stars and supernovae create dust; supernovae shocks destroy it. However, dust creation and destruction are very different in high-redshift galaxies because some have dust masses which models, based on low-redshift galaxies, cannot explain (Michałowski et al. 2010a,b; Rowlands et al. 2014). If we know the spatial distribution of dust in galaxies we can address our incomplete knowledge of how galaxies became dusty and how they will become dust-poor. Our results indicate that galaxies at $z \sim 2$ are prime targets for such studies.

Dusty galaxies at $z \sim 2$ span a wide range of relative brightness between rest-frame mid-infrared ($8\mu\text{m}$) and ultraviolet wavelengths. We attempt to determine the physical mechanism responsible for this diversity. Dust-obscured galaxies (DOGs), which have rest-frame mid-IR to UV flux density ratios $\gtrsim 1000$, might be abnormally bright in the mid-IR, perhaps due to prominent AGN emission, PAH emission, or both, or abnormally faint in the UV. We use far-infrared data from the GOODS-*Herschel* survey to show that most DOGs with $10^{12} L_{\odot} \lesssim L_{\text{IR}} \lesssim 10^{13} L_{\odot}$ are not abnormally bright in the mid-IR when compared to other dusty galaxies with similar IR ($8\text{--}1000\mu\text{m}$) luminosities. We observe a relation between the median IR to UV luminosity ratios and the median UV continuum power-law indices for these galaxies and we find that only 24% have specific star formation rates which indicate the dominance of compact star-forming regions. This circumstantial evidence supports the idea that the UV- and IR-emitting regions in these galaxies are spatially coincident, which implies a connection between the abnormal UV

faintness of DOGs and dust obscuration. We conclude that the range in rest-frame mid-IR to UV flux density ratios spanned by dusty galaxies at $z \sim 2$ is due to differing amounts of UV obscuration. Of galaxies with these IR luminosities, DOGs are the most obscured. We attribute this range of UV obscuration to either: (1) differences in the degree of alignment between the spatial distributions of dust and massive stars; or (2) differences in the total dust mass.

This chapter is adapted from Penner et al. (2012).

3.1 Motivation

At $z \sim 2$, a large fraction of all high mass stars form in dusty galaxies (Chapman et al. 2005; Magnelli et al. 2011). Most of the intrinsic UV emission from newly formed stars in these galaxies is obscured, or absorbed by dust grains that subsequently heat up and radiate at IR wavelengths. The IR luminosity resulting from this obscuration is usually much greater than the emergent UV luminosity. For galaxies in which the intrinsic UV emission from newly formed stars is less obscured, the IR luminosity is still greater than the emergent UV luminosity, but to a lesser degree (Reddy et al. 2012). The relation between the IR and emergent UV emission from a $z \sim 2$ galaxy depends on the interplay between star formation and dust obscuration.

One of the many ways to select dusty galaxies at $z \sim 2$, without redshift determinations from spectroscopy, is to use the ratio of observed 24 to $0.65 \mu\text{m}$ (R -band) flux densities (Dey et al. 2008; Fiore et al. 2008). Sources satisfying $S_{24}/S_{0.65} \gtrsim 1000$ have been termed “dust-obscured galaxies,” or DOGs; their redshift distribution is approximately a Gaussian that peaks at $z = 2$ with $\sigma_z = 0.5$ (Dey et al. 2008). In the redshift range $1.5 < z < 2.5$, $0.65 \mu\text{m}$ observations are sensitive to rest-frame UV emission from newly formed massive stars, and $24 \mu\text{m}$ observations are sensitive to mid-IR emission from hot dust and polycyclic aromatic hydrocarbons (PAHs). The DOG criterion is thus

unique in that it selects galaxies in a specific redshift range which exhibit extreme ratios between their rest-frame mid-IR and UV flux densities.

The IR luminosities of DOGs with $L_{\text{IR}} \gtrsim 10^{13} L_{\odot}$ are dominated by emission from active galactic nuclei (AGN; Dey et al. 2008; Bussmann et al. 2009b). The dominant sources of the IR luminosities of less luminous DOGs is a topic of debate. Fiore et al. (2008) and Treister et al. (2009) conclude that the IR luminosities of many DOGs with $10^{12} L_{\odot} \lesssim L_{\text{IR}} \lesssim 10^{13} L_{\odot}$ originate from AGN, while Pope et al. (2008) conclude that many such DOGs are powered by newly formed stars.

In this paper we pose the question, What makes a DOG a DOG? The primary goal of our study is determining why DOGs have an extreme ratio between their rest-frame mid-IR and UV flux densities when compared to other dusty galaxies. Unfortunately the simple and singular selection criterion cannot distinguish between a DOG that is:

- abnormally bright at rest-frame $8\mu\text{m}$ for its far-IR flux density, indicating its mid-IR luminosity may be dominated by AGN emission or abnormally strong emission from polycyclic aromatic hydrocarbons (PAHs);
- or abnormally faint in the rest-frame UV for its optical flux density, indicating that dust more completely obscures the newly formed stars in the galaxy.

We use *Herschel* (Pilbratt et al. 2010) data in the GOODS-N region (Elbaz et al. 2011) to show that, on average, DOGs with $10^{12} L_{\odot} \lesssim L_{\text{IR}} \lesssim 10^{13} L_{\odot}$ are not abnormally bright at $8\mu\text{m}$ but are more UV faint than other galaxies with similar IR luminosities. The ratio between rest-frame IR and UV flux densities is set by the amount of obscuration, which can vary with either: (1) the degree of alignment between the spatial distributions of dust and massive stars; or (2) the total dust mass.

3.2 Data

3.2.1 Measured quantities

Our study uses observations of the GOODS-N region, which is roughly $10 \text{ arcmin} \times 16.5 \text{ arcmin}$ in extent. We cull the sample of DOGs from a catalog of $24 \mu\text{m}$ sources produced for the *Spitzer*/MIPS survey of the GOODS-N region (P.I. M. Dickinson; Magnelli et al. 2011). A $24 \mu\text{m}$ source is defined as a $\geq 3\sigma$ flux density measurement from PSF fitting to *Spitzer*/IRAC $3.6 \mu\text{m}$ source priors. The catalog is 99% complete at $S_{24} > 50 \mu\text{Jy}$, and contains 1603 sources.

The $2.2 \mu\text{m}$ (K_s -band) image we use to identify counterparts for the $24 \mu\text{m}$ sources comes from observations using the Canada-France-Hawaii Telescope (CFHT). The data are presented in Wang et al. (2010); we use our own reductions (Lin et al. 2012). The $0.65 \mu\text{m}$ (R -band) Subaru image we use to define the DOG sample comes from Capak et al. (2004). The 5σ depth of the $2.2 \mu\text{m}$ image is $\sim 0.60 \mu\text{Jy}$; the 3σ depth of the $0.65 \mu\text{m}$ image is $\sim 0.05 \mu\text{Jy}$.

To extract flux densities, we follow a modified version of the procedure used by Pope et al. (2008). Using SExtractor (Bertin & Arnouts 1996), we place $3''$ diameter apertures at the positions of sources detected ($\geq 5\sigma$) in the $2.2 \mu\text{m}$ image. If the $2.2 \mu\text{m}$ flux density is detected with $\text{SNR} \geq 5\sigma$ but the $0.65 \mu\text{m}$ flux density is not detected with $\text{SNR} < 3\sigma$, we use a 3σ limit for the latter flux density.

We use the same procedure to extract flux densities at 0.45 , 0.55 , 0.80 , and $0.90 \mu\text{m}$ (the B -, V -, I -, and z -bands) from Subaru images (Capak et al. 2004). We use these flux densities to determine rest-frame UV continuum power-law indices. We use the 3.6 , 4.5 , 5.8 , and $8 \mu\text{m}$ flux densities already associated with the $24 \mu\text{m}$ sources to determine whether or not their spectral energy distributions (SEDs) at these wavelengths behave as power laws; these flux densities come from a catalog produced for the *Spitzer*/IRAC survey of the GOODS-N region and will be included in catalogs accompanying the GOODS-

Herschel public data release.

For the optical/near-IR photometry, we calculate aperture corrections, defined as the ratios of total flux density to flux density in a $3''$ diameter aperture for point sources (non-saturated stars). We take the SExtractor parameter FLUX_AUTO as the total flux density. The corrections are factors of 1.086, 1.225, 1.247, 1.057, 1.086, and 1.057 at 0.45, 0.55, 0.65, 0.80, 0.90, and $2.2\mu\text{m}$, respectively. To maintain the signal-to-noise ratios given by SExtractor, both the flux densities and their uncertainties are multiplied by these factors.

We associate each $24\mu\text{m}$ source with a $2.2\mu\text{m}$ source and its extracted optical flux densities if the $2.2\mu\text{m}$ source is a unique match within $0.76''$ of the position of the $3.6\mu\text{m}$ prior. The match radius is chosen by maximizing the number of unique matches while minimizing the number of multiple matches. Of the 1603 $24\mu\text{m}$ sources, 87 either do not have a $\geq 5\sigma$ $2.2\mu\text{m}$ counterpart within the match radius (85 of 87) or have multiple counterparts (2 of 87).

The far-IR flux densities come from a catalog produced for the GOODS-*Herschel* survey (Elbaz et al. 2011). We use only 100 and $160\mu\text{m}$ flux densities measured with PACS (Poglitsch et al. 2010) and $250\mu\text{m}$ flux densities measured with SPIRE (Griffin et al. 2010), to avoid the complications of measuring flux densities for $24\mu\text{m}$ sources in the 350 and $500\mu\text{m}$ SPIRE images, which are affected by severe source confusion. We consider a $\geq 3\sigma$ measurement at 100 or $160\mu\text{m}$ to be a detection; at $250\mu\text{m}$, we require a $\geq 5\sigma$ measurement.

We impose additional constraints on the $250\mu\text{m}$ flux densities (and 5σ limits), similar to those defining the “clean index” (Hwang et al. 2010; Elbaz et al. 2010, 2011). The $250\mu\text{m}$ flux densities of clean sources (and 5σ limits of clean non-detections) should not be affected by severe source confusion. We do not impose additional constraints on the 100 and $160\mu\text{m}$ flux densities because the $100\mu\text{m}$ images are not deep enough to be affected by source confusion and the $160\mu\text{m}$ images are only deep enough to be

moderately affected. The 3σ depths of the 100 and 160 μm images are $\sim 1100 \mu\text{Jy}$ and $\sim 2700 \mu\text{Jy}$, respectively; the 5σ depth of the 250 μm image is $\sim 5700 \mu\text{Jy}$.

We attempt to match each 24 μm source to a source with a spectroscopic redshift from the catalogs of Barger et al. (2008; which includes redshifts compiled from the literature) and D. Stern (private communication). We find spectroscopic redshifts for 910 (57%) of the 24 μm sources. If no coincident sources with spectroscopic redshifts are found, we resort to the photometric redshift source catalog of Pannella et al. (submitted) to find a source match. We exclude sources with photometric redshifts derived from ill-fitting templates (those with reduced $\chi^2 > 2$). For an additional 510 (32%) of the 24 μm sources we have photometric redshift estimates. There are no redshift estimates for 183 (11%) of the 24 μm sources, and these sources are excluded from our samples.

3.2.2 Samples

Using the multi-wavelength information and redshifts, we define 2 samples from the superset of all 24 μm sources with $S_{24} > 50 \mu\text{Jy}$:

- *DOG sample*: All 24 μm sources with 2.2 μm counterparts and $S_{24}/S_{0.65} > 986$ (Fig. 3.1). The 24 μm flux density of the faintest DOG is $53 \mu\text{Jy}$, justifying our $S_{24} > 50 \mu\text{Jy}$ cut for the control sample. The limiting quantity is the depth of the 0.65 μm image ($3\sigma = 0.05 \mu\text{Jy}$; Capak et al. 2004). The redshift distribution of our sample of DOGs is shown in Fig. 3.2, also motivating our $1.5 < z < 2.5$ cut for the control sample. Six (of 61; 10%) DOGs have spectroscopic redshifts. In the following analysis, we include only DOGs with $1.5 < z < 2.5$. Our conclusions do not change if we include DOGs without redshift estimates in the sample.
- *Control sample*: All $S_{24} > 50 \mu\text{Jy}$ 24 μm sources with 2.2 μm counterparts that are at $1.5 < z < 2.5$ and that do not satisfy the DOG selection criterion. Seventy four (of 268; 28%) control galaxies have spectroscopic redshifts.

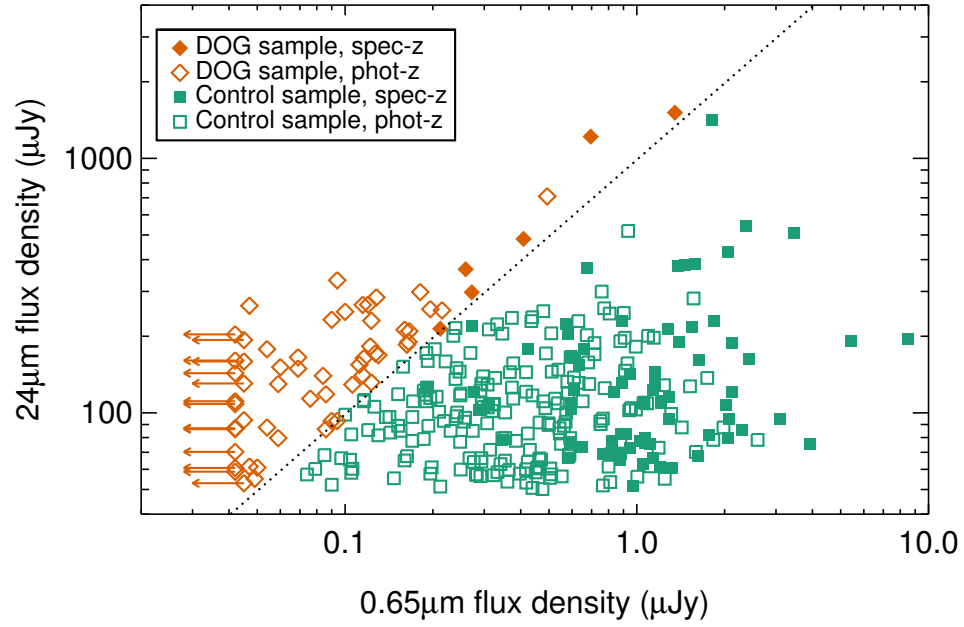


Figure 3.1 $24\mu\text{m}$ flux density vs. $0.65\mu\text{m}$ flux density for galaxies in the two samples. The DOG sample is defined by $S_{24}/S_{0.65} > 986$.

For each sample, Table 3.1 characterizes the subset of sources with flux densities detected at 0.65, 100, 160, and $250\mu\text{m}$. More than 70% of these galaxies are undetected in optical spectra (or are unobserved) because their observed-frame optical flux densities are so faint.

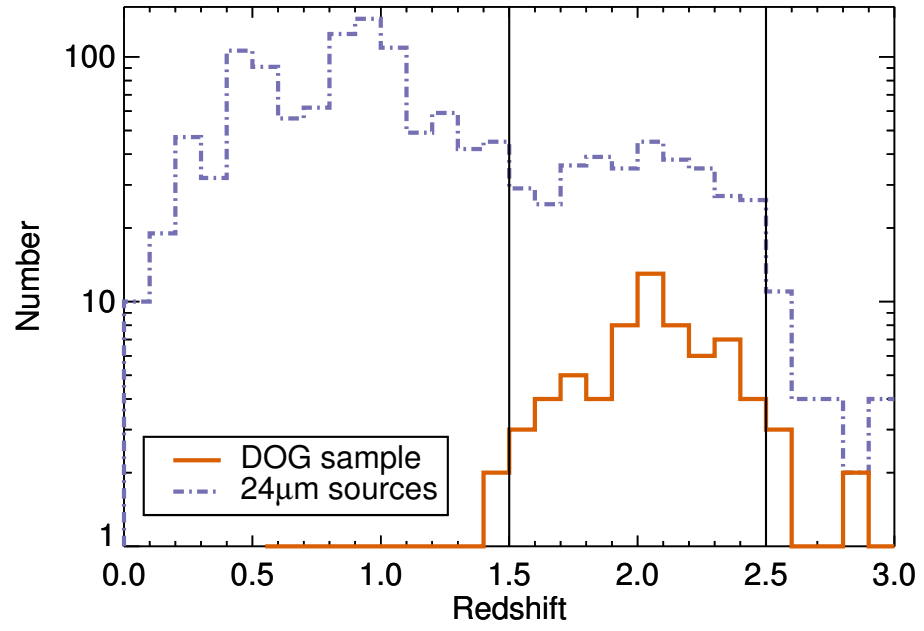


Figure 3.2 Redshift distributions for the DOG sample and all $24\mu\text{m}$ sources (before we impose redshift limits). For the analysis, we limit all samples to the redshift range $1.5 < z < 2.5$ (the area between the vertical lines).

Table 3.1. Basic properties of DOG and control samples

Sample	Number with $1.5 < z < 2.5$	Median z	Median S_{24} μJy	Number detected			
				$0.65\,\mu\text{m}$ $\geq 3\sigma$	$100\,\mu\text{m}$ $\geq 3\sigma$	$160\,\mu\text{m}$ $\geq 3\sigma$	$250\,\mu\text{m}$ $\geq 5\sigma$, clean
DOGs	61	2.1	161	47 (77%)	29 (48%)	24 (39%)	9 (15%)
Control	268	2.0	102	268 (100%)	81 (30%)	52 (19%)	15 (6%)

Note. — All sources have $\geq 5\sigma$ $2.2\,\mu\text{m}$ and $\geq 3\sigma$ $24\,\mu\text{m}$ flux density measurements. We also require $S_{24} > 50\,\mu\text{Jy}$.

Our sample contains DOGs with fainter $24\mu\text{m}$ emission than does the Dey et al. (2008) sample. Their sample is selected from the shallower *Spitzer*/MIPS survey of the Boötes region; their limit is $S_{24} > 300\mu\text{Jy}$. However, the GOODS-N region is much smaller than the Boötes region, so we have few DOGs with $S_{24} > 300\mu\text{Jy}$. Pope et al. (2008) also study a sample of DOGs in GOODS-N. The main differences between the Pope et al. (2008) sample and ours are that: (1) they limit their sample to $S_{24} > 100\mu\text{Jy}$; and (2) they estimate a redshift for each DOG using IRAC and MIPS photometry, whereas we match DOGs to sources in a near-IR/optical catalog with redshift estimates based on *UBVRIZJK*, 3.6 , and $4.5\mu\text{m}$ photometry.

The fractions of $24\mu\text{m}$ sources at $1.5 < z < 2.5$ that meet the DOG criterion increase with increasing $24\mu\text{m}$ flux density (Fig. 3.1). Of the sources with $S_{24} < 100\mu\text{Jy}$, 4% are DOGs. Of the sources with $S_{24} > 100\mu\text{Jy}$, 25% are DOGs. Riguccini et al. (2011) find similar fractions; they also find that of their sources with $S_{24} > 300\mu\text{Jy}$, 60% are DOGs.

3.2.3 Derived quantities

Several quantities are useful in analyzing the relation between IR and emergent UV emission from galaxies. In this section, we detail how we estimate the total IR and UV luminosities, UV continuum power-law indices, star formation rates, and stellar masses for the galaxies in our samples.

3.2.3.1 IR luminosities

We estimate a total IR luminosity ($8\text{--}1000\mu\text{m}$; L_{IR}) for each galaxy with detected emission at $100\mu\text{m}$. We redshift the Chary & Elbaz (2001) template spectral energy distributions (SEDs) to the distance of each galaxy, find the SED that most closely matches the observed $100\mu\text{m}$ flux density, and multiply the IR luminosity of that SED by the ratio between actual and predicted flux densities to get L_{IR} .

We prefer this approach over estimating the IR luminosity directly, by summing sev-

eral far-IR flux densities, because the latter procedure requires detected emission at 160 and 250 μm . The GOODS-*Herschel* image at 160 μm is moderately affected by blending due to source confusion while the image at 250 μm is so deep that blending is problematic. The drawback to our chosen approach is that all statements we make regarding IR luminosities assume that the low-redshift template SEDs accurately represent the SEDs of galaxies at $z \sim 2$. Elbaz et al. (2010) show that this assumption is valid when template matching is done to 100 μm flux densities.

3.2.3.2 UV continuum power-law indices and luminosities

For galaxies with UV emission from newly formed massive stars, the UV continuum can be approximated as a power law with an index β :

$$S_\lambda = C\lambda^\beta. \quad (3.1)$$

We use $\geq 3\sigma$ flux densities at 0.45, 0.55, 0.65, 0.80, and 0.90 μm (i.e., in the *B*-, *V*-, *R*-, *I*-, and *z*-bands) to fit for β and the constant factor C for each galaxy that has an estimate of L_{IR} . If only two flux densities have $\text{SNR} \geq 3\sigma$, we calculate β analytically. If only one flux density has $\text{SNR} \geq 3\sigma$, we use an upper limit for the 0.45 μm flux density to calculate a lower limit to β .

We estimate a UV luminosity λL_λ at rest-frame 0.16 μm for each galaxy using its redshift estimate and the power-law fit to the rest-frame UV flux densities.

3.2.3.3 Stellar masses and star formation rates

To estimate a stellar mass for each galaxy, we fit stellar population synthesis models to its *UBVRIzJK*, 3.6, and 4.5 μm flux densities (Drory et al. 2004; Pannella et al. 2009b). Full details are in §4.2 of Mullaney et al. (2012). We assume the stellar initial mass function in Salpeter (1955) from 0.1 to 100 M_\odot , as well as the dust attenuation formula in Calzetti et al. (2000).

We use the equation in Kennicutt (1998) to calculate a star formation rate (SFR), derived from the IR luminosity, for each galaxy with detected $100\mu\text{m}$ emission. We do not add the SFR derived from the emergent UV luminosity since it is negligible for all galaxies in the DOG and control samples (see §3.4). In using the Kennicutt (1998) equation, we assume that the observed $100\mu\text{m}$ emission is due to star formation and not AGN activity, and that the star formation episode lasts for $< 10^8$ years. Mullaney et al. (2012) find that the former assumption is valid for most AGN with detected X-ray emission at $z < 3$.

3.3 Results

Seventy six percent of the $z \sim 2$ galaxies with detected $100\mu\text{m}$ emission have $10^{12} L_{\odot} \lesssim L_{\text{IR}} \lesssim 10^{13} L_{\odot}$ (Fig. 3.3). The distributions of IR luminosities for the DOGs and the control galaxies are statistically indistinguishable ($p = 0.20$, from a K-S test, that the two samples are drawn from the same parent population).

Fig. 3.4 shows the stellar masses for DOGs and control galaxies with detected emission at $100\mu\text{m}$. The distributions are not strongly different ($p = 0.02$ from a K-S test), though some control galaxies have lower stellar masses than do the DOGs. 17 (of 72; 24%) control galaxies have stellar masses $M_* < 5 \times 10^{10} M_{\odot}$ while only 1 (of 25; 4%) DOG has a stellar mass below this threshold.

The infrared SEDs of most low-redshift dusty galaxies peak between rest-frame ~ 60 and $100\mu\text{m}$. The rest-frame $8\mu\text{m}$ luminosity is only a fraction of the total IR luminosity in these galaxies. To address whether or not DOGs are abnormally bright at rest-frame $8\mu\text{m}$ we require a comparison of the rest-frame far-IR and $8\mu\text{m}$ flux densities between DOGs and the control galaxies.

Fig. 3.5 shows that DOGs are statistically indistinguishable from the control galaxies when looking at the observed flux density ratio S_{100}/S_{24} ($p = 0.35$ from a K-S test).

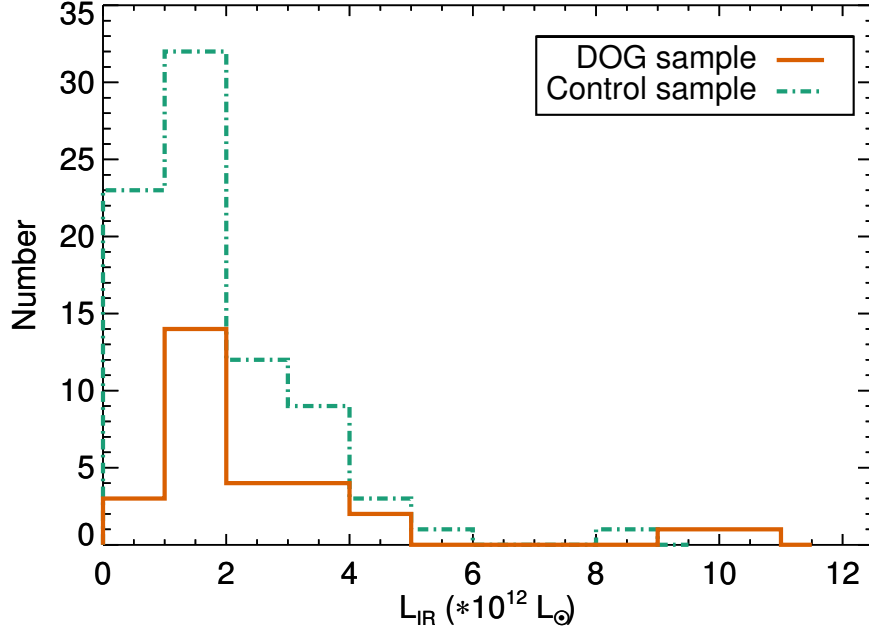


Figure 3.3 Distributions of IR luminosities (derived from best-fit templates) for galaxies with detected emission at $100\mu\text{m}$. The two distributions are statistically indistinguishable.

In this figure, we do not show the galaxies with limits for S_{100} . We perform the Gehan and logrank tests, which are conceptually similar to the two sample K-S test but also allow for the inclusion of galaxies with limits at $100\mu\text{m}$ in the two samples. We find no statistically significant difference between the DOGs and the control galaxies ($p > 0.70$, from both tests, that both samples are drawn from the same parent population). Our conclusions are the same using S_{160}/S_{24} (not shown; $p > 0.10$ from both tests). If DOGs were abnormally luminous at rest-frame $8\mu\text{m}$ for their far-IR luminosities, then we would expect them to have low values of observed S_{100}/S_{24} and S_{160}/S_{24} compared to those of the control galaxies; they do not. However, 100 and $160\mu\text{m}$ observations are sensitive to rest-frame 33 and $53\mu\text{m}$ emission from galaxies at $z = 2$. These rest-frame wavelengths are still short of the presumed wavelength of the peak of the infrared SED; the rest-frame

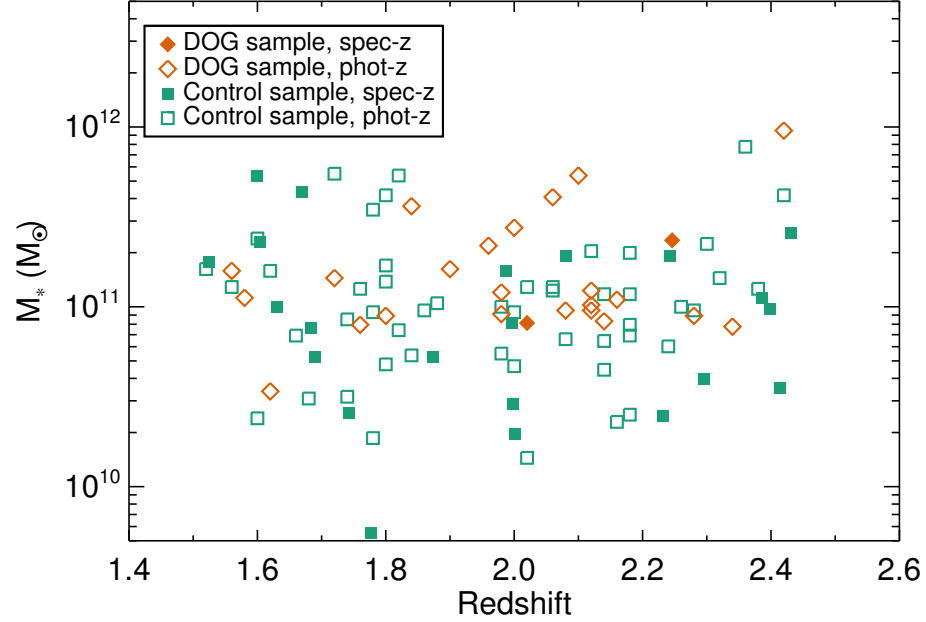


Figure 3.4 Stellar mass vs. redshift for galaxies with detected emission at $100\mu\text{m}$. The distribution of stellar masses for DOGs is not strongly different from that for control galaxies, though some control galaxies have lower stellar masses than do the DOGs. Twenty four percent of the control sample has $M_* < 5 \times 10^{10} M_\odot$, as opposed to 4% of the DOG sample.

luminosities are still only a fraction of the total IR luminosity in these galaxies.

$250\mu\text{m}$ observations are sensitive to rest-frame $83\mu\text{m}$ emission from galaxies at $z = 2$. This rest-frame wavelength is generally close to the wavelength of the peak of the IR SED. Fig. 3.6 shows that DOGs are statistically indistinguishable from the control galaxies when looking at the observed flux density ratio S_{250}/S_{24} . We reach the same conclusion when including galaxies with limits at $250\mu\text{m}$ in statistical tests ($p > 0.76$, from both a Gehan and logrank test, that both samples are drawn from the same parent population).

The DOG criterion does not select galaxies that are abnormally bright at rest-frame

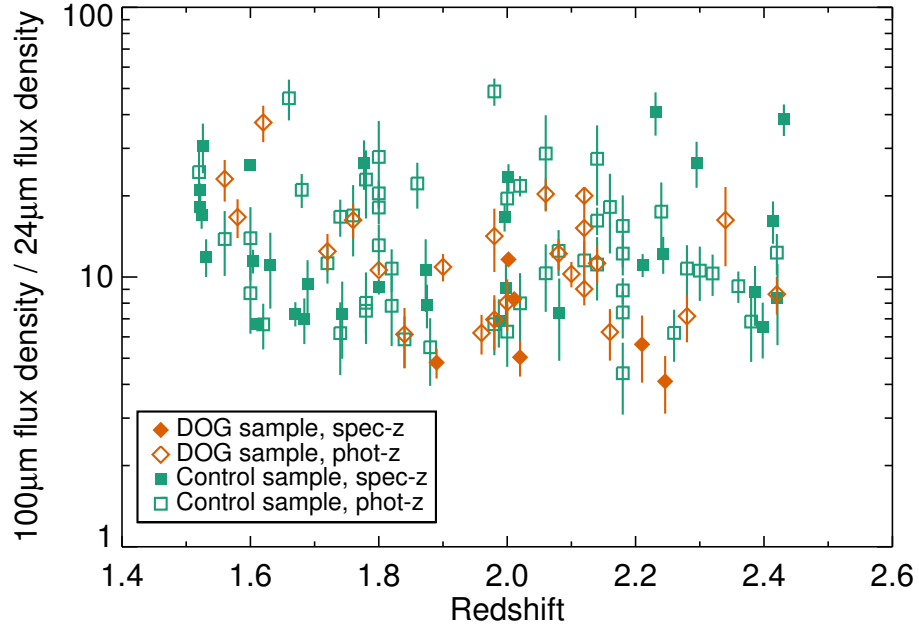


Figure 3.5 S_{100}/S_{24} vs. redshift for galaxies in the two samples. Galaxies with limits at $100\mu\text{m}$ are not shown in this figure but we do include them in our statistical tests. DOGs are statistically indistinguishable from the control galaxies in S_{100}/S_{24} .

$8\mu\text{m}$ for their far-IR flux densities. What makes a DOG a DOG must be that the galaxy’s rest-frame UV emission is suppressed compared to the UV emission from a control galaxy. Therefore we expect a clear separation between DOGs and control galaxies when looking at the ratios of rest-frame optical to UV flux densities. Indeed, Fig. 3.7 shows that 92% of DOGs have an observed $S_{2.2}/S_{0.65} > 20$, while 78% of control galaxies have $S_{2.2}/S_{0.65} \lesssim 20$. The Gehan and logrank tests report a statistical difference between the DOGs and control galaxies ($p < 0.0001$, from both tests, that both samples are drawn from the same parent population). Galaxies with $S_{2.2}/S_{0.65} \gtrsim 20$ are also known as “extremely red objects,” or EROs (Elston et al. 1988; Hu & Ridgway 1994; Graham & Dey 1996; McCarthy 2004). We note that even though a galaxy with detected $24\mu\text{m}$ emission

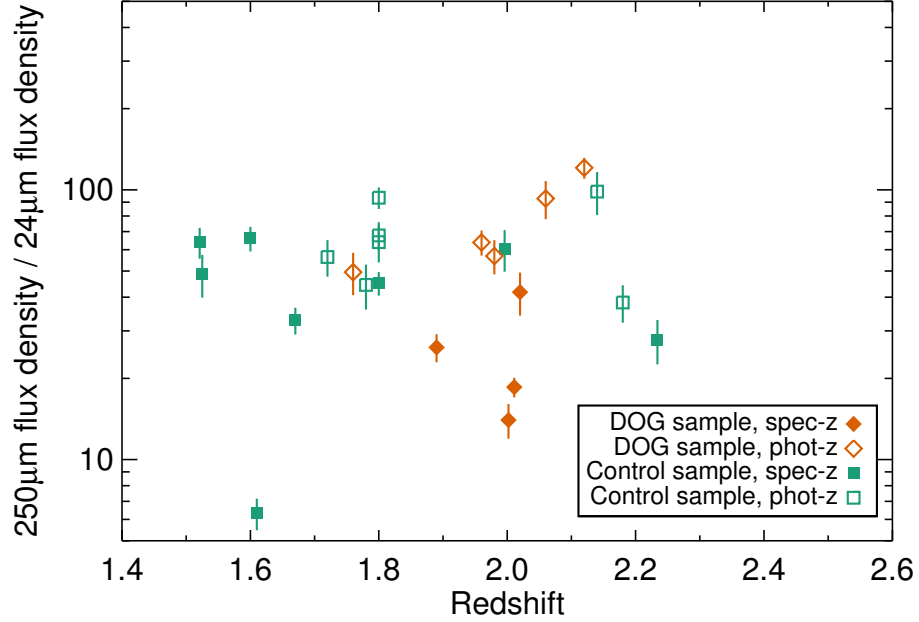


Figure 3.6 S_{250}/S_{24} vs. redshift for galaxies in the two samples. Galaxies with limits at $250\mu\text{m}$ are not shown in this figure but we do include them in our statistical tests. As in Fig. 3.5, DOGs span the same range of flux density ratios as do the control galaxies; this leads us to conclude that the DOG criterion does not select dusty galaxies that are abnormally bright at rest-frame $8\mu\text{m}$.

may meet the ERO criterion, it may not meet the DOG criterion (and vice versa, rarely).

The statistical difference between the DOGs and control galaxies for $S_{2.2}/S_{0.65}$, and the lack thereof for S_{100}/S_{24} , is robust against photometric redshift errors. We offset photometric redshifts for the superset of all galaxies with detected $24\mu\text{m}$ emission, assuming the offsets obey a Gaussian distribution with $\sigma_{\Delta z/(1+z)} = 0.1$. We then select new DOG and control samples. The differences in $S_{2.2}/S_{0.65}$ are always statistically significant, and the differences in S_{100}/S_{24} are very rarely statistically significant (from K-S tests).

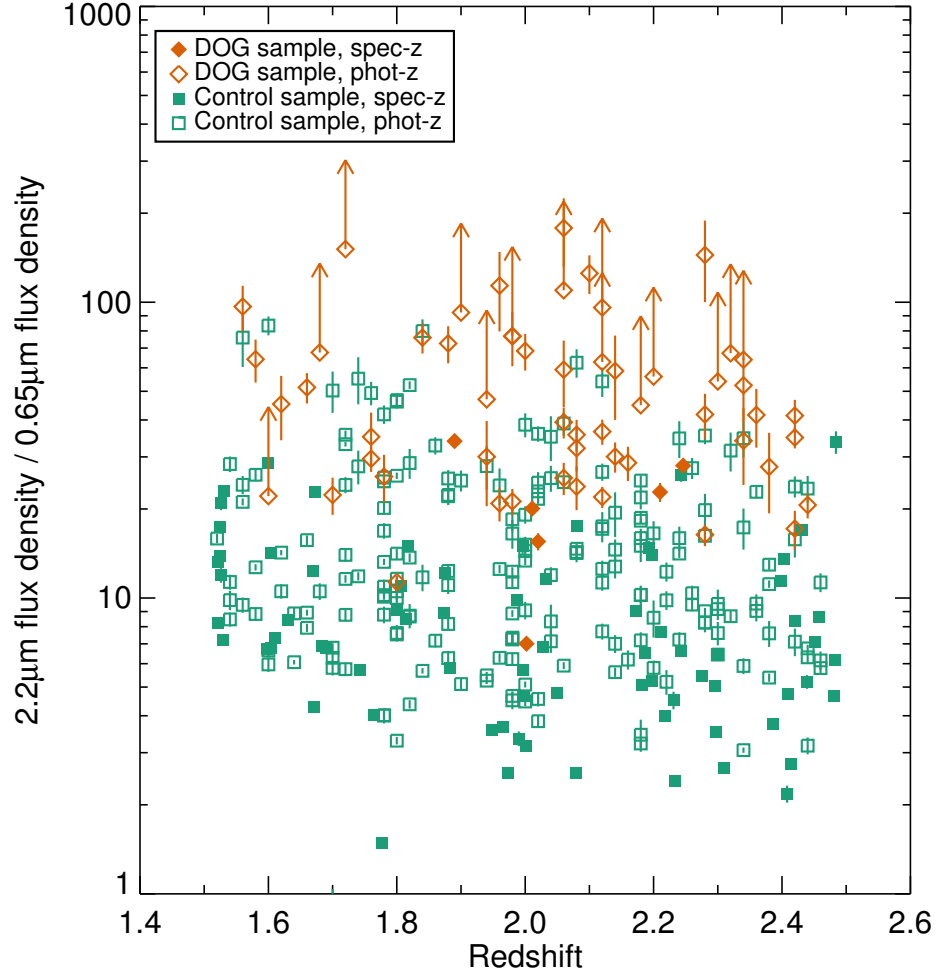


Figure 3.7 $S_{2.2}/S_{0.65}$ vs. redshift for galaxies in the two samples. A DOG is distinguishable from a random galaxy with detected $24\mu\text{m}$ emission because it is abnormally faint in the rest-frame UV.

3.4 Discussion

We have shown that the 100, 160, and 250 to $24\mu\text{m}$ flux density ratios for DOGs with moderate IR luminosities ($10^{12} L_{\odot} < L_{\text{IR}} < 10^{13} L_{\odot}$) are statistically indistinguishable from the flux density ratios for galaxies with detected $24\mu\text{m}$ emission that lie at similar redshifts, have similar IR luminosities, and do not meet the DOG selection criterion. Most

DOGs have higher 2.2 to $0.65\,\mu\text{m}$ flux density ratios than do the control galaxies. Thus it seems clear that DOGs occupy the tail of a distribution of UV obscuration in IR-luminous galaxies at $z \sim 2$.

We select a sample of DOGs using deep images of the GOODS-N region. These DOGs have lower IR luminosities than do DOGs selected using shallower images of wider regions. For example, the Dey et al. (2008) sample in the wide Boötes region contains many DOGs with $L_{\text{IR}} > 10^{13} L_{\odot}$. Our sample contains very few galaxies with $L_{\text{IR}} > 10^{13} L_{\odot}$ and our conclusions regarding obscuration may not apply to DOGs with such high luminosities. At low redshift, AGN emission dominates the IR luminosity for most galaxies with $L_{\text{IR}} > 10^{13} L_{\odot}$ (Tran et al. 2001). Dey et al. (2008) find that many DOGs at $z \sim 2$ with $L_{\text{IR}} > 10^{13} L_{\odot}$ have featureless SEDs from observed-frame 3.6 to $8\,\mu\text{m}$, indicating the presence of AGN-heated dust. Several studies find that, for these DOGs, the SEDs at rest-frame mid- and far-IR wavelengths are similar to those of low-redshift galaxies with IR luminosities dominated by AGN emission, such as Markarian 231 (Tyler et al. 2009; Bussmann et al. 2009b; Melbourne et al. 2012). Only 2 (of 59; 3%) DOGs, and 8 (of 253; 3%) control galaxies, have SEDs that increase (in νS_{ν}) from observed-frame 3.6 to $8\,\mu\text{m}$, and indeed both are among the DOGs with the highest L_{IR} (at 4.8×10^{12} and $9.5 \times 10^{12} L_{\odot}$). Two galaxies are not enough to allow us to rule out the possibility that DOGs with $L_{\text{IR}} > 10^{13} L_{\odot}$ differ in their 100 or 250 to $24\,\mu\text{m}$ flux density ratios from control galaxies with similar luminosities.

Most galaxies in our sample have $10^{12} L_{\odot} < L_{\text{IR}} < 10^{13} L_{\odot}$. Whether their IR luminosities are dominated by emission from AGN or newly formed stars is not clear. Fiore et al. (2008) and Treister et al. (2009) find that the average DOG in this L_{IR} range has an X-ray spectrum with a power-law index they interpret as indicative of heavily obscured AGN emission. An obscured AGN would presumably contribute to the IR luminosity as well. Pope et al. (2008) find the same X-ray index and also PAH emission

in the mid-infrared spectra of DOGs; they conclude that heavily obscured AGN emission cannot coexist with PAH emission. Pope et al. (2008) attribute the X-ray emission of the DOGs to X-ray binaries rather than AGN. In our sample, 5 (of 61; 8%) DOGs and 31 (of 268; 12%) control galaxies have detected X-ray emission (Alexander et al. 2003). For galaxies with $L_{\text{IR}} < 10^{13} L_{\odot}$ we do not find any evidence that AGN emission at rest-frame mid-IR wavelengths is more or less common in DOGs than in the control galaxies. The fractions of DOGs and control galaxies with increasing SEDs between observed-frame $3.6\mu\text{m}$ and $8\mu\text{m}$ are similar, as are the fractions with detected X-ray emission. No matter what powers their IR luminosities, DOGs in this L_{IR} range are abnormally UV faint and are probably the most obscured galaxies.

We have shown that the brightness of the emergent UV emission in $z \sim 2$ dusty galaxies can vary considerably from galaxy to galaxy, even though the emergent UV emission is only a fraction of the IR emission. In a dusty galaxy at either low or high redshift, most of the intrinsic UV emission from newly formed stars, AGN, or both is absorbed by dust grains, which emit at IR wavelengths. We now ask, Are the UV-emitting regions that we see from a DOG or a control galaxy spatially coincident with the IR-emitting regions? If yes, the variation in emergent UV emission is due to UV obscuration. If no, the emergent UV emission may come from stars in a “normal” galactic disk, whereas the newly formed stars ultimately responsible for the IR emission are completely obscured, perhaps in a compact, nuclear star-forming region. In this scenario, the variation in the rest-frame optical to UV flux density ratios might be due as much to differences in the stellar populations from galaxy to galaxy as to differences in obscuration (Charmandaris et al. 2004).

We cannot yet efficiently spatially resolve the IR-emitting regions for large samples of high-redshift dusty galaxies. Two pieces of circumstantial evidence support the statement that the UV- and IR-emitting regions in these dusty galaxies are spatially coincident: (1) a minority of DOGs and control galaxies deviate from the median specific SFR for galaxies

at $z \sim 2$; and (2) DOGs and control galaxies define a continuous relation between their median IR to UV luminosity ratios and median UV continuum power-law indices.

The specific star formation rate of a galaxy is the ratio of its SFR to its stellar mass. Most star-forming galaxies at the same redshift fall on a tight relation between SFR and stellar mass; this relation is referred to as the “main sequence” (Noeske et al. 2007; Elbaz et al. 2007; Daddi et al. 2007; Pannella et al. 2009a). Elbaz et al. (2011) find that SFR and stellar mass are directly proportional at all redshifts, and present the evolution of the median specific SFR for galaxies at $0 < z < 2.5$. Elbaz et al. (2011) also isolate the minority of galaxies with specific SFRs much higher than the median values (“starbursts”). Here, we define starbursts as galaxies with specific SFRs higher than 3 times the median value at their redshift. A minority of DOGs (5 of 25; 20%) and control galaxies (18 of 72; 25%) are starbursts (Fig. 3.8). Elbaz et al. (2011) find that individual low-redshift starbursts have compact UV-emitting regions; the correspondence between deviation from the median specific SFR and the compact size of the UV-emitting region also holds for the average $z \sim 2$ starburst. If this correspondence holds for individual $z \sim 2$ galaxies, few DOGs and control galaxies would have concentrated UV-emitting regions. These regions in the typical DOG or control galaxy would be more widely distributed, and it would be less plausible that the UV-emitting regions occupy parts of the galaxy not occupied by IR-emitting regions. That radio-emitting regions in high-redshift galaxies are widely distributed indirectly supports this idea (Rujopakarn et al. 2011).

For starburst galaxies at low redshift, Meurer et al. (1999; and more recently Overzier et al. 2011) find a relation between the ratio of IR to UV luminosities (denoted IRX) and the power-law index of the SED in the UV (denoted β). (Meurer et al. 1999 refer to low-redshift galaxies with bright UV-emitting regions as “starbursts.” The term does not necessarily refer to galaxies that deviate from the main sequence.) This relation is generally interpreted to mean that the IR emission originates as UV emission from newly

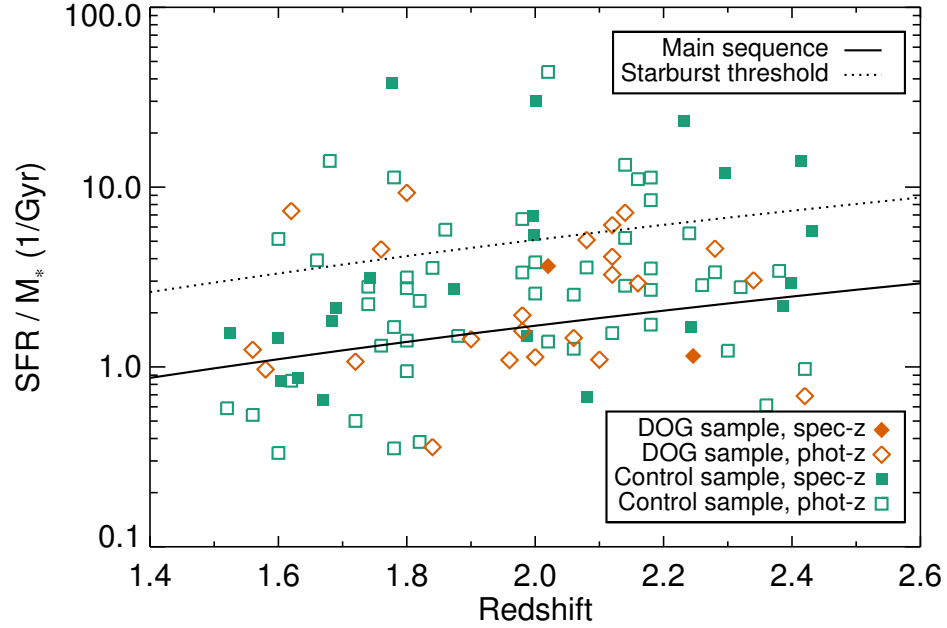


Figure 3.8 Specific star formation rate (SFR over stellar mass) vs. redshift for galaxies with detected $100\,\mu\text{m}$ emission. The solid line is the median specific SFR for star-forming galaxies, as a function of redshift (Elbaz et al. 2011). The dotted line is three times the median value, which we use as a threshold for identifying starbursts. 20% of DOGs and 25% of control galaxies are starbursts. DOGs deviate from the median specific SFR no more frequently than do the control galaxies.

formed stars, which is partially absorbed by dust. The dependence between the emergent UV emission, the dust emission in the IR, and β , in the low-redshift IRX- β relation is consistent with the dependence of dust absorption on β in the Calzetti et al. (1994, 2000) dust attenuation formula. In other words, we think that galaxies that lie on this relation have spatially coincident UV- and IR-emitting regions. Reddy et al. (2010, 2012) show that most Lyman break galaxies (LBGs) at $z \sim 2$ lie on the low-redshift IRX- β relation. However, both $z \sim 2$ LBGs and the low-redshift starbursts in Meurer et al. (1999) are much

less dusty than DOGs. Some subclasses of dusty galaxies deviate from the low-redshift relation, perhaps because their IR emission is unrelated to their emergent UV emission (Goldader et al. 2002; Chapman et al. 2005; Papovich et al. 2006; Bauer et al. 2011).

Fig. 3.9 shows the low-redshift IRX- β relation from Overzier et al. (2011) and the relevant quantities for the $z \sim 2$ dusty galaxies in our samples. Individual galaxies, in both the DOG and control samples, are found on either side of the relation. Because DOGs are so faint in the UV, it is difficult to precisely determine the power-law indices of their UV SEDs; the large uncertainties on β values preclude us from reaching firm conclusions about individual galaxies. The median β values for the DOG and control samples tend to lie to the left of the low-redshift IRX- β relation; DOGs do not appear to deviate more strongly from the relation than do control galaxies. These $z \sim 2$ dusty galaxies define their own IRX- β relation. As noted earlier, specific subpopulations of dusty galaxies deviate from the low-redshift relation, but the trend that we find between the averages for a broader $z \sim 2$ population has not been discussed. Because the median β value increases with increasing IRX, from the LBGs to the DOGs, the IR emission is not completely independent of the emergent UV emission in these galaxies. This reinforces our initial conclusion that $z \sim 2$ dusty galaxies populate a continuum of UV obscuration and that DOGs are simply the most heavily obscured galaxies.

DOGs in the luminosity range spanned by our sample are more obscured than the control galaxies for a reason unrelated to their far-IR luminosity because the L_{IR} distributions of the two samples are statistically indistinguishable. In galaxies with dust heated by UV emission from newly formed stars, the amount of obscuration affecting that UV emission can vary due to either: (1) differences in the degree of alignment between the spatial distributions of dust and newly formed massive stars; or (2) differences in the total dust mass.

Meurer et al. (1999) derive the low-redshift IRX- β relation by assuming a uniform

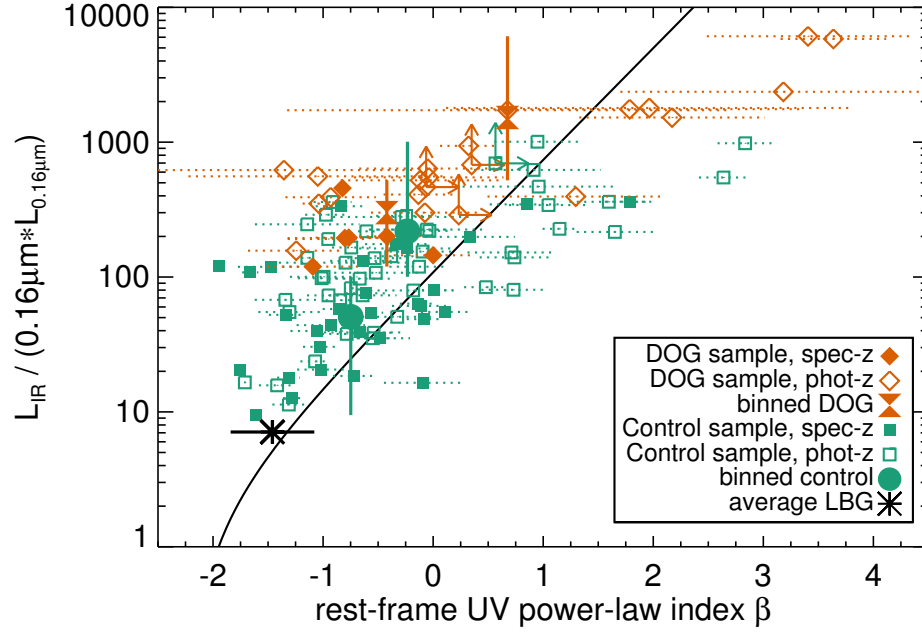


Figure 3.9 L_{IR} over $0.16\mu\text{m}$ luminosity (IRX) vs. UV continuum power-law index (β) for galaxies with detected $100\mu\text{m}$ emission. We only show errors on the UV power-law indices. Filled hourglasses and circles show the median β values, in bins of IRX; the vertical bars show the range of IRX over which the β values are binned. The “average LBG” black asterisk is from Reddy et al. (2012) and shows a mean and its dispersion. The solid line is the low-redshift IRX- β relation from Overzier et al. (2011).

screen of dust in the line of sight between us and the newly formed stars (see figure 8 in Calzetti et al. 1994 for an illustration). Gordon et al. (1997) show that this assumption can be recovered when the dust is instead distributed in clumps around star-forming regions. Thus DOGs might be more obscured than the control galaxies because DOGs have more dust clumps surrounding star-forming regions.

Variations in UV obscuration might also be caused by differences in the physical properties responsible for the shape of the submillimeter SED. For example, increases in the

mass of cold dust can result in greater UV obscuration. Increases in the cold dust mass can also result in increases in submillimeter emission. Since the submillimeter luminosity is usually a small fraction of the total IR luminosity, the increase in total IR luminosity due to a higher cold dust mass would not be easily measurable between 100 and 250 μm . We cannot fully test this hypothesis without submillimeter luminosities for galaxies in our samples. The sensitivities of current submillimeter facilities limit comparisons of the dust mass between DOGs and control galaxies to the most luminous ($L_{\text{IR}} > 10^{13} L_{\odot}$) galaxies (Bussmann et al. 2009b; Magdis et al. 2011).

For two galaxies with the same amount of UV obscuration, differences in the degree of alignment between dust and stars or differences in the grain size distributions alter the attenuation formula. Two galaxies with the same IRX can have different β values (Eq. 4.3). High-redshift dusty galaxies—both DOGs and the control galaxies—define their own IRX- β relation. At fixed IRX a high-redshift dusty galaxy may have lower β than a low-redshift dusty galaxy because the high-redshift galaxy follows a different attenuation formula and has unique dust properties.

New data are just now allowing us to discriminate between any hypotheses for the mechanisms responsible for differences in the degree of alignment between dust and stars, or for differences in the dust mass, between DOGs and the control galaxies. For instance, two plausible hypotheses are that: (1) galaxy inclination might be responsible for the patchiness of dust in the line-of-sight; and (2) many DOGs are merging galaxies, and some aspect of the merging process creates differences in the degree of alignment. To falsify either we require high resolution rest-frame optical images; the Cosmic Assembly Near-infrared Deep Extragalactic Legacy Survey (CANDELS) has obtained such images using *HST*/WFC3 (Grogin et al. 2011). Kartaltepe et al. (2012) and Schawinski et al. (2012) examine rest-frame optical images of DOGs in GOODS-S and conclude that most are undisturbed disk galaxies. Furthermore, Narayanan et al. (2010) simulate isolated

galaxies that meet the DOG selection criterion, so DOGs are not necessarily merging galaxies on the basis of their extreme rest-frame mid-IR to UV flux density ratios.

Finally, UV obscuration is affected by the prominence of the “dust bump” at rest-frame $0.2175\mu\text{m}$ in a galaxy’s attenuation curve. At $z \sim 2$, rest-frame $0.2175\mu\text{m}$ is redshifted into the R -band filter. The presence of this feature in the attenuation curves of high-redshift galaxies has been controversial; the bump is found, though, in the attenuation curves for several samples of galaxies at $z > 1$ (Noll et al. 2009; Buat et al. 2011, 2012). However, doubling the amplitude of the average bump leads to a reduction in the $0.65\mu\text{m}$ flux density by a factor of 1.3. This is not large enough to explain the spread of $S_{2.2}/S_{0.65}$ in Fig. 3.7.

3.5 Summary

1. We cull a sample of dust-obscured galaxies (DOGs), or galaxies with $S_{24}/S_{0.65} > 986$ that are at $1.5 < z < 2.5$, in the GOODS-N region. We use deep GOODS-*Herschel* data to compare the emission from DOGs with that from other $z \sim 2$ galaxies with detected $24\mu\text{m}$ emission.
2. The DOGs in our sample span $10^{12} L_{\odot} \lesssim L_{\text{IR}} \lesssim 10^{13} L_{\odot}$. DOGs and control galaxies with detected $100\mu\text{m}$ emission have similar distributions of IR luminosities and stellar masses.
3. We compare the rest-frame far-IR and optical flux densities of DOGs with those of the control galaxies. DOGs have extreme ratios of $S_{24}/S_{0.65}$ not because they are abnormally bright at rest-frame $8\mu\text{m}$ for their far-IR flux densities but because they are abnormally faint in the rest-frame UV.
4. DOGs and the control galaxies scatter around the median specific SFR established by $z \sim 2$ galaxies falling on the “main sequence;” 20% of DOGs have specific SFRs

greater than 3 times the median value and thus are starbursts. If UV-emitting regions in high-redshift starbursts are distributed as they are in low-redshift starbursts, few DOGs have compact UV-emitting regions.

5. For both the DOG and control samples, the median rest-frame UV continuum power-law index (β) at a given IR to UV luminosity ratio (IRX) is lower than the index predicted by the low-redshift IRX- β relation. DOGs do not appear to deviate more from this relation than do the control galaxies. Over more than a factor of 100 in IRX, the median β value for these galaxies systematically increases with increasing IRX.
6. These pieces of evidence suggest that, for most of these galaxies, the UV- and IR-emitting regions are spatially coincident. Thus the range in rest-frame mid-IR to UV flux density ratios spanned by dusty galaxies at $z \sim 2$ is due to differing amounts of UV obscuration. DOGs are the most heavily obscured galaxies.
7. Differences in the amount of obscuration between DOGs and other dusty galaxies at $z \sim 2$ can be due to: (1) differences in the degree of alignment between the spatial distributions of dust and massive stars; or (2) differences in the total dust mass.
8. Differences in the degree of alignment or differences in the grain size distributions can explain the discrepancy between high- and low-redshift IRX- β relations for dusty galaxies.

Our samples do not have many galaxies with $L_{\text{IR}} \gtrsim 10^{13} L_{\odot}$. In DOGs with these IR luminosities, where AGN emission may be the dominant source of dust heating, our conclusions about obscuration may not be valid.

Further information about the nature of obscuration in these galaxies can come from measurements that spatially resolve UV- and IR-emitting regions. *HST* can resolve the

rest-frame UV and optical emission from these galaxies (Bussmann et al. 2009a, 2011; Kartaltepe et al. 2012). ALMA will resolve the IR emission and allow us to measure the submillimeter luminosities that we need to determine cold dust mass. Studies using such data will clearly establish the degree to which the spatial distributions of dust and massive stars align.

A secondary, long-term, goal is to derive the attenuation formula for high-redshift galaxies and compare it to the formula for low-redshift galaxies. We require rest-frame UV and optical spectra and unambiguous attenuation measurements—including the ratio of $H\alpha$ to $H\beta$ line luminosities, which is the only measurement for zero attenuation.

CHAPTER 4

Is β WELL-DEFINED?

Our arguments in chapter 3—that UV- and IR-emitting regions in IR-luminous galaxies at $z \sim 2$ are spatially coincident and that the galaxies define their own IRX- β relation—depend on finicky determinations of the power-law indices of attenuated rest-frame UV continua. Our β values come from fitting Eq. 3.1 to 2 or more photometric flux densities, while the β values for the low-redshift IRX- β relation come from fitting to spectra. Calzetti et al. (1994) mask wavelength ranges where spectra are affected by absorption lines; we cannot do the same. There is also the question of whether our assumption that UV continua are power laws in wavelength is a good one. While the unattenuated UV continuum of a galaxy is a power law in λ , the Calzetti et al. (2000) attenuation formula is not a power law in λ ; deviations of the attenuated UV continuum from a power law complicate the interpretation of β . With these pitfalls, and others, in mind, we present an analysis of fitting β to simulated spectra and photometry.

4.1 Motivation

We eschew magnitudes of attenuation in favor of the escape fraction, which is the ratio of emergent to intrinsic luminosity. In relation to magnitudes of attenuation, A , the escape fraction, ϵ , is $10^{-A/2.5}$. We define ϵ_{UV} as the escape fraction at rest-frame $0.16 \mu\text{m}$, $\epsilon(0.16 \mu\text{m})$. The Calzetti et al. (2000) attenuation formula for $0.12 < \lambda < 0.63 \mu\text{m}$ becomes:

$$\epsilon(\lambda) = 10^{-0.4E_S(B-V)(2.659(-2.156+1.509/\lambda-0.198/\lambda^2+0.011/\lambda^3)+4.05)}, \quad (4.1)$$

with wavelength in μm . The escape fraction as a function of wavelength is roughly a power law for high values of ϵ_{UV} ; as ϵ_{UV} decreases, deviations of $\epsilon(\lambda)$ from a power law become apparent. A galaxy with a very low UV escape fraction, like a DOG, may not

have a well-defined β if it obeys this attenuation formula. If β is ill-defined, the value we find from fitting will depend on the rest-frame wavelengths of the photometry— β fit to 2 flux densities between 0.20 and 0.22 μm will differ from β fit to 2 flux densities between 0.13 and 0.15 μm . For photometry at fixed observed-frame wavelengths our β fits will vary with redshift. One test is to examine the difference in β between fits to a simulated spectrum and simulated photometry as a function of redshift.

If β is well-defined, DOGs and control galaxies may not obey the Calzetti et al. (2000) attenuation formula because they define their own IRX- β relation. Do different attenuation formulas alleviate or worsen the problem of fitting β at low escape fractions? The median relation in Fig. 3.9 constrains alternate attenuation formulas because the UV escape fraction is a function of IRX:

$$\kappa_{\text{UV}} = \left(\frac{L_{\text{IR}}}{1.68 \times 0.16 \times L_{0.16}} + 1 \right)^{-1}, \quad (4.2)$$

equivalent to $\kappa_{\text{UV}} = (\text{emergent UV SFR})/(\text{IR SFR} + \text{emergent UV SFR})$, and an attenuation formula relates the UV escape fraction to β :

$$\frac{\kappa_{\text{UV}}}{\kappa(\lambda)} = \left(\frac{0.16}{\lambda} \right)^{\beta - \beta_i}, \quad (4.3)$$

with wavelength in μm . β_i is the power-law index of the unattenuated spectrum. (If $\kappa(\lambda)$ is not a power law in λ , the relation between κ_{UV} and β depends on the wavelengths we use in Eq. 4.3.) We construct several attenuation formulas that predict different relations between the UV escape fraction and β and examine the effects on β fits. β fitting to spectra and photometry converges for reasonable attenuation formulas and at all relevant redshifts.

4.2 Simulated β values

We generate unattenuated spectra for 100 simulated galaxies each at $z = 1$, $z = 2$, and $z = 3$. Pforr et al. (2012) give the ranges of ages, metallicities, stellar masses, and star

formation rates of the galaxies. The spectra are attenuated using several attenuation formulas; for each formula, the escape fractions at $0.545\mu\text{m}$ decrease from 1 (unattenuated) to 0.01, in 26 steps. The (un)attenuated rest-frame UV spectra are then fit to Eq. 3.1. (There are 2600 β values for each formula at each redshift.) For fits to the spectra, we mask wavelength ranges affected by absorption lines. The resulting β values are the “true” values.

To examine the effects of redshift on β values, we generate 5 random numbers, δ_z , from a uniform distribution with $-0.5 < \delta_z < 0.5$ and offset the redshift of each galaxy by δ_z . (There are 13000 β values for each formula in each redshift range.) We again fit to the spectra to get true β values.

We generate flux densities from the (un)attenuated spectra for bands in the CANDELS GOODS-S catalog (Guo et al. 2013). We find flux densities in the catalog that are between 80 and 120% of each flux density for each simulated galaxy. We choose a random flux density from the list and generate a random number from a Gaussian distribution with σ equal to the flux density’s σ . We add the random number to the simulated galaxy’s flux density. If no flux densities in the catalog are between 80 and 120% of the simulated galaxy’s flux density, we do not add noise and do not estimate β or a limit. (The UV escape fraction is very low if $\tau(0.545\mu\text{m})$ is 0.01. Most of the 100 simulated galaxies with escape fractions at the low end have no match to galaxies in the catalog.)

We use all flux densities and uncertainties with rest-frame wavelengths between 0.125 and $0.263\mu\text{m}$ to fit for β and the constant factor C or for their limits (Eq. 3.1). Flux densities may be negative, which complicates our estimation logic. If a galaxy has only two flux densities in the wavelength range, the solution for β and C is analytic, so for a solution to exist the flux densities must be positive. If they both are, we do not make any cuts on their signal-to-noise ratio. If the only positive flux density, among multiple measurements, is $> 3\sigma$, we calculate a β limit using that flux density and a 3σ limit for

another in the rest-frame wavelength range. Whether the limit is an upper or lower one depends on whether the detected flux density's wavelength is lower or higher than the limit's wavelength. We do not estimate a β limit if the only positive flux density, among multiple measurements, is $< 3\sigma$. If more than two flux densities are positive, regardless of their SNR and whether the surplus measurements are negative or positive, we minimize χ^2 .

4.3 Results and discussion

We present and discuss results for three attenuation formulas.

4.3.1 The Calzetti attenuation formula

The top panel of Fig. 4.1 shows Eq. 3.1 with $\beta = \beta_i = -2.5$. For the purpose of display we choose $\beta_i = -2.5$ if the UV escape fraction is 1. After we apply attenuation according to the Calzetti et al. (2000; Eq. 4.1) formula, β does not equal β_i . A perfect power law, in the absence of attenuation, turns into a different function after attenuation, notably near $0.13\mu\text{m}$ for a UV escape fraction of 0.01.

The left panel of Fig. 4.1 shows that, for many escape fractions for the simulated galaxies at $z = 2$, β fit to the photometry recovers β fit to the spectrum; there are no systematic differences between the two β values. The dispersion of photometric β is high at high true β (low UV escape fractions). The right panel shows that many galaxies with high true β have highly uncertain photometric β ; the dispersion in this panel at high true β is no larger than it is at low true β . The combined effect of: (1) imperfect power laws, in the absence of attenuation, for UV continua of simulated galaxies; (2) the non-power law form of the Calzetti et al. (2000) attenuation formula; and (3) band availability in GOODS-S; is to maintain agreement, on average, between photometric and true β values. This result does not apply generally to the simulated galaxies, since it depends on which bands are observed, and it does not prove that real galaxies have UV continua that are

power laws in wavelength. We can only say that if real galaxies at $z = 2$ have spectra similar to spectra of the simulated galaxies at $z = 2$, our photometric and true β values would agree on average.

The non-power law behavior in the top panel of Fig. 4.1 is worrisome if flux densities are in fixed photometric bands and samples contain galaxies at different redshifts. If our flux densities are at rest-frame 0.125 and 0.15 μm for a $z = 2$ galaxy, they will be at rest-frame 0.15 and 0.18 μm for a $z = 1.5$ galaxy—which means that even though the spectra are the same, we may estimate different photometric β values. Fig. 4.2 shows that the redshift effect on β estimates is minor. At most redshifts the average difference in β values is less than 0.4, which is not enough to account for the difference between low- and high-redshift IRX- β relations in Fig. 3.9. The difference between relations is probably not due to the high-redshift relation being defined by low UV escape fractions for galaxies that obey the Calzetti et al. (2000) attenuation formula.

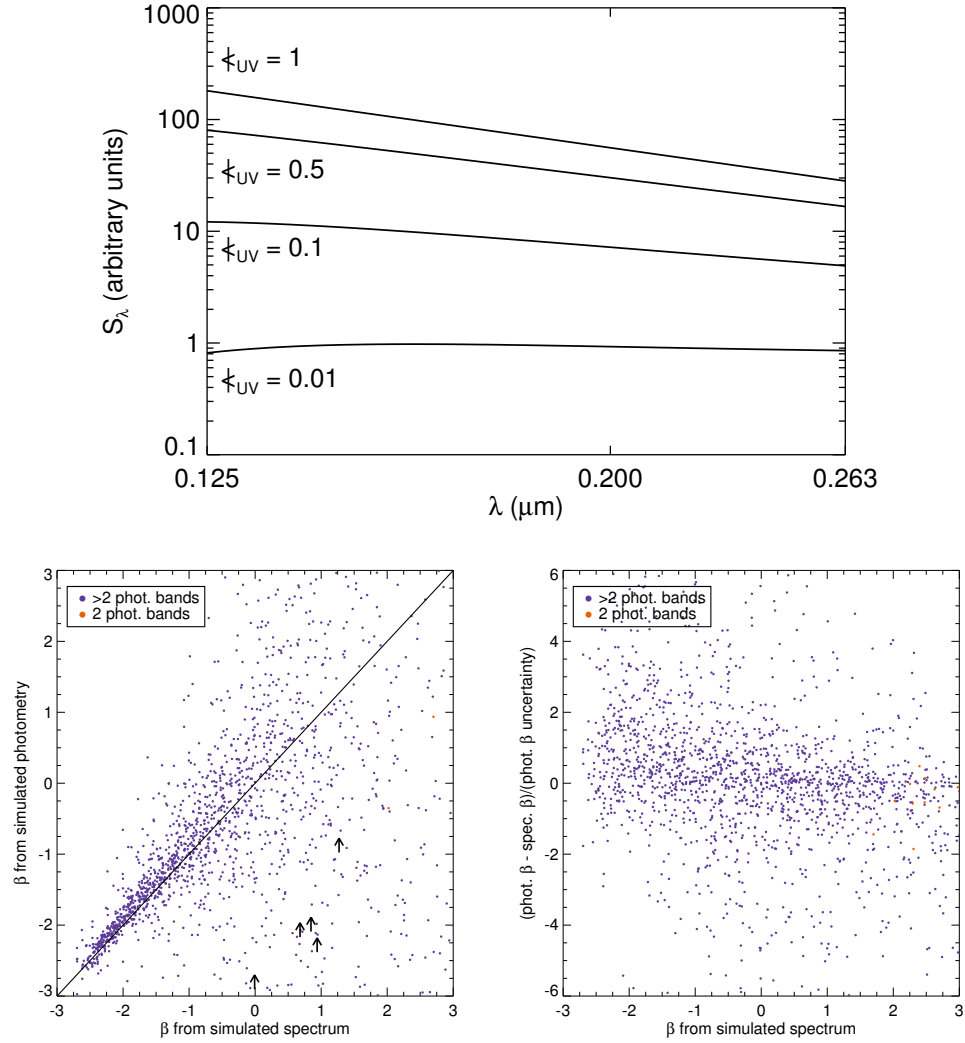


Figure 4.1 *Top*: Modifications to a perfect power law by the Calzetti et al. (2000) attenuation formula for UV escape fractions of 1 (unattenuated), 0.5, 0.1, and 0.01. At low escape fractions, the attenuated continua deviate from a power law. *Left*: β fit to photometry vs. β fit to spectra. On average the two β values agree. *Right*: Difference in β values divided by the photometric β uncertainty vs. true β . For most galaxies—even the ones with high true β (low UV escape fractions)—the photometric β is within $\pm 2\sigma$ of the true β . Agreement does not prove that the UV continua are power laws; it only proves that the fitting methods converge to the same β .

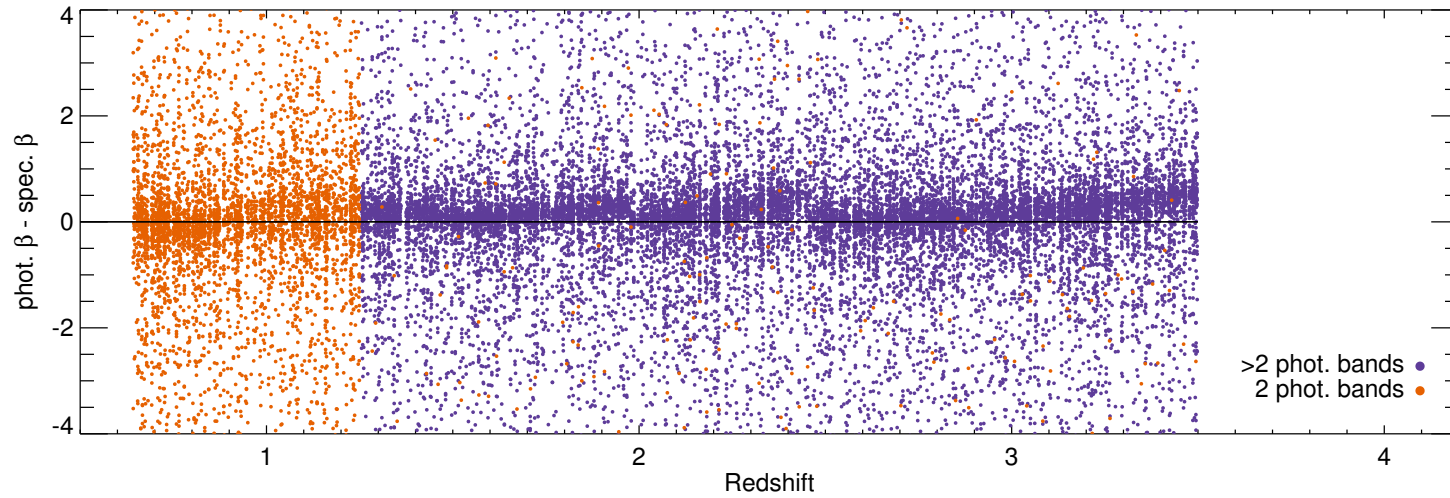


Figure 4.2 Difference in β values vs. redshift for attenuation according to the Calzetti et al. (2000) formula. At most redshifts the average difference in β values is less than 0.4. The difference between low- and high-redshift IRX- β relations (Fig. 3.9) is probably not due to the high-redshift relation being defined by low UV escape fractions for galaxies that obey the Calzetti et al. (2000) attenuation formula.

4.3.2 The attenuation formula for $z \sim 2$ dusty galaxies

This attenuation formula roughly predicts the high-redshift IRX- β relation:

$$\tau(\lambda) = 10^{-0.4E_S(B-V)(2.659(-2.156+1.509/\lambda-0.198/\lambda^2+0.010/\lambda^3)+4.05)}. \quad (4.4)$$

The coefficient for λ^{-3} is 0.010 instead of 0.011. We repeat our comparisons of β values in Figs. 4.3 and 4.4. At fixed and low UV escape fractions, the attenuation formula for $z \sim 2$ dusty galaxies modifies continua to be more like power laws than does the Calzetti et al. (2000) formula. However, our conclusions regarding β fits are the same as they are for the Calzetti et al. (2000) formula: there are no systematic differences in β values, either at fixed redshift or as a function of redshift.

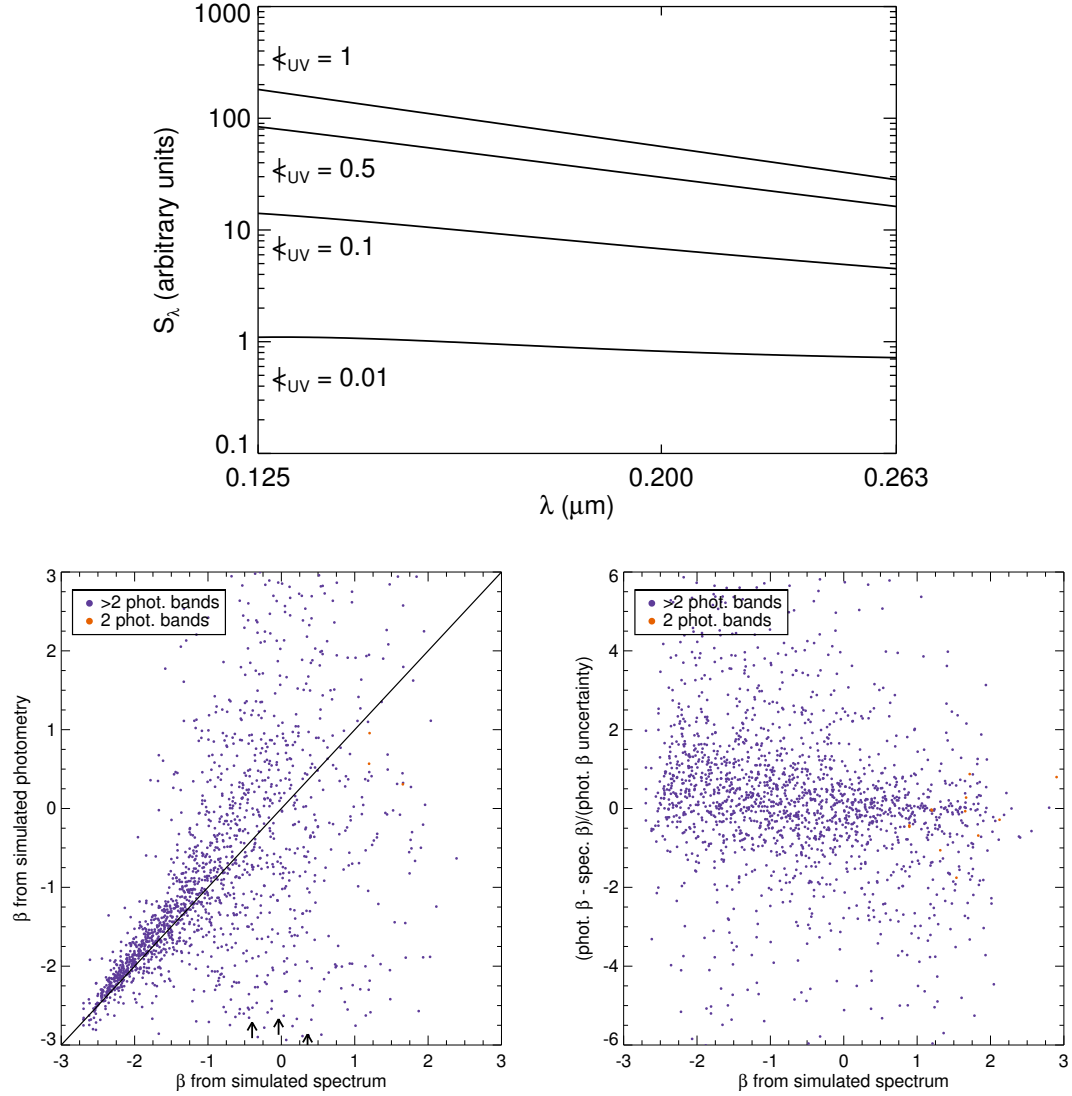


Figure 4.3 *Top*: Modifications to a perfect power law by the attenuation formula for $z \sim 2$ dusty galaxies (Eq. 4.4) for UV escape fractions of 1 (unattenuated), 0.5, 0.1, and 0.01. Compared to the Calzetti et al. (2000) attenuation formula, this formula results in continua that more closely resemble power laws. *Left*: β fit to photometry vs. β fit to spectra. On average the two β values agree. *Right*: Difference in β values divided by the photometric β uncertainty vs. true β . For most galaxies—even the ones with high true β (low UV escape fractions)—the photometric β is within $\pm 2\sigma$ of the true β .

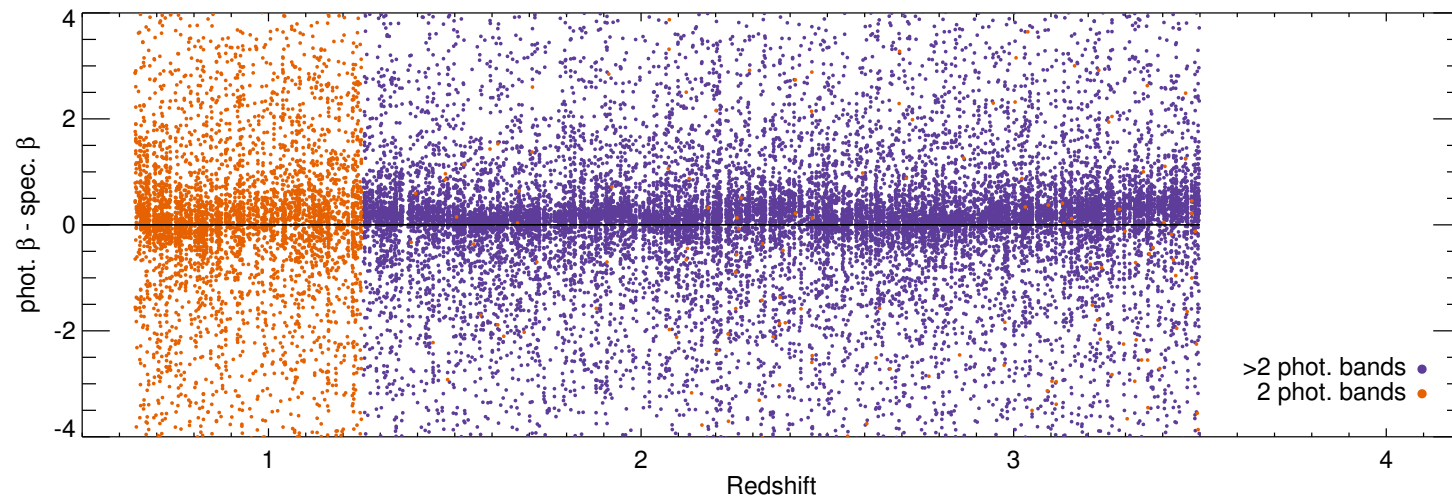


Figure 4.4 Difference in β values vs. redshift for attenuation according to the formula for $z \sim 2$ dusty galaxies (Eq. 4.4). At most redshifts the average difference in β values is less than 0.4.

4.3.3 The attenuation formula based on Murphy

We consider one final attenuation formula:

$$\kappa(\lambda) = 10^{-0.4E_S(B-V)(2.659(-2.166+1.509/\lambda-0.168/\lambda^2+0.015/\lambda^3)+4.05)}, \quad (4.5)$$

which roughly predicts the Murphy et al. (2011) IRX- β relation. They study IR-luminous sources at $0 < z < 2.8$. Their relation deviates from both relations in Fig. 3.9; they argue that some amount of UV luminosity from low-redshift galaxies can come from old stars, implying that the deviation may be observational and not physical. (Recall that the UV escape fraction comes from a ratio of star formation rates. The UV luminosity must come from newly formed massive stars.) However, this attenuation formula provides an interesting challenge to β fitting. At fixed and low UV escape fractions, this formula modifies continua to be less like power laws than does the Calzetti et al. (2000) formula (Fig. 4.5). Our β fits disagree at low UV escape fractions (Fig. 4.5) and systematic differences with redshift are apparent (Fig. 4.6). β is ill-defined if this is the true attenuation formula for high-redshift dusty galaxies, unless the galaxies have unattenuated spectra that are not power laws.

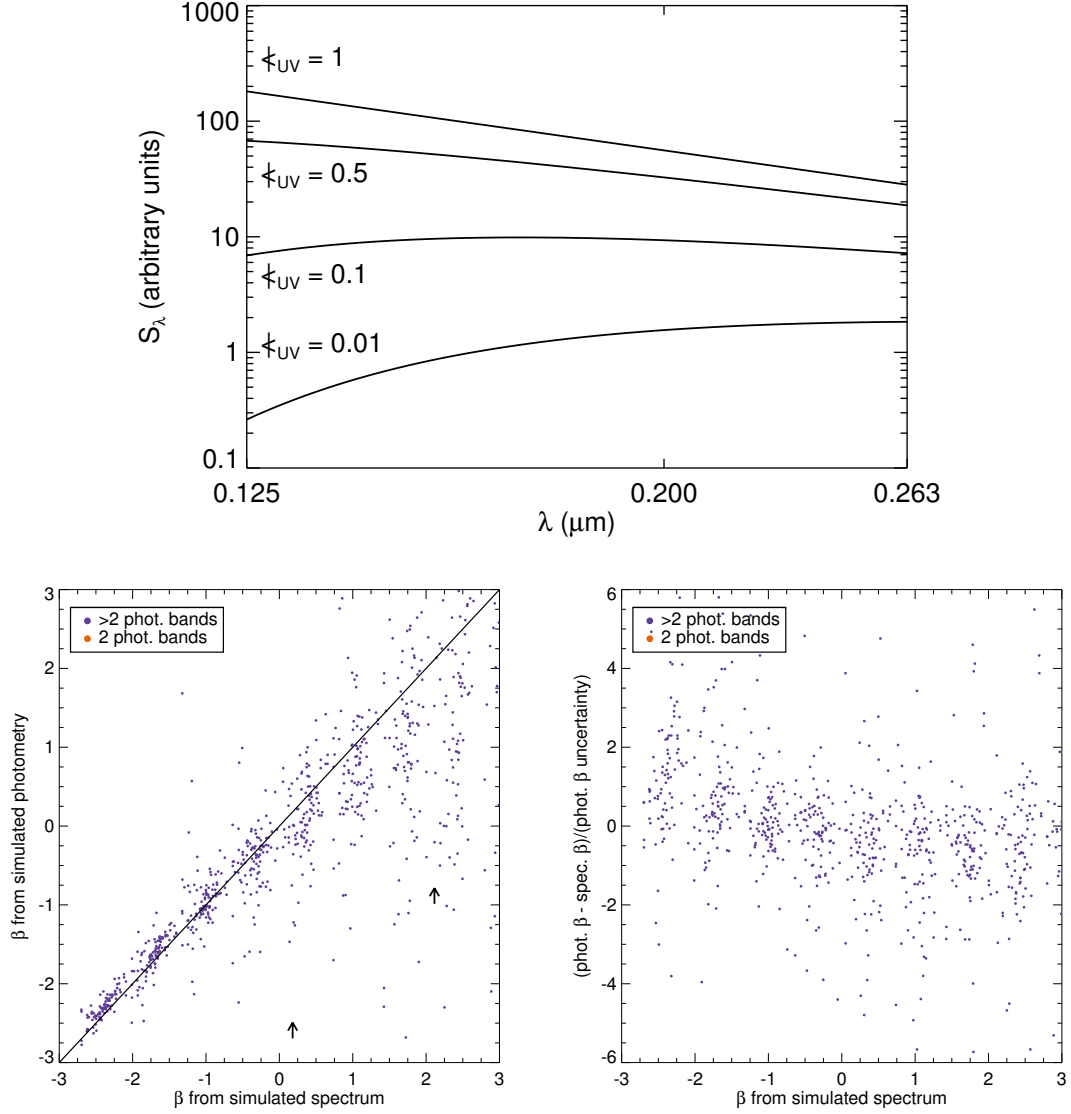


Figure 4.5 *Top*: Modifications to a perfect power law by the attenuation formula given in Eq. 4.5 for UV escape fractions of 1 (unattenuated), 0.5, 0.1, and 0.01. Compared to the Calzetti et al. (2000) attenuation formula, this formula results in continua that depart more from power laws. *Left*: β fit to photometry vs. β fit to spectra. *Right*: Difference in β values divided by the photometric β uncertainty vs. true β .

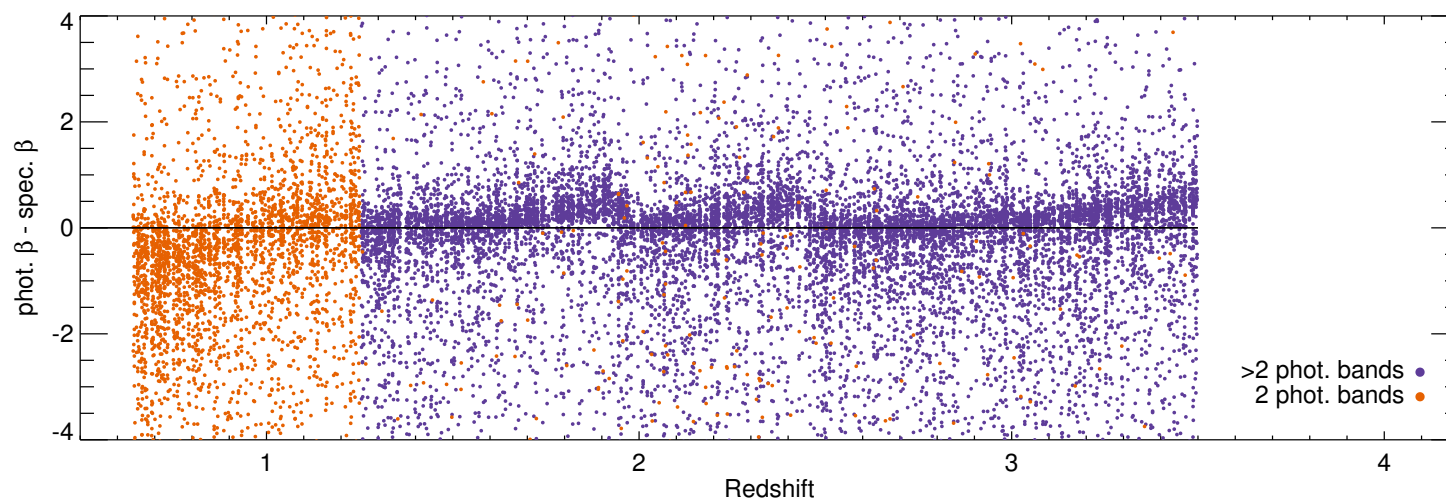


Figure 4.6 Difference in β values vs. redshift for attenuation according to Eq. 4.5, which is based on the Murphy et al. (2011) IRX- β relation. Systematic differences are due to departures of the attenuated UV continua from power laws (Fig. 4.5).

CHAPTER 5

NONUNIFORM DUST DISTRIBUTIONS IN DUSTY GALAXIES

Power law indices may be uncertain, but it is hard to use this uncertainty to dismiss the argument that UV- and IR-emitting regions in IR-luminous galaxies are spatially coincident and widely distributed. IR-luminous galaxies are dusty because their dust is pervasive. (It would have been awkward if “dust-obscured galaxies” turned out to be neither dusty nor obscured.) The next step in addressing the lifecycle of dust is to determine its morphology. Do spatial distributions of dust grains in galaxies have typical forms, like those of stars?

We investigate whether or not the distributions resemble uniform foreground screens, as commonly assumed. We use rest-frame infrared, ultraviolet, and $H\alpha$ line luminosities of dust-poor and dusty galaxies at $z \sim 0$ and $z \sim 1$ to compare measured $H\alpha$ escape fractions with those predicted by the attenuation formula. The predictions, based on UV escape fractions, overestimate the measurements for all samples. The interpretation of this result for dust-poor $z \sim 0$ galaxies is that regions with ionizing stars have more dust than regions with nonionizing UV-emitting stars. Dust distributions for these galaxies are nonuniform. The interpretation of the overestimates for dusty galaxies at both redshifts is less clear. If the attenuation formula does not apply to these galaxies, perhaps the disagreements are not physical—perhaps dust distributions in these galaxies are uniform. If the attenuation formula does apply, then dusty galaxies have nonuniform dust distributions; the distributions are more uniform than they are in dust-poor galaxies. A broad range of $H\alpha$ escape fractions at a given UV escape fraction for $z \sim 1$ dusty galaxies, if real, indicates the implausibility of the screen assumption and diverse dust morphologies.

5.1 Motivation

A galaxy’s morphology is often defined as its spatial distribution of stars. Rest-frame optical images of galaxies show diverse arrangements of their stellar components: smooth ellipticals, tightly-wound spirals, clumpy disks, barred disks, train-wrecks, fuzzballs, and whatever Willman 1 is. Little is known about their spatial distributions of dust. (The arrangement of dust is often described, oddly, as its geometry.) Yet spatial distributions of all galactic components have intrinsic value. If we want to learn about galaxies, morphology should not be a wavelength-dependent word. Surprises surely abound: for example, galaxies at $z \sim 0.3$ have dust out to several Mpc. Their average dust mass profile is a constant fraction of their average halo mass profile (Ménard et al. 2010; see also Zaritsky 1994).

Dust attenuates a galaxy’s intrinsic luminosity at ultraviolet (UV) and optical wavelengths. In the absence of better information, we assume that dust grains are distributed as a uniformly thick screen between us and the galaxy’s stars and gas. From the uniform screen assumption follows an attenuation formula that depends solely on wavelength; intrinsic luminosity is recovered from emergent luminosity and attenuation calculated from the formula.

The uniform screen assumption is unrealistic. A low-redshift galaxy with a high emergent UV luminosity and a low IR luminosity—a dust-poor galaxy—suffers a low amount of UV attenuation. The formula predicts how much $H\alpha$ attenuation it should suffer; the prediction underestimates the measured $H\alpha$ attenuation. The galaxy’s regions with $> 10 M_{\odot}$ stars, which ionize gas, have more dust than its regions with less massive stars that emit in the UV but do not ionize gas (Calzetti et al. 1994; Calzetti 1997b). While the discrepancy in amounts of dust does not invalidate the screen part of our assumption, it does invalidate the uniform part.

The screen part of our assumption is suspect, but it may be a good approximation to the

truth. As we discuss in §3.4, the screen assumption is qualitatively similar to a scenario in which dust is distributed in a large number of clumps. Liu et al. (2013) find that the dust distribution around ionizing stars in M83 is clumpy at a spatial scale of 6 pc; if the spatial resolution is degraded to 100 pc, we would conclude that the distribution around ionizing stars is a screen. If we choose to think of dust distributions as clumpy, in low-redshift dust-poor galaxies the number of clumps surrounding nonionizing UV-emitting stars is 60% of the number of clumps surrounding ionizing stars (Calzetti 1997a).

The discrepancy between the uniform screen assumption and real dust distributions in low-redshift dust-poor galaxies grows even larger if we consider sub-galactic spatial scales. A number of studies find that $H\alpha$ and UV attenuation decrease with increasing radius (Boissier et al. 2004; Prescott et al. 2007; Muñoz-Mateos et al. 2009). Not only do ionizing stars have more dust surrounding them than nonionizing UV-emitting stars—ionizing stars at large radii have less dust than ionizing stars at small radii, and similarly for nonionizing UV-emitting stars.

We know little about dust distributions in low-redshift dusty galaxies, which have high IR luminosities and variable emergent UV luminosities. Their IR emitting regions span a range of sizes, from sub- to several kpc (Díaz-Santos et al. 2010). Measuring a size is hard enough; imaging a distribution is even harder. We might conclude that a dusty galaxy has a uniform dust distribution if, for example, its measured $H\alpha$ attenuation agreed with the prediction from the attenuation formula. The complement to this conclusion is that a low-redshift dusty galaxy has a nonuniform dust distribution, like that of a dust-poor galaxy.

We have nothing more than vague and conflicting ideas of dust distributions in all high-redshift galaxies. Onodera et al. (2010), Kashino et al. (2013), and Price et al. (2013) argue for nonuniform distributions in their samples, which comprise dusty and dust-poor galaxies; Erb et al. (2006) present evidence for uniform distributions in a simi-

larly mixed sample.

In this chapter, we ask the question, For dusty galaxies at $z \sim 0$ and $z \sim 1$, how does $H\alpha$ attenuation relate to the prediction made by the attenuation formula? We: (1) show that $H\alpha$ attenuation differs from the prediction; (2) show that the relations between $H\alpha$ and UV attenuation differ from the relation for low-redshift dust-poor galaxies; and (3) argue that an interpretation in the context of dust distributions relies on the shaky assumption that the attenuation formula is universally valid.

5.2 Data

5.2.1 Measured quantities

We use IR, emergent UV, and $H\alpha$ luminosities to determine attenuation. In the following part, we detail our catalogs and samples.

5.2.1.1 Sample at $z > 0.7$

Our study uses observations of the GOODS-S, COSMOS, and UDS regions. A catalog of *Herschel*/PACS $100\mu\text{m}$ sources for GOODS-S comes from Magnelli et al. (2013); for COSMOS and UDS, we use catalogs produced for the *Herschel* survey of CANDELS regions (Inami et al. in prep). A $100\mu\text{m}$ source is defined as a $\geq 3\sigma$ flux density measurement from PSF fitting to a *Spitzer*/MIPS $24\mu\text{m}$ source, which is based on an IRAC $3.6\mu\text{m}$ source prior. In GOODS-S, the catalog has $\geq 3\sigma$ flux densities at 24, 70, 100, and $160\mu\text{m}$; in COSMOS and UDS, the catalogs have $\geq 3\sigma$ flux densities at 24, 100, 160, 250, 350, and $500\mu\text{m}$. We do not use the 250, 350, and $500\mu\text{m}$ flux densities in the COSMOS and UDS catalogs, to avoid the effects of source confusion on PSF fitting. (Including them changes our results negligibly.)

We associate each $100\mu\text{m}$ source with a $1.6\mu\text{m}$ source in the catalogs produced by CANDELS (Nayyeri et al. in prep; Galametz et al. 2013; Guo et al. 2013). The 3 optical catalogs, like the infrared catalogs, have flux densities at unique as well as shared wave-

lengths. We require the $1.6\mu\text{m}$ source to be a unique match within $0.7''$ of the position of the $100\mu\text{m}$ source's $3.6\mu\text{m}$ prior. The match radius is an estimate for maximizing the number of unique matches while minimizing the number of multiple matches.

The final quantity of interest for each matched source is an $\text{H}\alpha$ line flux or flux limit. These come from the *HST*/WFC3-IR grism surveys *AGHAST* (P.I. B. Weiner) and *3D-HST* (Brammer et al. 2012). We match each $100\mu\text{m}$ source to a counterpart in the direct image accompanying the grism observations. Two people in our group visually inspect the counterpart's spectrum and reconcile discrepant redshift assignments. The $\text{H}\alpha$ line falls in the grism's wavelength range for galaxies at $0.7 < z < 1.5$. The spectra have low enough wavelength resolution that the $\text{H}\alpha$ and $[\text{N II}]$ lines are blended; we assume that the line flux of $[\text{NII}]$ at $\lambda = 0.6583\mu\text{m}$ is 0.3 times the $\text{H}\alpha$ line flux and that the line flux of $[\text{N II}]$ at $\lambda = 0.6548\mu\text{m}$ is 0.1 times the $\text{H}\alpha$ line flux. The ratio of $[\text{N II}]$ to $\text{H}\alpha$ line fluxes depends on gas-phase metallicity so these values may not be correct for all star-forming galaxies. They should be correct for a significant fraction if $z \sim 1$ galaxies have gas-phase metallicities distributed similarly to those of low-redshift galaxies (Kauffmann et al. 2003). For each 1D spectrum with a visible and uncontaminated line complex, we fit a linear model to the continuum and Gaussian profiles to the emission lines and extract the $\text{H}\alpha$ line flux. The uncertainty on the line flux comes from the covariance matrix times the fit's reduced χ^2 . We replace $< 5\sigma$ $\text{H}\alpha$ line fluxes with limits.

Some sources will be at $0.7 < z < 1.5$ but will not have visible $\text{H}\alpha$ line flux. To determine line flux limits for these sources, we match each $100\mu\text{m}$ source to a source with a spectroscopic redshift in the catalogs of M. Dickinson (private communication), Lilly et al. (2009), and M. Cooper and B. Weiner (private communication). (Operationally both the $100\mu\text{m}$ and spectroscopic catalogs are matched to the CANDELS catalogs.) If the $100\mu\text{m}$ source has a spectroscopic redshift that is unconfirmed by an uncontaminated grism spectrum, we estimate the widths of the invisible Gaussian line profiles from the

ratio of integrated flux density to peak surface brightness in the galaxy’s region of the direct image. We then fit the same model as above to the 1D spectrum and extract the $H\alpha$ line flux uncertainty. We use 5σ limits. We are unable to determine limits for galaxies observed by the grism that are undetected in the direct image. Most limits are in GOODS-S because the spectroscopic completeness is higher there than it is in COSMOS and UDS.

To summarize, our high-redshift sample contains galaxies with: (1) detected emission at $100\mu\text{m}$; (2) detected emission at $1.6\mu\text{m}$; and (3) spectroscopically-determined redshifts at $0.7 < z < 1.5$.

5.2.1.2 Samples at $z < 0.2$

We use a nonstandard method to determine $H\alpha$ attenuation, so we measure it first for low-redshift dust-poor galaxies, which have known dust properties. We choose a sample of star-forming galaxies at $z \sim 0$ that are analogs of common star-forming galaxies at high redshift (LBAs; Overzier et al. 2009, 2011).

We use $24\mu\text{m}$ flux densities in the *Spitzer* Heritage Archive. Of the 26 sources in Overzier et al. (2011), 3 do not have reliable $24\mu\text{m}$ flux densities (per the recommendations in the enhanced imaging products quick start guide); these sources are excluded. The remainder have flux densities at 0.15 and $0.23\mu\text{m}$, from *GALEX* observations. $H\alpha$ line fluxes, from SDSS observations, are from Overzier (private communication). We multiply the line fluxes by 1.67 as a fiber-aperture correction (Overzier et al. 2009).

We also apply our method to a sample of low-redshift dusty galaxies, which have relatively unknown dust properties. Hwang & Geller (2013) collate, for low-redshift dust-obscured galaxies (DOGs) and a control sample: flux densities at 9, 12, 22, 25, 60, 100, and $140\mu\text{m}$, from *IRAS*, *AKARI*, and *WISE* observations; 0.15 and $0.23\mu\text{m}$ flux densities, from *GALEX* observations; and $H\alpha$ line fluxes, from SDSS observations. The fiber-aperture corrections for the $H\alpha$ line fluxes come from the differences, in the accompanying r -band images, between Petrosian flux densities and flux densities in apertures

with equal size to the fiber apertures.

5.2.2 Derived quantities

In the following part we detail how we estimate total IR and emergent UV luminosities, UV continuum power-law indices, and star formation rates for the galaxies in our samples.

5.2.2.1 IR luminosities

We estimate a total IR luminosity ($8\text{--}1000\,\mu\text{m}$; L_{IR}) for each galaxy. We redshift the Chary & Elbaz (2001) template spectral energy distributions (SEDs) to the distance of each galaxy. If the galaxy has one measured IR flux density, we find the SED that most closely matches that flux density and multiply the IR luminosity of the SED by the ratio between actual and predicted flux densities. If the galaxy has two or more measured IR flux densities, we introduce a multiplicative factor f for each SED. We find the best-fit f for each SED, which results in a list of f 's and χ^2 values. We choose the SED and its accompanying f that results in the minimum of all χ^2 values. The galaxy's L_{IR} is then f times the IR luminosity of the SED. (In practice, all the high- and low-redshift dusty galaxies have two or more measured IR flux densities, and all the low-redshift dust-poor galaxies have one measured IR flux density.)

Overzier et al. (2011), in their footnote 14, find that the Chary & Elbaz (2001) SEDs do not fit low-redshift dust-poor galaxies as well as other SEDs. They measured IR flux density limits at 70 and $160\,\mu\text{m}$ as well as flux densities at $24\,\mu\text{m}$. The footnote explains that the Chary & Elbaz (2001) SEDs, when fit to $24\,\mu\text{m}$ flux densities, predict flux densities at 70 and $160\,\mu\text{m}$ that fall above their upper limits. Our IR luminosities are high compared to theirs—on average, a factor of 1.4 times higher; at most, a factor of 2.5 times higher. We present results for both sets of IR luminosities for the low-redshift dust-poor galaxies.

5.2.2.2 UV continuum power-law indices and luminosities

We use the procedure in §4.2 to estimate β and C or their limits. We do not deboost low-significance flux densities because they are measured at the position of a well-detected $1.6\mu\text{m}$ source.

We estimate an emergent UV luminosity, λL_λ , or a limit at rest-frame $0.16\mu\text{m}$ ($0.16 \times L_{0.16}$) for each galaxy using its redshift and the power-law fit to the rest-frame UV flux densities.

5.2.2.3 Star formation rates

The equations in Kennicutt (1998) relate IR, emergent UV, and emergent $\text{H}\alpha$ luminosities to star formation rates (SFRs). We assume that a galaxy's total SFR: (1) is the sum of its IR- and emergent UV-derived SFR; and (2) equals the intrinsic (from the attenuation-corrected luminosity) $\text{H}\alpha$ -derived SFR. The SFR equations are valid under different assumptions for the duration of a galaxy's star formation episode. If the SFR has been constant for $\sim 10^8$ yr, so that the instantaneous $\text{H}\alpha$ -derived SFR equals the prolonged UV- and IR-derived SFRs, and as long as the dominant source for the IR luminosity is not old stars, our assumptions will not conflict with those of Kennicutt (1998).

We must exclude galaxies with active nuclei because fractions of their IR, emergent UV, and emergent $\text{H}\alpha$ luminosities will be unrelated to newly formed massive stars. We identify 5 AGN hosts among the high-redshift dusty galaxies; we use the Donley et al. (2012) criteria, which are based on mid-IR flux densities (which all 3 CANDELS catalogs have). These criteria will miss some AGN hosts (Juneau et al. 2013). We accept the contaminants because in some fields we lack data we could use to identify the missed AGN hosts.

Among the low-redshift dusty galaxies, we keep only those identified as star-forming by Hwang & Geller (2013). They use line flux ratios to discriminate between an AGN host and a star-forming galaxy without an AGN. None of the low-redshift dust-poor galax-

ies host an AGN.

5.3 Results

We define the following quantities.

- ϵ_{UV} is the escape fraction at rest-frame $0.16\,\mu\text{m}$.
- $\epsilon_{\text{H}\alpha}$ is the escape fraction of the $\text{H}\alpha$ line luminosity.
- $\epsilon_{0.66}$ is the escape fraction extrapolated from ϵ_{UV} to the wavelength of $\text{H}\alpha$ —the attenuation formula prediction. For the attenuation formula in Calzetti et al. (2000), $\epsilon_{0.66} = \epsilon_{\text{UV}}^{0.33}$.

Our hypothesis is that the $\text{H}\alpha$ and $0.66\,\mu\text{m}$ escape fractions agree—that dusty galaxies have uniform dust distributions.

Calzetti et al. (1994) argue that, in low-redshift dust-poor galaxies, regions with ionizing stars are not spatially coincident with regions with nonionizing UV-emitting stars. In this framework $\epsilon_{0.66}$ is the escape fraction of the $0.66\,\mu\text{m}$ continuum emission from massive stars and $\epsilon_{\text{H}\alpha}$ is the escape fraction of the $0.66\,\mu\text{m}$ line emission from gas ionized by even more massive stars. These galaxies have $\epsilon_{\text{H}\alpha} = \epsilon_{\text{UV}}^{0.69}$, equivalent to $\epsilon_{\text{H}\alpha} = \epsilon_{0.66}^{2.1}$ (Calzetti et al. 1994; Calzetti 1997b). Because the ionizing and nonionizing stars are not spatially coincident, the escape fractions disagree because the dust distributions are nonuniform. The ionizing stars are surrounded by more dust than are the nonionizing stars.

Their $\text{H}\alpha$ escape fractions come from the ratios of $\text{H}\alpha$ to $\text{H}\beta$ line luminosities. In the absence of dust the ratio is 2.86, so $(L_{\text{H}\alpha}/L_{\text{H}\beta})/2.86 = \epsilon_{\text{H}\alpha}/\epsilon_{\text{H}\beta}$. Since $\epsilon_{\text{H}\beta}$ is a power law function of $\epsilon_{\text{H}\alpha}$, the ratio of line luminosities uniquely determines $\epsilon_{\text{H}\alpha}$.

Their UV and $0.66\,\mu\text{m}$ escape fractions come from comparing spectra of galaxies with $\text{H}\alpha$ escape fractions of 1 to spectra of galaxies with $\text{H}\alpha$ escape fractions less than 1.

The $H\alpha$ and $H\beta$ lines in the spectra must be masked or replaced with continuum values. (This is not mentioned in Calzetti et al. 1994.) The literature relation is technically $\mathcal{A}_{H\alpha} = \mathcal{A}_{0.66}^{2.3}$. Calzetti (1997b) uses the Milky Way *extinction* formula of Howarth (1983) to determine $H\alpha$ escape fractions for low-redshift dust-poor galaxies; if we instead use the attenuation formula, we get $\mathcal{A}_{H\alpha} = \mathcal{A}_{0.66}^{2.1}$.

Our method for determining $H\alpha$ escape fractions is nonstandard; we do not have $H\beta$ luminosities for the $z \sim 1$ dusty galaxies. We first apply it to a sample of low-redshift dust-poor galaxies with the aim of reproducing the Calzetti (1997b) result.

The sample, from Overzier et al. (2011), contains galaxies that lie roughly on the low-redshift IRX- β relation. This relation is a blunt instrument we use to determine whether or not galaxies obey the attenuation formula at UV wavelengths; \mathcal{A}_{UV} is a function of IRX and the attenuation formula relates \mathcal{A}_{UV} to β . Since these galaxies lie on the relation, we do not expect them to have anomalous dust properties as compared to the properties of the galaxies in the Calzetti et al. (2000) sample. We calculate $\mathcal{A}_{H\alpha}$ and \mathcal{A}_{UV} for each galaxy in the following way.

- \mathcal{A}_{UV} from IRX: $\mathcal{A}_{UV} = (L_{IR}/(1.68 \times 0.16 \times L_{0.16}) + 1)^{-1}$. (Equivalent to $\mathcal{A}_{UV} = [\text{emergent UV SFR}]/[\text{IR SFR} + \text{emergent UV SFR}]$.)
- Following the assumptions in 5.2.2.3: $\mathcal{A}_{H\alpha} = (\text{emergent } H\alpha \text{ SFR})/(\text{IR SFR} + \text{emergent UV SFR})$.

We use these quantities to find, for the sample, a best-fit index for the form $\mathcal{A}_{H\alpha} = \mathcal{A}_{UV}^q$.

Fig. 5.1 shows that $\mathcal{A}_{H\alpha} = \mathcal{A}_{UV}^{0.80}$ for the low-redshift dust-poor galaxies. (If we use the IR and UV luminosities from Overzier et al. 2011, $\mathcal{A}_{H\alpha} = \mathcal{A}_{UV}^{0.84}$.) We do not have uncertainties on any SFRs so we also perform a robust linear regression (which requires a fit to the form $\log \mathcal{A}_{H\alpha} = q \log \mathcal{A}_{UV}$). It returns a similar result. We recover a relation close to the Calzetti (1997b) relation for similar galaxies, so we have some

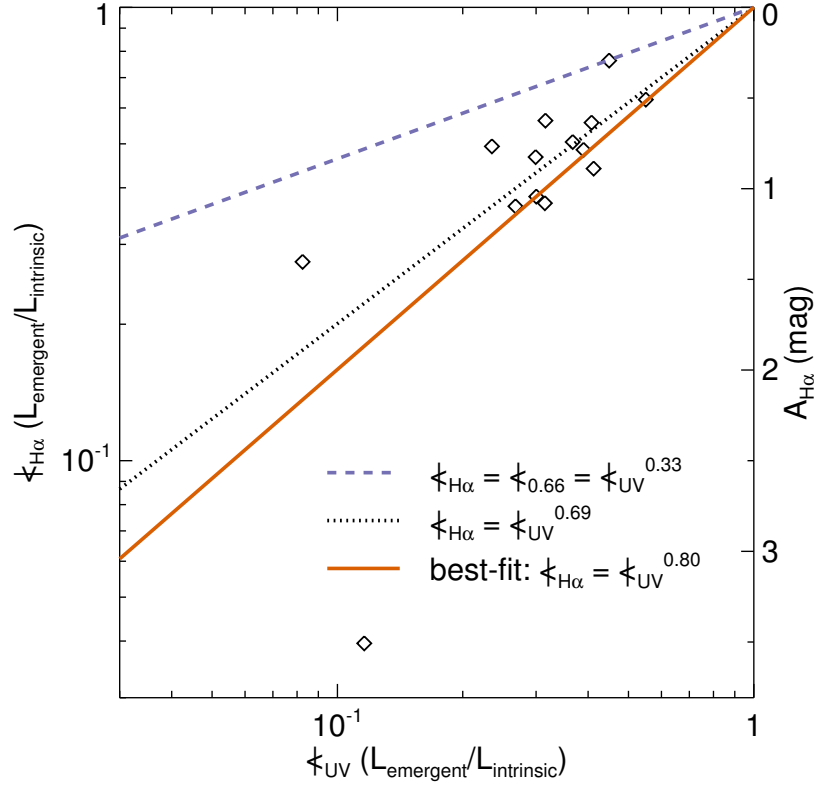


Figure 5.1 The $H\alpha$ escape fraction, $\zeta_{H\alpha}$, as a function of the UV escape fraction, ζ_{UV} , for the low-redshift dust-poor galaxies. The dashed purple line shows $\zeta_{0.66}$, the extrapolation of ζ_{UV} to the wavelength of $H\alpha$ using the Calzetti et al. (2000) attenuation formula, as a function of ζ_{UV} . This is the uniform dust distribution hypothesis for the attenuation formula. Calzetti (1997b), who study another sample of low-redshift dust-poor galaxies, find that $H\alpha$ escape fractions are lower than this extrapolation (dotted black line). We find a similar result (solid orange line).

confidence that our procedure is not grossly incorrect. We stress, again, that there are no evolutionary connections between the low- and high-redshift galaxy samples; we aim only to reproduce the Calzetti (1997b) result with our nonstandard method of determining $\zeta_{H\alpha}$.

Fig. 5.2 shows that $\zeta_{\text{H}\alpha} = \zeta_{\text{UV}}^{0.55}$ for the low-redshift dusty galaxies. We use uncertainties only on the emergent H α -derived SFR (we treat it as the dependent variable) in the weighted fit.

Fig. 5.3 shows that $\zeta_{\text{H}\alpha} = \zeta_{\text{UV}}^{0.55}$ for high-redshift dusty galaxies. We do not include limits in this fit. The uncertainty in the index is very small; this is not surprising given the number of galaxies. The dispersion about the best-fit relation is large; the central 50% of galaxies with H α -detected SFRs lies between $\zeta_{\text{H}\alpha} = \zeta_{\text{UV}}^{0.45}$ and $\zeta_{\text{H}\alpha} = \zeta_{\text{UV}}^{0.66}$. A survival regression, which incorporates H α SFR limits in a fit to the form $\log \zeta_{\text{H}\alpha} = q \log \zeta_{\text{UV}}$, finds $q = 0.47$, as does a simple linear regression using only the H α -detected SFRs. (None of the galaxies have limits for both the UV and H α SFRs.) The main effect of including limits in the regression is to increase the standard error of the sample's best-fit index; a marginally different index is a secondary effect.

The escape fraction relations of dusty galaxies are subject to selection effects. The best-fit relation for the low-redshift dusty galaxies seems to underestimate H α escape fractions at low UV escape fractions (Fig. 5.2). This may reflect our constraint that $\zeta_{\text{H}\alpha} = 1$ when $\zeta_{\text{UV}} = 1$, but the lack of galaxies with H α escape fractions at or below the relation may be due to galaxies with H α SFRs below the limit of the sample. We do not measure H α line flux limits for galaxies that meet the selection criteria of Hwang & Geller (2013) and have undetected H α line fluxes. If we replace all H α -detected SFRs with SFRs corresponding to the minimum H α line flux of the sample, we fill in the space around the relation.

High-redshift dusty galaxies with UV escape fractions $< 10^{-2}$ seem to have less dispersion in their H α escape fractions than do galaxies with UV escape fractions $> 10^{-2}$. Despite our best efforts to measure H α line flux limits, we still lack them for galaxies lacking spectroscopic redshifts. If we replace all H α -detected SFRs with SFRs corresponding to a reasonable H α line flux limit for the grism observations ($5 \times 10^{-17} \text{ erg s}^{-1}$

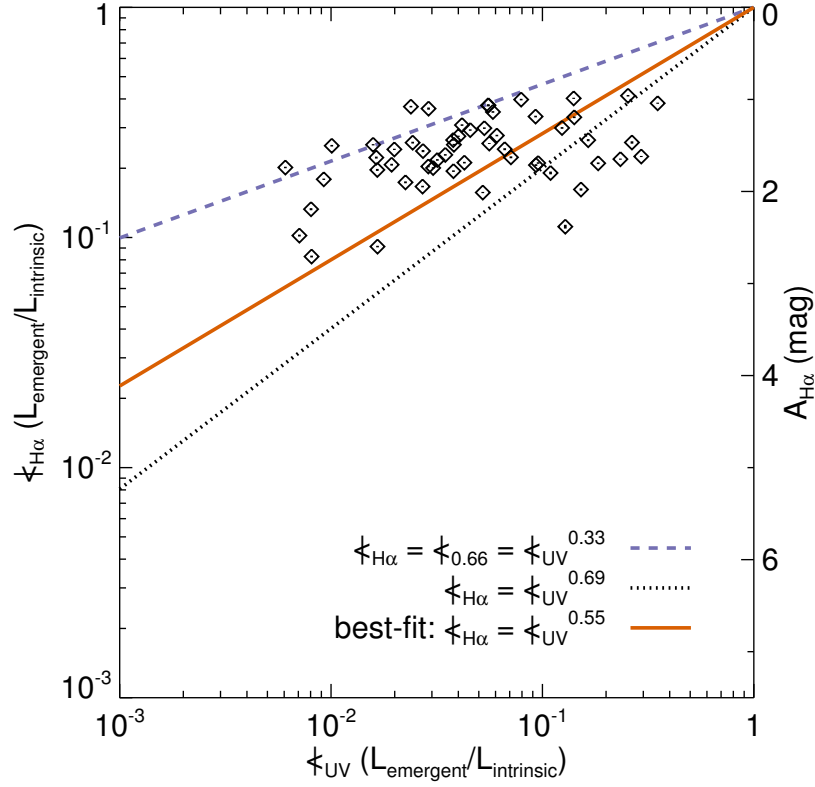


Figure 5.2 The $H\alpha$ escape fraction, $f_{H\alpha}$, as a function of the UV escape fraction, f_{UV} , for the low-redshift dusty galaxies. The dashed purple line shows $f_{0.66}$, the extrapolation of f_{UV} to the wavelength of $H\alpha$ using the Calzetti et al. (2000) attenuation formula, as a function of f_{UV} . This is the uniform dust distribution hypothesis for the attenuation formula. If low-redshift dust-poor galaxies were to have this range of UV escape fractions, their $H\alpha$ escape fractions would be lower than this extrapolation (dotted black line). Our fit is the solid orange line. We find that, in low-redshift dusty galaxies, regions with ionizing stars have lower escape fractions than the extrapolation and higher escape fractions than they would in low-redshift dust-poor galaxies.

cm^{-2}), we fill in the space with low $H\alpha$ escape fractions at low UV escape fractions. The decrease in dispersion is probably an artifact of the grism detection limit and a paucity of

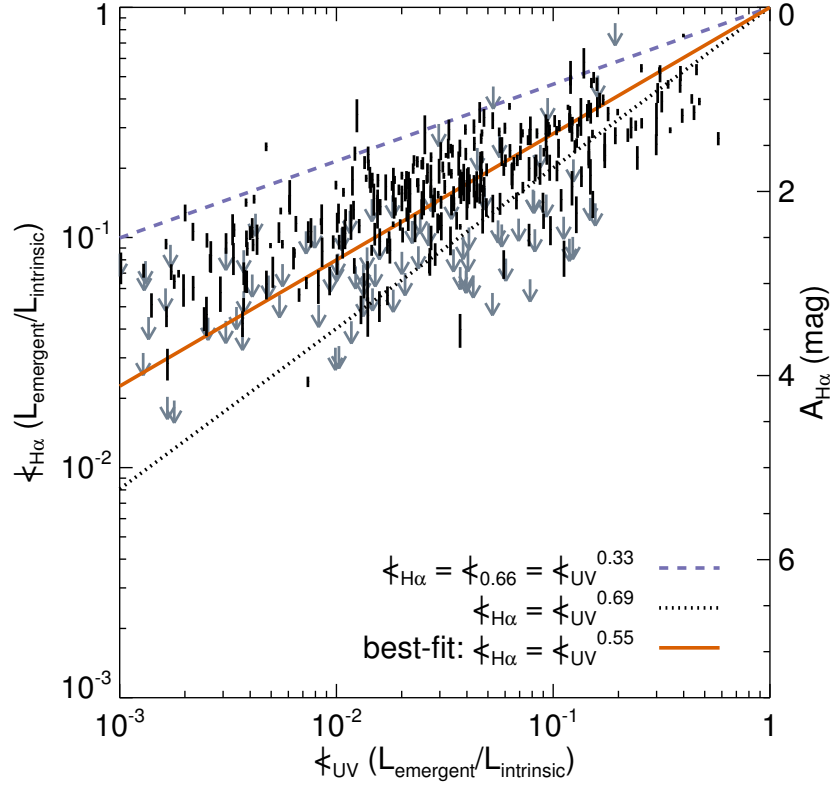


Figure 5.3 The $H\alpha$ escape fraction, $f_{H\alpha}$, as a function of the UV escape fraction, f_{UV} , for the high-redshift dusty galaxies. The dashed purple line shows $f_{0.66}$, the extrapolation of f_{UV} to the wavelength of $H\alpha$ using the Calzetti et al. (2000) attenuation formula, as a function of f_{UV} . This is the uniform dust distribution hypothesis for the attenuation formula. If low-redshift dust-poor galaxies were to have this range of UV escape fractions, their $H\alpha$ escape fractions would be lower than this extrapolation (dotted black line). Our fit is the solid orange line. We find that, in high-redshift dusty galaxies, regions with ionizing stars have lower escape fractions than the extrapolation and higher escape fractions than they would in low-redshift dust-poor galaxies.

spectroscopic redshifts in COSMOS and UDS.

5.4 Discussion

If we assume that dusty galaxies obey the Calzetti et al. (2000) attenuation formula, our results indicate that their $H\alpha$ and $0.66\mu\text{m}$ escape fractions disagree. Unlike low-redshift dust-poor galaxies, dusty galaxies have $\zeta_{H\alpha} = \zeta_{0.66}^{1.6}$; like low-redshift dust-poor galaxies, dusty galaxies have nonuniform dust distributions. The relations between $\zeta_{H\alpha}$ and $\zeta_{0.66}$ are similar to those found by Onodera et al. (2010), Kashino et al. (2013), and Price et al. (2013) and conflict with those of Erb et al. (2006). These studies assume the applicability of the attenuation formula, and use samples of high-redshift galaxies that are not necessarily dusty. Their UV escape fractions come from stellar population modeling, while ours come from IRX; their $H\alpha$ escape fractions come from ratios of averaged $H\alpha$ to averaged $H\beta$ luminosities, while ours come from assumptions about SFRs.

However, dusty galaxies may not obey the Calzetti et al. (2000) attenuation formula, which complicates our interpretation of the more basic relation between UV and $0.66\mu\text{m}$ escape fractions—the relation between escape fractions for just the regions with nonionizing UV-emitting stars (Reddy et al. 2010, 2012; Buat et al. 2011, 2012; Penner et al. 2012; Kriek & Conroy 2013). The true attenuation formula for dusty galaxies may have a higher $0.66\mu\text{m}$ escape fraction for a given UV escape fraction. An attenuation formula modified according to Kriek & Conroy (2013)—with $\delta = -0.2$ and no bump—has $\zeta_{0.66} = \zeta_{UV}^{0.25}$ instead of $\zeta_{0.66} = \zeta_{UV}^{0.33}$. The combination of this Kriek & Conroy (2013) attenuation formula and our result implies that $\zeta_{H\alpha} = \zeta_{0.66}^{2.2}$. If the true attenuation formula instead has a much lower $0.66\mu\text{m}$ escape fraction for a given UV escape fraction— $\zeta_{0.66} = \zeta_{UV}^{0.55}$ —we conclude that, for dusty galaxies, the $H\alpha$ and $0.66\mu\text{m}$ escape fractions agree. Our conclusion regarding the uniformity of dust distributions depends on the assumed attenuation formula. We cannot reject our hypothesis. The unambiguous statement we make is that dusty galaxies have relations between $H\alpha$ and UV escape fractions that are different from the relation for low-redshift dust-poor galaxies.

The dispersion about the best-fit relation for high-redshift dusty galaxies is large, yet it is not immune to our possibly invalid assumption that a galaxy's instantaneous SFR has, for at least 10^8 yr, equaled its prolonged SFR. For example, if most massive stars formed over 15 Myr instead of 300 Myr, we should multiply $L_{0.16}$ and L_{IR} by larger numbers than we do here to derive the UV and IR SFRs. The true UV SFR is 57% higher and the true IR SFR is 63% higher (Madau & Dickinson 2014). The true UV escape fraction is little different; because the true total SFR is higher, the true $\text{H}\alpha$ escape fraction is lower. (Another scenario is that massive stars stopped forming within the last 15 Myr.) Perhaps some of the galaxies in Fig. 5.3 have complicated star formation histories; the combined effect of deriving correct SFRs might lead to lower dispersion.

There are few ways to resolve the uncertainties regarding star formation histories and the applicability of the Calzetti et al. (2000) attenuation formula to dusty galaxies. One (partial) way is to use the formula and $\zeta_{\text{H}\alpha}$ to predict the escape fraction of the $\text{H}\beta$ luminosity, $\zeta_{\text{H}\beta}$. Both line luminosities are from ionized gas surrounding the same stars, so this prediction is immune to an uncertain star formation history. The ratio of intrinsic $\text{H}\alpha$ to $\text{H}\beta$ luminosities is 2.86 (under reasonable assumptions); with $\text{H}\beta$ observations, we can use $(L_{\text{H}\alpha}/L_{\text{H}\beta})/2.86 = \zeta_{\text{H}\alpha}/\zeta_{\text{H}\beta}$ and from this determine $\zeta_{\text{H}\beta}$. If the predicted and determined $\text{H}\beta$ escape fractions agree, the assumed attenuation formula is probably valid at optical wavelengths; the assumed star formation histories are also probably valid. If the predicted and determined fractions disagree, the attenuation formula at optical wavelengths can be different (for example, due to dust not distributed as a uniform foreground screen; Calzetti 2001) or the true $\zeta_{\text{H}\alpha}$ can be different. Fig. 5.4 shows this test applied to the low-redshift dusty galaxies. To apply this test to high-redshift dusty galaxies, we need near-IR spectra that cover the $\text{H}\beta$ line. If the dispersion of $\text{H}\alpha$ escape fractions at a given UV escape fraction for high-redshift dusty galaxies does not go away, there must be a diversity of dust distributions. Either way, this test provides no information on the

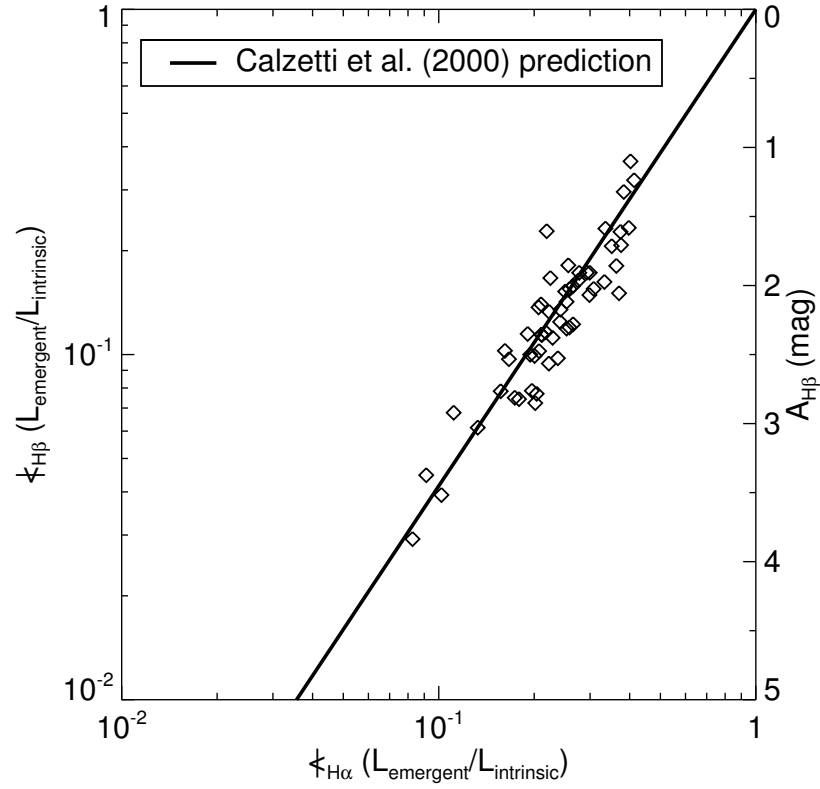


Figure 5.4 $H\beta$ escape fraction, $\zeta_{H\beta}$, as a function of $H\alpha$ escape fraction, $\zeta_{H\alpha}$, for the low-redshift dusty galaxies. We determine $\zeta_{H\beta}$ using $\zeta_{H\alpha}$ and the ratios of $H\alpha$ and $H\beta$ luminosities. The Calzetti et al. (2000) attenuation formula has $\zeta_{H\beta} = \zeta_{H\alpha}^{1.38}$ (solid black line). If $H\beta$ measurements of high-redshift dusty galaxies agree with the prediction, we can resolve uncertainties related to star formation histories and the validity of the attenuation formula at optical wavelengths; otherwise, we might not.

relation between UV and $0.66\,\mu\text{m}$ escape fractions; more extrapolations are necessary to definitively interpret Figs. 5.2 and 5.3.

5.5 Summary

1. We measure $H\alpha$ line luminosities and limits, from *HST*/WFC3-IR grism spectra, for $z \sim 1$ galaxies with detected $100\mu\text{m}$ emission. We determine rest-frame UV continuum power-law indices (β values) and ratios of IR to UV luminosities (IRX values).
2. For each galaxy we determine ϵ_{UV} , the escape fraction at $0.16\mu\text{m}$, from IRX. We determine $\epsilon_{\text{H}\alpha}$, the $H\alpha$ escape fraction, from the $H\alpha$ luminosity and the total star formation rate.
3. For the Overzier et al. (2011) sample of low-redshift dust-poor galaxies, we recover the Calzetti (1997b) relation between $H\alpha$ and UV escape fractions: $\epsilon_{\text{H}\alpha} = \epsilon_{\text{UV}}^{0.80}$. Our nonstandard method for determining $H\alpha$ escape fractions should not be grossly incorrect.
4. For the Hwang & Geller (2013) sample of low-redshift dusty galaxies, we find that $\epsilon_{\text{H}\alpha} = \epsilon_{\text{UV}}^{0.55}$.
5. For our sample of dusty galaxies at $0.7 < z < 1.5$, we find that $\epsilon_{\text{H}\alpha} = \epsilon_{\text{UV}}^{0.55}$. The dispersion about the best-fit relation is large.
6. The interpretation of the results for dusty galaxies is unclear. If we assume that the Calzetti et al. (2000) attenuation formula applies to these galaxies, our results agree with those of Onodera et al. (2010), Kashino et al. (2013), and Price et al. (2013) and conflict with those of Erb et al. (2006). They study samples comprising dust-poor and dusty galaxies. Dusty galaxies have nonuniform dust distributions. However, dusty galaxies may not obey the attenuation formula.
7. Measurements of the ratios of $H\alpha$ to $H\beta$ luminosities may decrease the dispersion in the relation between $H\alpha$ and UV escape fractions for dusty galaxies at $z \sim 1$. If

the dispersion is real, these galaxies have diverse dust distributions.

ALMA is beginning to produce images of the dust distributions in galaxies. These images lead to direct tests—independent of the attenuation formula—of the uniform screen assumption. They also have the potential to reveal the parts of galaxies that may never be detected at UV and optical wavelengths: surprises surely abound.

CHAPTER 6

FUTURE DIRECTIONS

The evolution of a galaxy's dust mass is not simple. Dust grains of different sizes are created and destroyed by different processes, and how they are distributed is tied to where they form. Stars and supernovae form large grains; then the grains are destroyed by shocks or intense radiation from hot gas, consumed by forming stars, or shattered into smaller grains by collisions with other large grains; then the small grains grow large again, through accretion of metals, atom by atom, or through coagulation with other small grains. Formation occurs where the massive stars are while shattering, accretion, and coagulation occur in the ISM.

We have to consider more than the physical evolution of a galaxy's dust mass—selection effects may be strong. The average dust mass of submillimeter-selected galaxies is five times larger at $z \sim 0.5$ than it is at $z \sim 0$ (Dunne et al. 2011). The millimeter background results, along with luminosity function evolution, argue for dust mass evolution from even higher redshifts. However, as Dunne et al. (2011) discuss, how we select the galaxies may have much to do with how we interpret this evolution. High-redshift dusty galaxies might be detected at millimeter wavelengths; if they destroy their dust quickly, their low-redshift descendants will not be detected at submillimeter wavelengths. Evolutionary studies need to connect progenitors to descendants through number densities set by the stellar masses of the progenitors (Behroozi et al. 2013).

Galaxies which already have high stellar masses and star formation rates at $z \sim 2$ cannot have high star formation rates for very much longer; otherwise, they would evolve into low-redshift galaxies with too-high stellar masses. High-redshift galaxies of this sort are prime targets for studying dust mass evolution. Since we are witnessing them form most of their stars, they probably do not produce, at lower redshifts, much more dust

through asymptotic giant branch (AGB) stars and supernovae. (That is, produce much more dust after the stars formed at $z \sim 2$ evolve out of these phases.) And since we can estimate the stellar masses of these galaxies, we can connect them to their low-redshift descendants.

The first step in studying the evolution of galaxies' dust masses is to estimate dust masses. We need rest-frame far-infrared flux densities, to estimate dust temperatures, and millimeter flux densities, to estimate the masses themselves. Take, for example, the detected galaxies in the millimeter map (Table 2.1). If we assume that they are all at $z = 2.7$ and have dust temperatures of 30 K (Chapin et al. 2009), their dust masses range from 3×10^8 to $2 \times 10^9 M_\odot$ (eq. 2 in Hughes et al. 1997; also, eq. 4 in Hildebrand 1983).

The second step is to identify descendants. Many people argue that millimeter galaxies will evolve into passive galaxies at low redshift. Approximately 5% of passive galaxies at $z \sim 0$ are dusty, with dust masses ranging from 9×10^5 to $4 \times 10^8 M_\odot$ (Rowlands et al. 2012). Rowlands et al. (2012) argue that most of the dust in these passive galaxies comes from accretion and coagulation in ISM—not from stellar sources. But they base their estimates on the low numbers of stars forming at $z \sim 0$. They consider as unlikely that the galaxies formed much of their dust in earlier episodes of star formation. As Rowlands et al. (2012) note, we need X-ray and CO observations of the passive galaxies: to rule out that they have hot gas, which would destroy dust created at high redshift on very short timescales; or to confirm that they have cold gas, which would shield dust from emission from hot gas. If the $z \sim 2$ millimeter galaxies evolve into the dusty $z \sim 0$ passive galaxies, they might lose anywhere from 90% to almost all of their dust. We might not need to invoke dust formation in the ISM to explain the dust masses of low-redshift passive galaxies.

Or perhaps the descendants of millimeter galaxies are the passive galaxies that lack dust. They might have stellar metallicities that are much higher than the metallicities of

the descendants of high-redshift dust-poor galaxies. Stars formed at $z \sim 2$ may consume all their surrounding dust; if this is the case, the distributions of dust must align with those of stars. Perhaps the consumption was only possible because the distributions of dust in high-redshift dusty galaxies were more uniform than the distributions of dust in low-redshift dust-poor galaxies (assuming the validity of the Calzetti et al. 2000 escape fraction formula). For this hypothesis, knowing what destroys the dust requires concomitant tracking of dust masses and metallicities for galaxies that share common histories. If astration does not rid galaxies of dust, perhaps galactic winds do; perhaps the descendants of millimeter galaxies have more dust at several Mpc than do the descendants of other galaxies.

We started this thought experiment with galaxies at $z \sim 2$ which: (1) have high stellar masses; and (2) probably form no more dust through AGB stars and supernovae; and used these assumptions to explore dust destruction, or its formation in the ISM. We might also be able to constrain the amount of dust created by supernovae at higher redshifts. With only dust temperatures and masses, this constraint is a difficult one to make—it requires knowledge of a galaxy’s star formation history and the amount of dust created in each supernova. The dust mass, at $z \sim 2$, divided by the dust yield from exploding stars, at higher redshifts, would be unity if all the dust mass comes from supernovae. A more straightforward constraint comes from detailed knowledge of the escape fraction formula.

We interpret the wavelength dependence of the Calzetti et al. (2000) formula as from, in part, a grain size distribution. As the sizes of grains increase, they become more effective at attenuating longer wavelengths of UV emission. Different size distributions thus lead to different escape fraction formulas.

Dust grains created in supernovae have a unique composition and size distribution (Todini & Ferrara 2001). Specifically, they have a size distribution that results in a formula with a broad, shallow depression near $0.3 \mu\text{m}$ (see fig. 1 in Hjorth et al. 2013). We

expect galaxies with significant dust created by supernovae to obey an *attenuation* formula with this depression. A much more prominent depression, at $0.2175\ \mu\text{m}$, is in the attenuation formula for high-redshift dusty galaxies (and in the *extinction* formula for the Milky Way; §3.4). Those findings require narrowband photometry, which we would need as well. (Alternatively, we could use spectra, if they are sensitive enough.) If we can determine the escape fraction formula for dusty galaxies at $z \sim 2$, we might falsify the presence of dust created by supernovae. (Maiolino et al. 2004 find evidence for dust created by supernovae in a $z \sim 6$ quasar; Hjorth et al. 2013 argue that the evidence is weak.)

More generally, as galaxies transition from dusty, at high redshift, to dust-poor, at low redshift, we expect their escape fraction formulas to evolve. As large grains, formed by supernovae or AGB stars, shatter in the ISM, they become less effective at attenuating longer UV wavelengths and more effective at attenuating shorter UV wavelengths. The total effect of shattering on the evolution of the escape fraction formula is complicated by the migration of the dust from around stars to the ambient ISM. What we need in a model are: (1) grain size distributions, which relate to the processes creating and destroying dust, as a function of redshift; and (2) spatial distributions.

Grain size and spatial distributions exist for dust-poor galaxies at low redshift. Weingartner & Draine (2001) determine grain size distributions that reproduce the escape fraction formulas for the *extinction of stellar emission* in the Milky Way, LMC, and SMC. Calzetti et al. (1994) take the escape fraction formula for extinction in the Milky Way and determine the spatial distribution that reproduces the escape fraction formula for the *attenuation of galactic emission*. The spatial distribution is the uniform foreground screen.

We need to perform similar studies of dusty high-redshift galaxies. (Asano et al. 2013, 2014 present a first effort in modeling the evolution of the escape fraction formula for ex-

tion in the Milky Way.) With detailed knowledge of the escape fraction formula at UV and optical wavelengths, as mentioned in this section and in §3.5, we can start modeling combinations of grain size and spatial distributions until we reproduce the formula, the high-redshift IRX- β relation, and the relation between $H\alpha$ and UV escape fractions.

The research in this thesis deals with two major questions:

- When do galaxies contribute to the millimeter background?
- Where is the dust in galaxies at those times?

While dust may be pervasive in a common galaxy at high redshift, these answers lead only to a partial census of the lifecycle of dust. A full census will come from future research on the properties tied to its creation and destruction.

REFERENCES

- Alexander, D. M., Bauer, F. E., Brandt, W. N., et al. 2003, *AJ*, 126, 539
- Asano, R. S., Takeuchi, T. T., Hirashita, H., & Nozawa, T. 2014, *MNRAS*, 459
- Asano, R. S., Takeuchi, T. T., Hirashita, H., & Nozawa, T. 2013, *MNRAS*, 432, 637
- Barger, A. J., Cowie, L. L., & Wang, W.-H. 2008, *ApJ*, 689, 687
- Bauer, A. E., Conselice, C. J., Pérez-González, P. G., et al. 2011, *MNRAS*, 417, 289
- Behroozi, P. S., Marchesini, D., Wechsler, R. H., et al. 2013, *ApJL*, 777, L10
- Bertin, E., & Arnouts, S. 1996, *A&AS*, 117, 393
- Béthermin, M., Dole, H., Cousin, M., & Bavouzet, N. 2010, *A&A*, 516, A43
- Boissier, S., Boselli, A., Buat, V., Donas, J., & Milliard, B. 2004, *A&A*, 424, 465
- Brammer, G. B., van Dokkum, P. G., Franx, M., et al. 2012, *ApJS*, 200, 13
- Buat, V., Noll, S., Burgarella, D., et al. 2012, *A&A*, 545, A141
- Buat, V., Giovannoli, E., Heinis, S., et al. 2011, *A&A*, 533, A93
- Bussmann, R. S., Dey, A., Lotz, J., et al. 2011, *ApJ*, 733, 21
- Bussmann, R. S., Dey, A., Borys, C., et al. 2009, *ApJ*, 705, 184
- Bussmann, R. S., Dey, A., Lotz, J., et al. 2009, *ApJ*, 693, 750
- Calzetti, D. 2001, *PASP*, 113, 1449
- Calzetti, D., Armus, L., Bohlin, R. C., et al. 2000, *ApJ*, 533, 682

- Calzetti, D. 1997, American Institute of Physics Conference Series, 408, 403
- Calzetti, D. 1997, AJ, 113, 162
- Calzetti, D., Kinney, A. L., & Storchi-Bergmann, T. 1994, ApJ, 429, 582
- Capak, P., Cowie, L. L., Hu, E. M., et al. 2004, AJ, 127, 180
- Chapin, E. L., Pope, A., Scott, D., et al. 2009, MNRAS, 398, 1793
- Chapman, S. C., Blain, A. W., Smail, I., & Ivison, R. J. 2005, ApJ, 622, 772
- Charmandaris, V., Le Floch, E., & Mirabel, I. F. 2004, ApJL, 600, L15
- Chary, R.-R., & Pope, A. 2010, arXiv:1003.1731
- Chary, R., & Elbaz, D. 2001, ApJ, 556, 562
- Coppin, K., Halpern, M., Scott, D., Borys, C., & Chapman, S. 2005, MNRAS, 357, 1022
- Daddi, E., Alexander, D. M., Dickinson, M., et al. 2007, ApJ, 670, 173
- Devlin, M. J., Ade, P. A. R., Aretxaga, I., et al. 2009, Nature, 458, 737
- Dey, A., Soifer, B. T., Desai, V., et al. 2008, ApJ, 677, 943
- Díaz-Santos, T., Charmandaris, V., Armus, L., et al. 2010, ApJ, 723, 993
- Dickinson, M., Giavalisco, M., & GOODS Team 2003, The Mass of Galaxies at Low and High Redshift, 324
- Dole, H., Lagache, G., Puget, J.-L., et al. 2006, A&A, 451, 417
- Donley, J. L., Koekemoer, A. M., Brusa, M., et al. 2012, ApJ, 748, 142
- Draine, B. T. 2009, Cosmic Dust—Near and Far, 414, 453

- Drory, N., Bender, R., & Hopp, U. 2004, *ApJL*, 616, L103
- Dunne, L., Gomez, H. L., da Cunha, E., et al. 2011, *MNRAS*, 417, 1510
- Dye, S., Eales, S. A., Ashby, M. L. N., et al. 2006, *ApJ*, 644, 769
- Elbaz, D., Dickinson, M., Hwang, H. S., et al. 2011, *A&A*, 533, A119
- Elbaz, D., Hwang, H. S., Magnelli, B., et al. 2010, *A&A*, 518, L29
- Elbaz, D., Daddi, E., Le Borgne, D., et al. 2007, *A&A*, 468, 33
- Elston, R., Rieke, G. H., & Rieke, M. J. 1988, *ApJL*, 331, L77
- Erb, D. K., Steidel, C. C., Shapley, A. E., et al. 2006, *ApJ*, 647, 128
- Fiore, F., Grazian, A., Santini, P., et al. 2008, *ApJ*, 672, 94
- Fixsen, D. J., Dwek, E., Mather, J. C., Bennett, C. L., & Shafer, R. A. 1998, *ApJ*, 508, 123
- Galametz, A., Grazian, A., Fontana, A., et al. 2013, *ApJS*, 206, 10
- Gilli, R., Daddi, E., Chary, R., et al. 2007, *A&A*, 475, 83
- Gispert, R., Lagache, G., & Puget, J. L. 2000, *A&A*, 360, 1
- Goldader, J. D., Meurer, G., Heckman, T. M., et al. 2002, *ApJ*, 568, 651
- Gordon, K. D., Calzetti, D., & Witt, A. N. 1997, *ApJ*, 487, 625
- Graham, J. R., & Dey, A. 1996, *ApJ*, 471, 720
- Greve, T. R., Weiß, A., Walter, F., et al. 2010, *ApJ*, 719, 483
- Greve, T. R., Pope, A., Scott, D., et al. 2008, *MNRAS*, 389, 1489

- Greve, T. R., Ivison, R. J., Bertoldi, F., et al. 2004, MNRAS, 354, 779
- Griffin, M. J., Abergel, A., Abreu, A., et al. 2010, A&A, 518, L3
- Grogin, N. A., Kocevski, D. D., Faber, S. M., et al. 2011, ApJS, 197, 35
- Guo, Y., Ferguson, H. C., Giavalisco, M., et al. 2013, ApJS, 207, 24
- Hildebrand, R. H. 1983, QJRAS, 24, 267
- Hogg, D. W., & Turner, E. L. 1998, PASP, 110, 727
- Howarth, I. D. 1983, MNRAS, 203, 301
- Hughes, D. H., Dunlop, J. S., & Rawlings, S. 1997, MNRAS, 289, 766
- Hwang, H. S., & Geller, M. J. 2013, ApJ, 769, 116
- Hwang, H. S., Elbaz, D., Lee, J. C., et al. 2010, A&A, 522, A33
- Hu, E. M., & Ridgway, S. E. 1994, AJ, 107, 1303
- Hjorth, J., Vreeswijk, P. M., Gall, C., & Watson, D. 2013, ApJ, 768, 173
- Juneau, S., Dickinson, M., Bournaud, F., et al. 2013, ApJ, 764, 176
- Kartaltepe, J. S., Dickinson, M., Alexander, D. M., et al. 2012, ApJ, 757, 23
- Kashino, D., Silverman, J. D., Rodighiero, G., et al. 2013, ApJL, 777, L8
- Kauffmann, G., Heckman, T. M., Tremonti, C., et al. 2003, MNRAS, 346, 1055
- Kennicutt, R., 1999, ARA&A, 36, 189
- Kriek, M., & Conroy, C. 2013, ApJL, 775, L16
- Kurczynski, P., & Gawiser, E. 2010, AJ, 139, 1592

- Lagache, G., Puget, J.-L., & Dole, H. 2005, *ARA&A*, 43, 727
- Lilly, S. J., Le Brun, V., Maier, C., et al. 2009, *ApJS*, 184, 218
- Lin, L., Dickinson, M., Jian, H.-Y., et al. 2012, *ApJ*, 756, 71
- Liu, G., Calzetti, D., Hong, S., et al. 2013, *ApJL*, 778, L41
- Madau, P., & Dickinson, M. 2014, *arXiv:1403.0007*
- Magdis, G. E., Daddi, E., Elbaz, D., et al. 2011, *ApJL*, 740, L15
- Magnelli, B., Popesso, P., Berta, S., et al. 2013, *A&A*, 553, A132
- Magnelli, B., Elbaz, D., Chary, R. R., et al. 2011, *A&A*, 528, A35
- Magnelli, B., Elbaz, D., Chary, R. R., et al. 2009, *A&A*, 496, 57
- Maiolino, R., Schneider, R., Oliva, E., et al. 2004, *Nature*, 431, 533
- Marsden, G., Ade, P. A. R., Bock, J. J., et al. 2009, *ApJ*, 707, 1729
- McCarthy, P. J. 2004, *ARA&A*, 42, 477
- Melbourne, J., Soifer, B. T., Desai, V., et al. 2012, *AJ*, 143, 125
- Ménard, B., Scranton, R., Fukugita, M., & Richards, G. 2010, *MNRAS*, 405, 1025
- Meurer, G. R., Heckman, T. M., & Calzetti, D. 1999, *ApJ*, 521, 64
- Michałowski, M. J., Murphy, E. J., Hjorth, J., et al. 2010, *A&A*, 522, A15
- Michałowski, M. J., Watson, D., & Hjorth, J. 2010, *ApJ*, 712, 942
- Moustakas, J., Coil, A. L., Aird, J., et al. 2013, *ApJ*, 767, 50
- Mullaney, J. R., Pannella, M., Daddi, E., et al. 2012, *MNRAS*, 419, 95

- Muñoz-Mateos, J. C., Gil de Paz, A., Boissier, S., et al. 2009, *ApJ*, 701, 1965
- Murphy, E. J., Chary, R.-R., Dickinson, M., et al. 2011, *ApJ*, 732, 126
- Narayanan, D., Dey, A., Hayward, C. C., et al. 2010, *MNRAS*, 407, 1701
- Noeske, K. G., Weiner, B. J., Faber, S. M., et al. 2007, *ApJL*, 660, L43
- Noll, S., Pierini, D., Cimatti, A., et al. 2009, *A&A*, 499, 69
- Onodera, M., Arimoto, N., Daddi, E., et al. 2010, *ApJ*, 715, 385
- Overzier, R. A., Heckman, T. M., Wang, J., et al. 2011, *ApJL*, 726, L7
- Overzier, R. A., Heckman, T. M., Tremonti, C., et al. 2009, *ApJ*, 706, 203
- Pannella, M., Gabasch, A., Goranova, Y., et al. 2009, *ApJ*, 701, 787
- Pannella, M., Carilli, C. L., Daddi, E., et al. 2009, *ApJL*, 698, L116
- Papovich, C., Moustakas, L. A., Dickinson, M., et al. 2006, *ApJ*, 640, 92
- Pascale, E., Ade, P. A. R., Bock, J. J., et al. 2009, *ApJ*, 707, 1740
- Penner, K., Dickinson, M., Pope, A., et al. 2012, *ApJ*, 759, 28
- Penner, K., Pope, A., Chapin, E. L., et al. 2011, *MNRAS*, 410, 2749
- Perera, T. A., Chapin, E. L., Austermann, J. E., et al. 2008, *MNRAS*, 391, 1227
- Pforr, J., Maraston, C., & Tonini, C. 2012, *MNRAS*, 422, 3285
- Pilbratt, G. L., Riedinger, J. R., Passvogel, T., et al. 2010, *A&A*, 518, L1
- Poglitsch, A., Waelkens, C., Geis, N., et al. 2010, *A&A*, 518, L2
- Pope, A., Bussmann, R. S., Dey, A., et al. 2008, *ApJ*, 689, 127

- Pope, A., Scott, D., Dickinson, M., et al. 2006, MNRAS, 370, 1185
- Pope, A., Borys, C., Scott, D., et al. 2005, MNRAS, 358, 149
- Prescott, M. K. M., Kennicutt, R. C., Jr., Bendo, G. J., et al. 2007, ApJ, 668, 182
- Price, S. H., Kriek, M., Brammer, G. B., et al. 2013, arXiv:1310.4177
- Puget, J.-L., Abergel, A., Bernard, J.-P., et al. 1996, A&A, 308, L5
- Reddy, N., Dickinson, M., Elbaz, D., et al. 2012, ApJ, 744, 154
- Reddy, N. A., Erb, D. K., Pettini, M., Steidel, C. C., & Shapley, A. E. 2010, ApJ, 712, 1070
- Riguccini, L., Le Floch, E., Ilbert, O., et al. 2011, A&A, 534, A81
- Rowlands, K., Gomez, H. L., Dunne, L., et al. 2014, arXiv:1403.2995
- Rowlands, K., Dunne, L., Maddox, S., et al. 2012, MNRAS, 419, 2545
- Rujopakarn, W., Rieke, G. H., Eisenstein, D. J., & Juneau, S. 2011, ApJ, 726, 93
- Salpeter, E. E., 1955, ApJ, 121, 161
- Schawinski, K., Simmons, B. D., Urry, C. M., Treister, E., & Glikman, E. 2012, MNRAS, L488
- Serjeant, S., Dye, S., Mortier, A., et al. 2008, MNRAS, 386, 1907
- Todini, P., & Ferrara, A. 2001, MNRAS, 325, 726
- Tran, Q. D., Lutz, D., Genzel, R., et al. 2001, ApJ, 552, 527
- Treister, E., Cardamone, C. N., Schawinski, K., et al. 2009, ApJ, 706, 535

- Tyler, K. D., Le Floch, E., Rieke, G. H., et al. 2009, *ApJ*, 691, 1846
- Viero, M. P., Moncelsi, L., Quadri, R. F., et al. 2013, *ApJ*, 779, 32
- Wang, W.-H., Cowie, L. L., Barger, A. J., Keenan, R. C., & Ting, H.-C. 2010, *ApJS*, 187, 251
- Wang, W.-H., Cowie, L. L., & Barger, A. J. 2006, *ApJ*, 647, 74
- Weingartner, J. C., & Draine, B. T. 2001, *ApJ*, 548, 296
- Zaritsky, D. 1994, *AJ*, 108, 1619